POLYMER BRUSHES INFILTRATED BY NANOPARTICLES AND APPLICATIONS TO THE NUCLEAR PORE COMPLEX

by

Michael G. Opferman

BS, University of Pittsburgh, 2006

MS, University of Pittsburgh, 2007

Submitted to the Graduate Faculty of

the Kenneth P. Dietrich School of Arts and Sciences in partial fulfillment

of the requirements for the degree of

Doctor of Philosophy

University of Pittsburgh

2013

UNIVERSITY OF PITTSBURGH

KENNETH P. DIETRICH SCHOOL OF ARTS AND SCIENCES

This dissertation was presented

by

Michael G. Opferman

It was defended on

November 22, 2013

and approved by

Rob D. Coalson, Department of Chemistry

David Jasnow, Department of Physics & Astronomy

Tony Duncan, Department of Physics & Astronomy

Hanna Salman, Department of Physics & Astronomy

Shigeru Amemiya, Department of Chemistry

Anton Zilman, University of Toronto

Dissertation Director: Rob D. Coalson, Department of Chemistry

POLYMER BRUSHES INFILTRATED BY NANOPARTICLES AND APPLICATIONS TO THE NUCLEAR PORE COMPLEX

Michael G. Opferman, PhD

University of Pittsburgh, 2013

Systems of grafted polymers in the presence of additives are useful in a variety of contexts including industrial applications, solar cells, organic electronics, drug delivery, and nucleocytoplasmic transport. In this thesis, we will consider the morphologies that polymer brushes attain when exposed to a solution of additives (which we generically term "nanoparticles"), particularly when those nanparticles interact attractively with the polymers. We find that nanoparticles of this type can have a dramatic effect on the height of the polymer chains above the grafting surface, and they can induce highly non-uniform morphologies, including ones in which a dense layer of nanoparticles and monomers forms near the grafting surface. We consider especially the relevance of the system to several experiments performed on biopolymers in the nuclear pore complex when they interact attractively with transport factors that regulate nucleocytoplasmic transport. We find that, although these experiments appear to give inconsistent results, the inconsistencies can be reconciled through two simple models: the Alexander-de Gennes polymer brush, and the Milner-Witten-Cates polymer brush. Our findings should contribute to the understanding of the nuclear pore complex in that experiments can be better understood in the context of their relevant control parameters.

TABLE OF CONTENTS

LIST OF TABLES

LIST OF FIGURES

1.0   INTRODUCTION

1.1   THE NUCLEAR PORE COMPLEX

1.1.1   What is the Nulcear Pore Complex?

In eukaryotic cells, the DNA is located in the nucleus, while the operational machinery of the cell is found in the cytoplasm. The two are separated by a double lipid bilayer membrane (approximately $35 - 40nm$ thick in the case of yeast [1]). This compartmentalization of the cell must be accompanied by pores in the membrane which enable the translocation of cargoes between the nucleus and the cytoplasm. The sole passageway through the nuclear membrane is the nuclear pore complex (NPC). A typical mammalian cell contains thousands of NPCs on a single nucleus [2], transporting $\sim$1 million total macromolecules per second [3].

The core scaffold of the NPC consists of an hourglass-shaped, eight-fold symmetric rigid framework embedded in the nuclear membrane that is about $40nm$ across at its narrowest point [4]. The central core is anchored into the membrane by rings of proteins called nucleoporins ("nups") at each end. On the cytoplasmic side, the nup ring is attached to eight flexible cytoplasmic fibrils that extend into the cytoplasm, while on the nuclear side, eight filaments extend into the nucleus to form a rigid "nuclear basket" structure [2, 5]. Several pictures of the core structural components of the NPC can be seen in Fig. 1.

In addition to the rigid, structural portion of the NPC, there are other flexible, possibly dynamic nups typically 200-700 amino acids in length that contain characteristic phenylalanine glycine (FG) repeat domains, referred to as "FG nups" [6]. Approximately 150 FG nups are grafted to the walls of the NPC transport channel [7]. The FG repeat domains are typically made up of sequences of FG, FXFG or GLFG repeat motifs separated by spacer sequences [6, 8, 9]. In total, approximately one-third of nups contain

these FG sequences, and the total number of FG repeat domains in one NPC is in the thousands [5] (perhaps ∼20-30 per FG nup [8]). The FG repeat domains make up 12% of the NPC mass [7] . FG nups are in the class of natively unfolded proteins, meaning that they are flexible and lack any significant secondary structure [6, 10]. The FG nups occupy much of the available space in the transport channel, though their exact location and morphology *in vivo* is disputed [11].
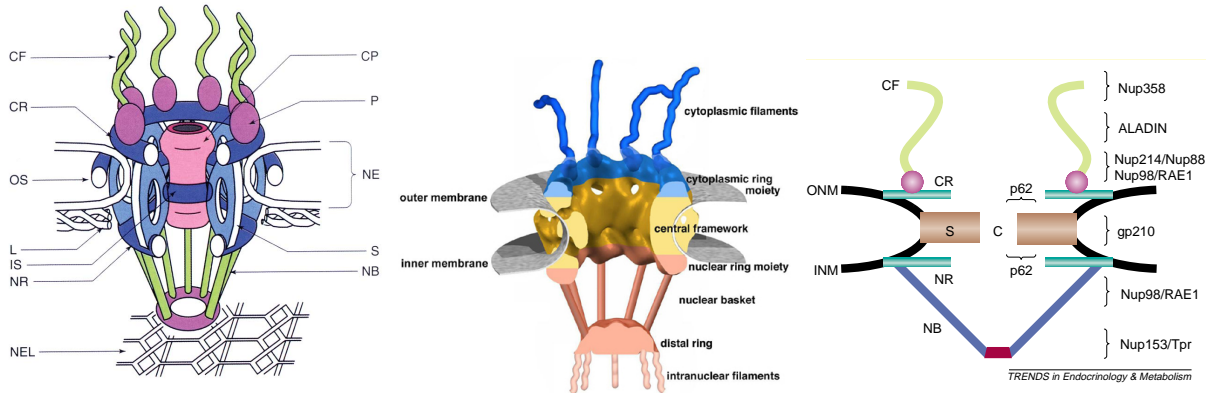
Figure 1: Three pictures of the NPC. In each case, the cytoplasmic side is shown at the top. *Left Panel:* Schematic cartoon of the NPC from [8]. Note that this early picture of the NPC erroneously shows a structural component to the NPC in the center of the transport channel. This structure was later concluded to be a result of the non-structural components of the NPC and their interactions with the cargo. *Center Panel:* Image of the NPC obtained from tomography of frozen NPCs from [12]. *Right Panel:* Schematic cartoon of the NPC from [13]

.

From a functional standpoint, the NPC must selectively transport a wide range of cargoes such as snRNPs, histones, transcription factors, mRNA, tRNA, and ribosomal subunits [5]. That is, unlike many other structures in the cell (such as ion channels), nucleocytoplasmic transport does not occur through a wide range of individually specialized channels designed for each particular cargo, but rather a single essential structure, the NPC. The NPC must have properties robust enough to accomplish this task and yet be selective enough to prevent the passage of unwanted cargoes. This is achieved through the use of transport receptors, which signal to the NPC which cargoes are to be permitted passage through the channel.

From a medical standpoint, the NPC is associated with a number of diseases including primary biliary

cirrhosis, in which an autoimmune response targets components of the NPC and results in cirrhosis of the liver, and triple A syndrome, in which mutations of a gene encoding the protein ALADIN, which is localized to the NPC, result in a variety of problems including an inability of the adrenal cortex to secrete glucocorticoids. NPC proteins are also implicated in cancer in a variety of ways. For instance the gene encoding Nup98 is associated with a number of oncogenic fusion proteins [13]. In addition, the NPC plays a role in viral infection. Some viruses dock onto nups at the cytoplasmic side of the NPC in order to inject their genomes into the nucleus, and others interact with specific nups in such a way as to inhibit or interfere with nucleocytoplasmic transport as a way to enhance their own replication. As a result, anti-viral drugs could be designed that target the interactions between viruses and nups in order to inhibit this step in viral replication [13]. Conversely, it may be desirable to deliver drugs into the nucleus, in which case the drug delivery system requires a method of traversing the NPC. This likewise requires a better understanding of the mechanism by which the NPC operates so that it can be co-opted or overcome [14].

1.1.2 Transport through the NPC

Molecules smaller than about $40kDa$ [5] ($\sim 5nm$ in diameter [15]) are able to passively diffuse through the free space in the NPC channel without assistance. This would include the transport of water and small ions, for example. For larger cargoes, up to about $39nm$ in diameter [16] (but more typically $\sim 25nm$ [2]), a transport receptor is required for transport of the cargo.

Although the exact details vary given the wide range of transport receptors and cargoes which pass through the NPC (see, e.g., the review in [2]), a cargo molecule to be imported into the nucleus contains a nuclear localization sequence (NLS), and this sequence enables the cargo to form a complex with the transport receptor. The formation of such complexes on the cytoplasmic side of the NPC creates a concentration gradient of receptor-cargo complexes, thereby enabling transport of the complexes into the nucleus without the consumption of energy during transport. In the nucleus, a molecule called RanGTP dissociates the complex, thereby maintaining the concentration gradient and releasing the cargo for use. The export of cargoes occurs via a conceptually similar mechanism, though the NLS is replaced by a nuclear export signal (NES), and typically the outgoing cargo must form a trimeric complex with the receptor and a RanGTP molecule. [2, 5, 17].
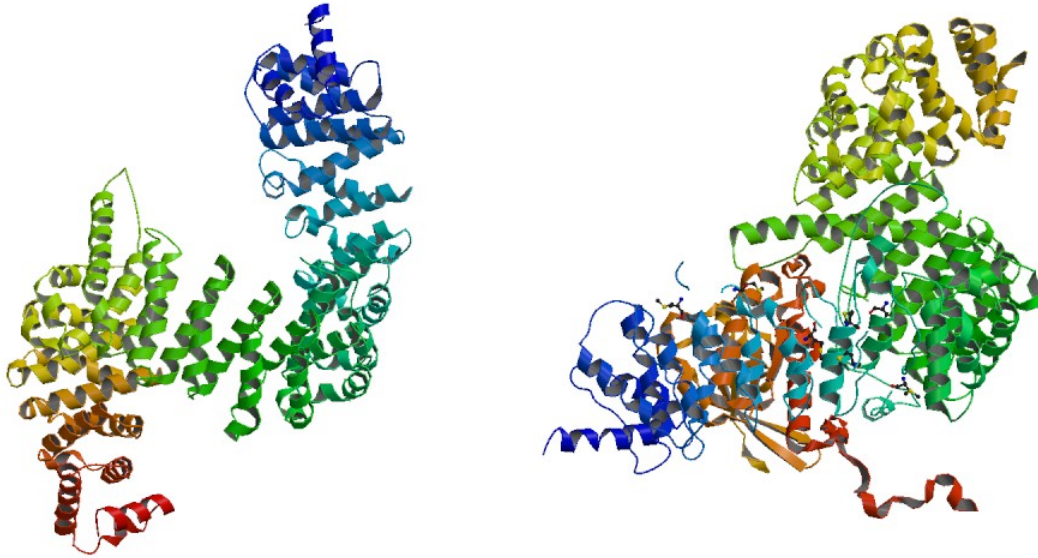
Figure 2: Diagram showing the structure of human transportin 1 (Kapβ2). *Left:* From [18], the structure of free transportin 1. *Right:* From [20], the structure of the complex Kapβ2-Ran x GppNHp. One can see that the cargo fits into the pocket of the structure of the free molecule.

Many of the transport receptors come from the family of karyopherins ("kaps") [2]. For instance, one of the most commonly discussed transport receptors is Kapβ2, also known as Transportin1. Kapβ2 has a mass of about $100kDa$ and a size of about $5 - 10nm$ [18]. Its structure can be seen in Fig. 2. As with other import receptors (importins), the binding of cargo and RanGTP onto the kap is mutually exclusive. As a result, the receptor will tend to bind cargo where the concentration of RanGTP is low (the cytoplasm), and will bind RanGTP where the concentration of RanGTP is high (the nucleus). In addition, the cytoplasm contains RanGAP, which is capable of switching RanGTP into RanGDP. Since RanGDP does not bind strongly to Kapβ2, this process releases the Ran and frees the transport receptor to accept a new cargo molecule. [2, 19] This results in a loading of cargo in the cytoplasm and an unloading in the nucleus as seen in Fig. 3. Conversely, RanGTP is loaded in the nucleus and unloaded in the cytoplasm, and the direction of RanGTP transport is opposite to the direction of cargo transport. In the case of export, the action of RanGAP in the cytoplasm destabilizes the trimeric complex by turning RanGTP into RanGDP, and this stimulates the release of both cargo and RanGTP in the cytoplasm. Another transport

4

factor called NTF2 is responsible for binding to the RanGDP and returning it to the nucleus through the NPC. Here the RanGDP is switched back to the RanGTP state (through the action of RanGEF), and it becomes available to continue the transport cycle.
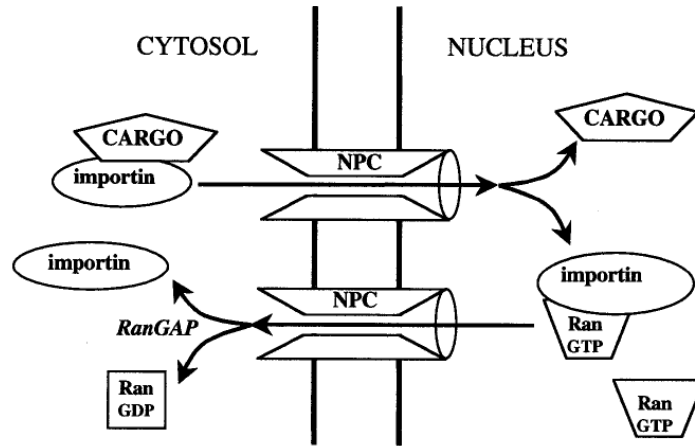
Figure 3: Diagram showing the transport cycle for nuclear import. (1) Receptor-cargo complexes are transported into the nucleus, (2) the cargo is released by the binding of RanGTP to the receptor, (3) the receptor-RanGTP complex is transported to the cytoplasm, (4) The RanGTP is transformed into RanGDP through the action of RanGAP, causing it to be released by the receptor, and (5) the receptor binds to another cargo. This figure is from [2].

It should be emphasized that, although the transport receptors do interact with the nups in the channel, the transport of the receptor-cargo complex is still diffusive in nature. That is, the transport itself does not (directly) consume energy. The NPC should not be viewed as a pump which moves complexes into areas of higher concentration, but rather each individual step which involves transport through the NPC is moving a given complex down its concentration gradient. The energy-consuming step occurs outside of the channel, where the concentration gradients are maintained via the switching between RanGTP and RanGDP. In fact, the kinetics can be modeled phenomenologically via a first-order Michaelis-Menten process in which the formation or dissociation of receptor-cargo complex in the nucleus and cytoplasm are the energy-consuming steps and diffusion across the NPC is purely based on the concentration gradients of the complexes. [21]

1.1.3 Transport Models

It is known that transport receptors bind to the FG repeat domains of FG nups [19]. For instance, it has been shown that the phenylalanine residue of the FXFG domain binds to the hydrophobic pocket on the receptor NTF2 [17, 22]. Although binding of receptor-cargo complexes to the FG nups in the channel is crucial to transport, there is not one unique transport model which appears to fit the available experimental data. In fact, many transport models have been proposed. For instance, in the "Reduction-of-Dimensionality" model (top-right panel of Fig. 4) the FG repeat domains are hypothesized to form a two-dimensional surface on which transport receptors undergo a two-dimensional random walk, while the spacer sequences block the remaining regions of the channel [17]. In the "Oily Spaghetti" model, a "spaghetti" of FG nups are imagined to occupy the periphery of the channel, leaving a central tube for passive transport. Transport receptors could easily move through the spaghetti by rapidly binding and unbinding to FG repeat domains, while other large cargoes could not [2]. In the "Forest" model (bottom-right panel of Fig. 4), nups are proposed to have collapsed globular domains near the channel walls and additional globular domains near the channel center, leaving two transport pathways in the remaining space [23, 24]. In the "Flycasting" model, it is proposed that a kap binds to a single nup filament for a long period of time until, still bound to the same nup, it reaches the nuclear side of the channel where the connection is cut through the action of RanGTP [25].

Although there are many different models of transport, one of the most fundamental disagreements in the community concerns whether the nups are in a flexible, random, polymer brush-like state in the channel or whether they form a more rigid mesh-like structure. This point can be emphasized by examining two transport models in particular.

In the "Selective Phase" model (bottom-left panel of Fig. 4), it is hypothesized that attraction between FG repeat domains causes a crosslinking of the nups into a hydrogel. From this viewpoint, it is the mesh size of the gel which determines the threshold for non-receptor-mediated transport. When molecules are larger than the mesh size of the gel, they are too large to fit through the "sieve," and the bonds between FG repeat domains that make up the crosslinks in the gel must be broken by the transport receptor in order to enable passage. As the receptor, perhaps loaded with cargo, melts into the gel, the FG repeat domains must re-bind behind it so that the transport remains selective. This theory is supported by the observations that FG nups can form hydrogels *in vitro*, that these hydrogels appear to selectively transport

6

B   Virtual gate/polymer brush   Reduction of dimensionality

Selective phase/hydrogel   Forest
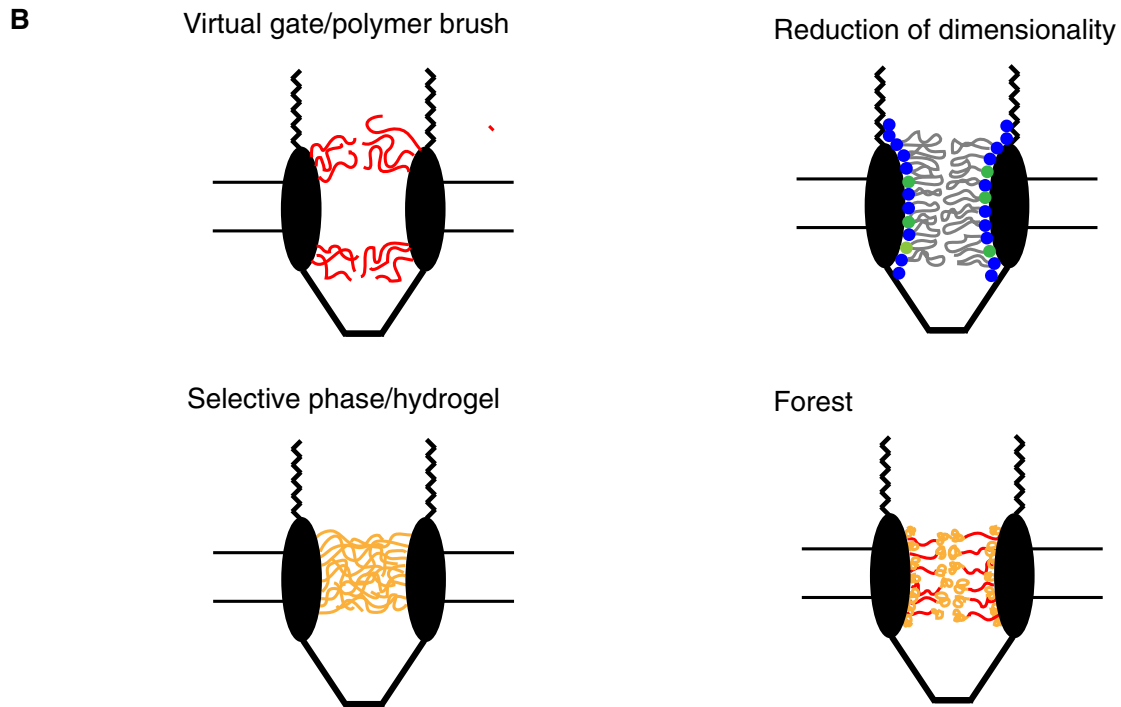
Figure 4: An illustrative diagram from [26] that shows where the FG nup "gate" in the NPC would be and what basic morphology it would have according to the indicated transport models. *Top Left:* The virtual gate, polymer brush, or reversible collapse model proposes the presence of an entropic barrier due to a polymer brush of nups near the periphery of the channel. *Top Right:* The reduction of dimensionality model proposes the formation of a two-dimensional FG surface (represented by the colored circles near the walls) on which receptors can move due to their binding interactions with the FG repeats. The spacer sequences of the nups block the remainder of the channel, preventing the passage of other large molecules. *Bottom Left:* The selective phase model proposes that the channel is filled with a crosslinked gel of FG nups. *Bottom Right:* The forest model proposes globular domains (represented by the orange balls) occupying both the periphery and an area near the channel center, leaving two remaining zones which could support transport.

kaps in a way similar to NPCs, and that cohesion between FG nups is crucial for transport [27–29]

In the "Reversible Collapse" model (top-left panel of Fig. 4), the FG nups are hypothesized to be in a flexible, dynamic, natively unfolded state in the channel (i.e., they form a polymer brush). They fill up most of the available space in the channel with an entropic barrier that prevents the passage of large molecules. In other words,the transport of cargo requires a compression of the nups so that they occupy a smaller volume in the channel. The entropy penalty associated with this compression makes an unfavorable state in terms of its free energy. In this model, the binding interactions between the transport receptor and the FG nups provide the free energy to offset and overcome the entropic barrier. The nups then collapse toward the wall of the channel in order to maximize the number of binding contacts with the transport receptor. This could open up the space necessary for transporting an additional transport receptor, for instance one that is weakly bound to the remaining FG nups. This theory is supported by the observations that grafted layers of FG nups can form a polymer brush *in vitro* and that the height of this brush is reduced upon the addition of transport receptors. [10, 30, 31]

It is also possible that the reality may be some hybrid of hypothesized mechanisms. For instance, nups may be in a brush-like state at the periphery of the channel, forming a "virtual gate" [32], but in a gel-like state near the channel's midpoint. This is referred to as the two-gate model [33].

1.1.4 Experiments on Grafted Nucleoporins

Particularly relevant to our work are the *in vitro* experiments in which FG nups were grafted to a flat surface and exposed to a solution of transport receptors. In particular, three such experiments will be discussed below, including some of the particular details that differ among the experiments. This information is summarized in Table 1.

In the first such experiment, described in Ref. [30] and summarized in Table 1, Lim *et al.* grafted multiple copies of the FG nup cNup153, which is composed of 604 amino acids for a contour length of around 200nm and comes from the nuclear periphery of the human NPC, to a gold nanodot at a grafting distance of about 23.9nm [36]. Various concentrations of the transport receptor Kapβ1 were introduced into the solution, and the height of the grafted polymers were measured by atomic force microscopy. In this experiment, it was found that as the concentration of transport receptors was increased, a reduction in the height of the nups was observed (to about 39% of their unperturbed height).

Experiment	Nup Used	Grafting Distance (a)	Height in the Absence of Kaps (h_0)	Height at Maximum Compression (h_{min})	Relative Compression (h_{min}/h_0)
Lim, *et al.* (2007) [34]	cNup153	24nm	29.1nm	11.3nm	0.388
Eisele, *et al.* (2010) [35]	Nsp1p	4.4nm	34nm	$\sim$34nm	$\sim$1
Schoch, *et al.* (2012) [31]	cNup62	2.4nm	14.1nm	12.7nm	0.901

Table 1: A summary of relevant experimental data. In Eisele, *et al.*, no compression of the layer is observed to within the experimental precision. In Schoch, *et al.*, we focus on the data set that is featured in the paper.

The existence of a brush collapse was corroborated by a similar experiment performed by Schoch *et al.*, a group that included Lim, as described in Ref. [31] and summarized in Table 1. In this experiment Kapβ1 was again introduced to a system of grafted nups. In this case, 240 amino acids of the FG nup cNup62, which comes from the central pore region of the human NPC, were grafting to a surface at a range of grafting distances from 2nm to 11nm, and the brush height was measured via the surface plasmon resonance (SPR) technique. It was found once again that a decrease in the height of the nup layer upon the addition of transport receptors occurred, but only for grafting distances less than 4.1nm and only to a maximum depth of about 90% of the unperturbed height. In addition, it was also found that a second regime exists at even higher receptor concentrations in which the nup layer swells back to, and eventually beyond, the unperturbed height. This regime was hypothesized to be associated with a pile-up of multiple layers of transport receptors in the grafted nups, thereby driving up the height.

Another similar experiment, descibed in Ref. [35] and summarized in Table 1, was performed by Eisele *et al.*, a group that included Görlich. In this case, 600 amino acids of the FG nup Nsp1p, which comes from the central pore region of the yeast NPC, were grafted to a lipid bilayer at a grafting distance of 4.4nm and exposed to the transport receptor Kap95p. It was found that the height of the nups did not decrease measurably upon the addition of transport receptors as measured by both AFM and quartz crystal microbalance with dissipation monitoring.

These experiments are often interpreted to support two very different *in vivo* transport mechanisms. The first two appear to support a collapse-based mechanism such as Reversible Collapse model, while the third appears to support the idea that a morphological reorganization does not occur in the pore, as in

the Selective Phase model. In Chapter 4, I will address the differences in light of the theoretical models developed in Chapters 2 and 3. One of the goals of this work is to provide a unified theoretical analysis of these *in vitro* experiments on grafted nucleoporins which explores the possibility that the apparent qualitative differences can be explained in light of the relevant parameter differences.

1.2   RELEVANT POLYMER SYSTEMS

1.2.1   The Alexander-de Gennes Polymer Brush

The experiments on grafted nucleoporins are reminiscent of another system from the field of polymer physics−namely, the system of grafted polymers. When a single polymer is grafted to a surface, it undergoes (approximately) a random walk in the vicinity of the grafting point and forms a roughly hemispherical "mushroom" on the grafting surface. The size of such a mushroom R, in terms of the polymerization of the chain N and the distance between monomers b will be roughly that of a self-avoiding random walk: $R \sim N^{3/5}b$ [37]. Since we will primarily focus on the scaling behavior, one can think of the size of the chain R as its end-to-end distance, but other choices such as the radius of gyration will differ only in numerical prefactors of order one and are equally good.

If many polymers are attached to the same surface, and the spacing between grafting sites is small enough, they will overlap and thereby interpenetrate and interact. Formally, one could consider a system of self-avoiding and other-avoiding random walkers, one starting at each of the grafting sites. In practice, we seek a simpler model of the system. In the regime where the polymers overlap suffiiciently strongly, each polymer's lateral extent will be, for the most part, limited by its neighbors, and the polymers will be forced to meander upward, away from the grafting surface. A system of grafted polymers in this overlapping limit is referred to as a "polymer brush." In this case, we make use of the simplifying assumption that the lateral size of the polymer will be limited to a size $\xi \sim a$, where a is the distance between grafting sites and ξ is referred to as the blob size of the brush [37]. In the direction perpendicular to the grafting surface, there is no such constraint, and the height of the polymers above the grafting surface will exceed the blob size. One can imagine the brush as being made of stacks of blobs filling the space up to the brush height. Since the brush is made of stacked blobs and each blob can be expected to have roughly the same

density, one might suppose that the density of monomers inside the brush will be approximately constant up to the edge of the brush. This idea is referred to as the Alexander-de Gennes approximation, which assumes that the density of monomers throughout the polymer layer is constant [37, 38]. Although this approximation is not very accurate, the results it produces are surprisingly good for several key brush properties.

In order to examine the Alexander-de Gennes polymer brush more quantitatively, we will model its free energy using a viewpoint analogous to Flory's approach to modeling the free energy of polymer melts [39], as discussed in Appendix A. Although this approach has been remarkably successful, it should be noted that it includes many crude approximations. We will treat aspects of the polymer systems which, in principle, could be crucial, such as the excluded volume between monomers and the connectivity of the chain, only approximately. Although the approach may be inexact, we will find that several experimentally and computationally verified conclusions result.

We will regard the characteristics of a polymer brush as resulting from a competition between the stretching entropy of the polymer chains, which favors more compact, less stretched configurations, and the excluded volume repulsion between monomers, which favors less compact, more stretched configurations. Some basic properties of the polymer brush may be obtained by taking the free energy of each chain of the brush to be, at the mean field level and assuming a homogeneous monomer concentration throughout,

$$F = a^2 h (1 - \psi) \ln(1 - \psi) + \frac{h^2}{2N} \tag{1.1}$$

$$\simeq a^2 h \left(-\psi + \frac{1}{2}\psi^2 + \frac{1}{6}\psi^3 \right) + \frac{h^2}{2N} \tag{1.2}$$

where a is the distance between grafting points, h is the height of the brush above the grafting surface, N is the polymerization of the chain, $\psi = Nb^3/a^2h$ is the volume fraction of space occupied by monomers, and the expansion has been carried out for small ψ. Please note that here and throughout this treatment, energies will be expressed in units of kT (where k is the Boltzmann constant and T is the temperature) and lengths will be expressed in units of b, the monomer diameter. The first term in Eq. (1.1), which represents the entropy of the solvent, can be obtained in several ways including the use of a lattice gas counting argument (see Appendix A). The last term represents the entropy of a Gaussian polymer chain. It can be obtained by calculating the probability distribution of end-to-end vectors for a Gaussian random walk $P(R)$ and converting to a free energy via $F \sim -\ln(P(R))$ [40]. Note that absent from this free

energy are any "enthalpic" interactions such as attractions or long-range repulsions between monomers or any interactions with solvent. If one expands the logarithm for small ψ, the free energy can be written in the form shown in Eq. (1.2).

Minimizing the approximate free energy Eq. (1.2) with respect to h at constant a and N and keeping only the lowest order term, one obtains

$$h_{eq} = \frac{1}{2^{1/3}} N a^{-2/3} \tag{1.3}$$

which is regarded as the basic scaling relationship for the polymer brush [37, 41]. An interesting property of this result is that $h \sim N$. This is in stark contrast to ordinary random walk statistics in which the size of the walk scales with some power of N less than one. Physically, the lateral extent of the chain is limited by its neighbors and adding additional monomers to the chain would simply stack more "blobs" on top of the brush.

Eq. (1.1) may be viewed as an approximate starting point for the consideration of polymer brushes. The characteristics of the brush may be modified by the inclusion of other interactions, such as additional attraction or repulsion between monomers, or interactions between the monomers and the solvent. Several relevant modifications to this basic Alexander-de Gennes brush will be treated below.

1.2.2 An Ungrafted Polymer Interacting with Solvent

One way of modifying the properties of a polymeric system is through the use of solvents. Solvents are generally classified as "good" or "bad." A good solvent is one which swells the size of the polymer, while a bad solvent reduces the size of the polymer. Thus, one way to model the effects of a good solvent is with an effective repulsive interaction between monomers, and a bad solvent with an attractive interaction[42]. If a solvent causes neither additional attraction nor additional repulsion between monomers, it is referred to as "athermal" [43]. One special case worth noting is the "theta solvent," in which the effective attractive interactions produced by the solvent are equal in magnitude to the repulsive ineractions which are present due to effects inherent, such as excluded volume between monomers. In a theta solvent, the effective attraction (approximately) cancels the preexisting repulsion, and this cancellation causes the polymer to behave similarly to an ideal Gaussian chain in which monomers do not interact at all [44].

Before considering the effect of solvents on the polymer brush, we will first consider their effect on an ungrafted polymer chain. A simple Flory-Huggins mean field analysis of a polymer chain in a single solvent yields, in units of kT (see Appendix A),

$$F = R^3 \left((1 - \psi) \ln(1 - \psi) + \chi \psi (1 - \psi) \right) + \left(\frac{R}{R_0} \right)^2 \tag{1.4}$$

where $\psi = Nb^3/R^3$ is the volume fraction of monomers, R is the size of the polymer chain, R_0 is the size of an ideal chain (i.e., without excluded volume interactions), and χ expresses the interaction between the polymer and the solvent (e.g., the polymer may be hydrophobic or hydrophilic). χ is known as the Flory or Flory-Huggins parameter. Recall that the length R gives the qualitative length scale of the polymer chain, but is imprecise to within a numerical factor of order one. As such, the numerical coefficients in the equations that follow are not meant to be precise, but only to give the general scaling behavior.

A simple analysis of this free energy may be performed by expanding to third order in ψ. This gives

$$F = (\chi - 1)N + \frac{1}{2}(1 - 2\chi)\frac{N^2}{R^3} + \frac{1}{6}\frac{N^3}{R^6} + \left(\frac{R}{R_0} \right)^2. \tag{1.5}$$

Minimizing this function over the polymer size R yields,

$$\frac{\partial F}{\partial R} = -\frac{3}{2}(1 - 2\chi)\frac{N^2}{R^4} - \frac{N^3}{R^7} + 2\frac{R}{R_0^2} = 0. \tag{1.6}$$

Now we will consider three limiting cases.

First, let $\chi = 1/2$ such that the first term in Eq. (1.6) goes to zero. This corresponds to a "theta" solvent, at the mean field level, since the solvent interactions cancel the monomer-monomer interactions in the leading order term. In this case, $R = R_0$ since the chain is approximately ideal, and we obtain

$$R_0 = \left(\frac{1}{2} \right)^{1/6} N^{1/2} \tag{1.7}$$

in units of the monomer size b. Note that $R_0 \sim N^{1/2}$. Since the binary interactions between monomers have been canceled out by the solvent interactions, the polymer in theta solvent behaves in a way similar to an ideal chain, in which monomers do not interact at all besides their connectivity, and one obtains ordinary random walk scaling behavior.

Next, let $\chi \ll 1/2$. This is the good solvent limit, in which the solvent interaction term will tend to swell the polymer. In this case, the second term in Eq. (1.6) can be neglected because the additional

swelling of the chain it causes will be negligible compared to the swelling caused by the solvent. Physically, the two-body (ψ^2) monomer-monomer repulsion will be the primary force that swells the chain, and this will be balanced by the stretching entropy at equilibrium. This leaves

$$R_{good} = \left(\frac{3}{4}(1 - 2\chi)N^2 R_0^2 \right)^{1/5}. \tag{1.8}$$

Making use of Eq. (1.7), this means that $R_{good} \sim N^{3/5}$. This mean-field scaling behavior corresponds to a self-avoiding random walk (SAW) [44]. In this regime, the scaling is dominated by the requirement that the monomers cannot overlap, and the polymer trajectories must avoid each other.

Finally, if $\chi \gg 1/2$, we reach the bad solvent limit. In this case, the last term in Eq. (1.6) can be neglected. Physically, the effective monomer-monomer attractions become dominant over the stretching entropy as the primary force causing contraction of the chain. This effect is balanced by the three-body (ψ^3) repulsion term. Discarding the stretching entropy term, we obtain

$$R_{bad} = \left(\frac{2N}{3(2\chi - 1)} \right)^{1/3}. \tag{1.9}$$

Here, $R_{bad} \sim N^{1/3}$ meaning that the *volume* of the polymer chain scales linearly with N. A polymer chain with this property is referred to as a globule. The coil-globule transition in polymer chains is related to the thermal denaturation of globular proteins in biology, in which the transition to the coil state corresponds to a loss of biological activity [42].

Considering the minimization of Eq. (1.4) numerically, we can plot R as a function of χ over the full range of χ. This produces the result shown in Fig. 5. The chain transitions between the swollen coil and compressed globule states as one sweeps through χ.

1.2.3 Polymer Brush Interacting with Solvent

A solvent can be added to the polymer brush free energy of Eq. (1.1) just as it was in Eq. (1.4). Namely, the term $\chi\psi(1 - \psi)$ must be added to take into account the interaction of the monomers with the solvent. This gives a free energy per chain of the form

$$F = a^2 h \left((1 - \psi) \ln(1 - \psi) + \chi\psi(1 - \psi) \right) + \frac{h^2}{2N}. \tag{1.10}$$
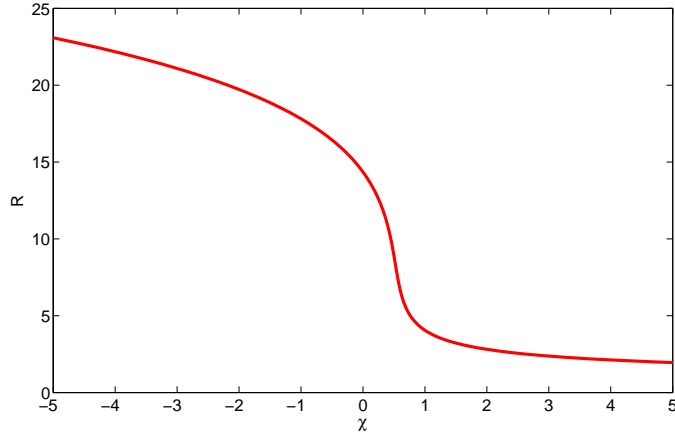
Figure 5: The relationship between the polymer size R and the Flory parameter representing the solvent quality χ for a polymer in a solvent. The decrease in R corresponds to the transition between the coil and globule states. This plot shows the case of polymerization $N = 100$.

Performing the same analysis, we minimize with respect to h and expand the logarithm to obtain

$$\frac{\partial F}{\partial h} = a^2 \ln(1 - \psi) + \frac{N}{h} + \frac{\chi N^2}{a^2 h^2} + \frac{h}{N} \tag{1.11}$$

$$\simeq -(1 - 2\chi)\frac{N^2}{2a^2 h^2} - \frac{N^3}{3a^4 h^3} + \frac{h}{N}. \tag{1.12}$$

In the case of good solvent ($\chi \ll 1/2$), the second term in the expansion Eq. (1.12) can be neglected for the same reason discussed in the previous section, and one obtains

$$h_{good} = \frac{(1 - 2\chi)N}{2^{1/3} a^{2/3}}. \tag{1.13}$$

Note that the ordinary brush scaling relationship seen in Eq. (1.3), $h \sim N a^{-2/3}$, is preserved.

In the case of bad solvent ($\chi \gg 1/2$), the first term can be neglected, and one obtains

$$h_{bad} = \frac{2N}{3(2\chi - 1)a^2}. \tag{1.14}$$

Note that in this case the volume per chain $a^2 h \sim N$. Since the volume of the brush scales with the number of monomers, this corresponds to the collapsed state, analogous to the globule state in Eq. (1.9), in which monomers are densely packed.

15
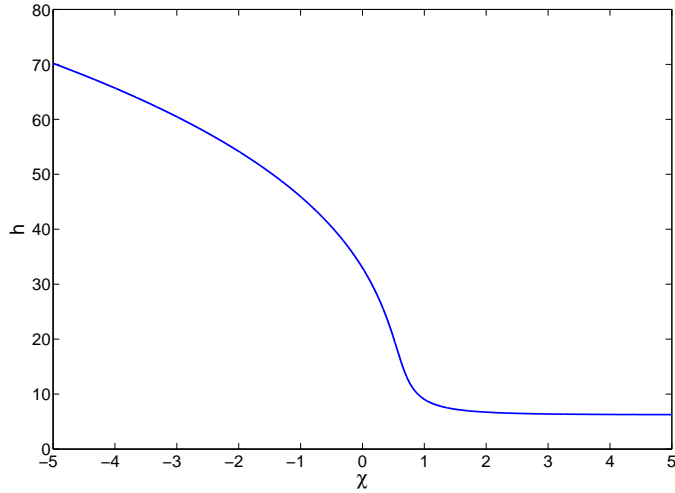
Figure 6: The relationship between the polymer brush height h and the Flory parameter representing the solvent quality χ for a polymer brush in a solvent. Decrease in h corresponds to the collapse of the polymer brush. This plot uses grafting distance $a = 4$ and polymerization $N = 100$.

The numerical solution over the full range of χ in shown in Fig. 6. As with the ungrafted polymer chain, the volume of the polymer brush changes with the character of the solvent, but the change is continuous and smooth with respect to χ.

1.2.4 Milner-Witten-Cates Polymer Brush

The arguments above assume a homogeneous distribution of monomers throughout the polymer layer (i.e. the Alexander-de Gennes approximation). One can avoid making this assumption by first regarding the monomer volume fraction ψ as a local quantity $\psi(\vec{r})$ which gives the monomer volume fraction in the neighborhood of point $\vec{r}$. In addition, the assumption that the stretching entropy of the polymer is simply $\sim h^2$, will be replaced by calculating the stretching energy as one would for a continuous string. In units of kT, the grand canonical free energy (or, equivalently, generalized Edwards Hamiltonian [45]) of the brush for a given set of monomer coordinates is given by a functional of the following form [41, 46, 47]:

$$F[\{\vec{r}_\alpha(s)\}] = \sum_\alpha \frac{1}{2b^2} \int_0^N ds \left(\frac{\partial}{\partial s} \vec{r}_\alpha(s) \right)^2 + \int d^3 r f(\psi(\vec{r})) \qquad (1.15)$$

16

where α indexes the polymer chain, $\vec{r}_\alpha$ locates monomer s ($0 \le s \le N$) on chain α, and f is the local non-elastic free energy density.

If this free energy functional is minimized over the polymer trajectories (i.e. the first variation is set to zero), one obtains

$$-\frac{1}{b^2}\frac{\partial^2}{\partial s^2}\vec{r}_\alpha(s) + \frac{\partial}{\partial \vec{r}_\alpha}\frac{\partial}{\partial \psi}f(\psi) = 0. \tag{1.16}$$

Additional details about this minimization for a more general case can be found in Appendix C. The insight of Milner, Witten, and Cates is that this differential equation is equivalent to Newton's second law if one makes the correspondence [46]

$$\begin{aligned}
\frac{1}{b^2} &\rightarrow m \\
s &\rightarrow t \\
-\frac{\partial}{\partial \psi}f &\rightarrow U
\end{aligned} \tag{1.17}$$

where m, t, and U are the mass, time, and potential energy respectively. Furthermore, if we assume that the brush is homogeneous in the lateral direction (such that ψ is a function of the distance from the grafting surface z only) we know that, although the chain ends may be at different distances from the grafting surface, every trajectory must reach the grafting surface in the same "time" N, even though the "initial velocity" $\partial z/\partial s(0) = 0$ by the condition that the tension in the polymer must be zero at the chain end. By analogy to Newton's equations, we therefore know that the appropriate "potential energy" corresponds to the harmonic oscillator. Namely,

$$\frac{\partial}{\partial \psi}f = A - Bz^2 \tag{1.18}$$

where z is the distance from the grafting surface. The constant B may be determined from Eq. 1.16. Since the period of the oscillator is $4N$ and the mass is $1/b^2$, and knowing that $B = m\omega^2/2$ for a harmonic oscillator, we can show that

$$B = \frac{\pi^2}{8N^2b^2}. \tag{1.19}$$

The constant A, which corresponds to an overall shift in the potential and does not affect the classical mechanics of the system, is determined from the normalization condition that the total number of monomers in the chain must be N and the grafting density is $1/a^2$. Namely,

$$\int_0^h \psi(z)dz = N/a^2. \tag{1.20}$$

In general, one could solve Eqs. (1.18) and (1.20), along with an appropriate definition of f, self-consistently using an iterative approach.

For a polymer brush with no solvent interactions, we can use

$$f = (1 - \psi(\vec{r})) \ln(1 - \psi(\vec{r})) \simeq -\psi(\vec{r}) + \psi^2(\vec{r})/2. \tag{1.21}$$

in analogy with Eq. (1.1). The expansion for small ψ is particularly useful here because in this case the solution may be obtained analytically. Eq. (1.18) becomes

$$\psi = (A + 1) - \frac{\pi^2}{8N^2b^2} z^2. \tag{1.22}$$

In other words, the monomer density profile is a downward-facing parabola with maximum value at the grafting surface. This solution is often referred to as the "parabolic brush." The height h of this brush is the point at which $\psi(h) = 0$. This gives

$$A + 1 = \frac{\pi^2 h^2}{8N^2b^2}. \tag{1.23}$$

Furthermore, combining Eqs. (1.20), (1.22), and (1.23) gives

$$h^3 = \frac{12N^3b^2}{\pi^2a^2}. \tag{1.24}$$

Note that although many of the details differ when comparing the Alexander-de Gennes result Eq. (1.3) to the MWC result Eq. (1.24), some of the essential features, such as the scaling relationship $h \sim Na^{-2/3}$, are preserved. This is why the Alexander-de Gennes model is still widely used even though its basic assumption (a density profile which is independent of z in the brush) is incorrect.

1.2.5 MWC Polymer Brush with Solvent Interactions

The same analysis can be performed for a polymer brush with solvent. Eqs. (1.15)-(1.20) still hold, but in this case we must use a more complicated $f(\psi)$. Expanding the expression in the same way that we did for the Alexander-de Gennes brush, we have

$$f = (1 - \psi) \ln(1 - \psi) + \chi\psi(1 - \psi) \simeq (\chi - 1)\psi + (\frac{1}{2} - \chi)\psi^2 + \frac{1}{6}\psi^3. \tag{1.25}$$

When $\chi \ll 0$, the ψ^3 term in the expansion may be neglected. As in the Alexander-de Gennes case, when the solvent quality is good, both the ψ^2 and ψ^3 terms result from the repulsion between monomers, and it is sufficient to keep the lowest order term of this type. The brush remains parabolic, but the use of Eq. (1.18) with the free energy density of Eq. (1.25) yields

$$(1 - 2\chi)\psi = (A + 1) - \frac{\pi^2}{8N^2b^2}z^2. \tag{1.26}$$

Eq. (1.23) still holds, and Eq. (1.24) becomes

$$h_{good}^3 = \frac{12(1 - 2\chi)N^3b^2}{\pi^2a^2}. \tag{1.27}$$

The polymer brush is swollen, but the scaling relation $h \sim Na^{-2/3}$ is preserved as is the qualitative shape of the brush$-$a downward-facing parabola.

The case of an MWC brush in a bad solvent is slightly more complicated. In this case, the ψ^3 term cannot be neglected, and Eqs. (1.18) and (1.25) yield

$$\frac{\psi^2}{2} + (1 - 2\chi)\psi = (A + 1) - \frac{\pi^2}{8N^2b^2}z^2. \tag{1.28}$$

Now the left hand side of the equation is potentially non-monotonic, and inverting the equation to obtain $\psi(z)$ becomes non-trivial. If the expression $\psi^2/2 + (1 - 2\chi)\psi$ has its minimum in the physically relevant domain $0 < z < h$, then the inversion of Eq. (1.28) would have two values of ψ corresponding to some values of z. To deal with this issue, an additional physical consideration must be invoked. Namely, we require that the osmotic pressure $\Pi(z)$ must be a continuous function in order to ensure mechanical equilibrium in the layer [48]. The osmotic pressure in the layer is

$$\Pi = \psi\frac{\partial f}{\partial \psi} - f = -(1 + \chi\psi)\psi - \ln(1 - \psi) \simeq \frac{1}{2}(1 - 2\chi)\psi^2 + \frac{1}{3}\psi^3. \tag{1.29}$$
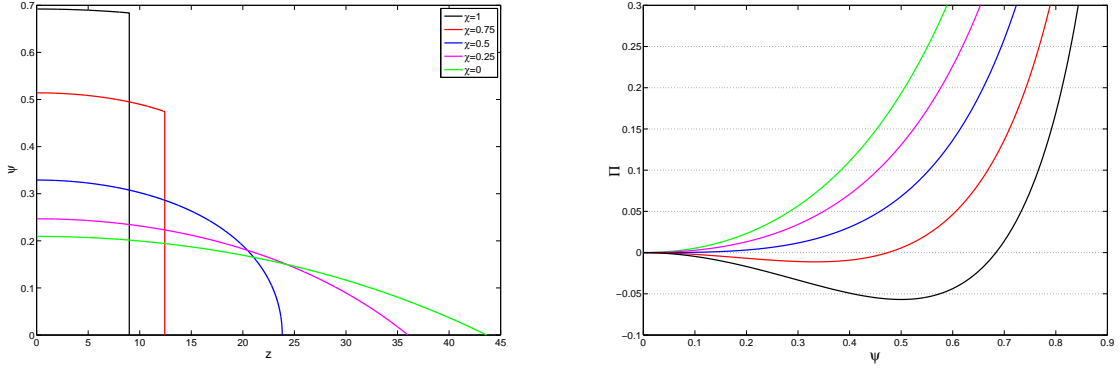
Figure 7: *Left:* Monomer density profiles obtained from the MWC model as the solvent quality χ is varied. At $\chi > 1/2$ the density profile has a discontinuity at the location where the osmotic pressure becomes zero. This plot uses grafting distance $a = 4$ and polymerization $N = 100$. *Right:* The osmotic pressure as a function of the monomer volume fraction for the same parameters. The osmotic pressure is non-monotonic for $\chi = 0.75$ and $\chi = 1$. The negative portion of the osmotic pressure is not physically meaningful, and as a result the monomer volume fraction must jump discontinuously from zero to the nonzero value of ψ at which $\Pi(\psi) = 0$.

Note that since $\psi(z \geq h) = 0$, this means $\Pi(z \geq h) = 0$. One can ensure continuity of the osmotic pressure and a valid solution to Eq. (1.28) by having a discontinuity in $\psi(z)$ at $z = h$ that connects $\psi = 0$ to the nonzero solution $\psi = \psi^*$ which satisfies Eq. (1.28). One must be cautious about using the series expansion form in this regime since (as one can see in Fig. 7) the solution is not guaranteed to have $\psi \ll 1$. Solving without making use of the series expansion yields

$$\psi^* = 1 - e^{-(1+\chi\psi^*)\psi^*} \tag{1.30}$$

which can be solved numerically. $\psi(z)$ will decrease monotonically as z increases until it reaches $\psi(z) = \psi^*$. At this z the ψ will drop discontinuously to zero and the brush will suddenly terminate. Physically, the monomer density does not gradually decrease to zero, leaving a region of sparse density near the top of the brush. Instead, the high-density brush ends quite suddenly. The result of this is illustrated in Fig. 7. Although the density profiles are in some cases discontinuous, the brush height h vs. the solvent quality χ is not. The behavior of the brush for the full range of solvent quality can be seen in Fig. 8.

20
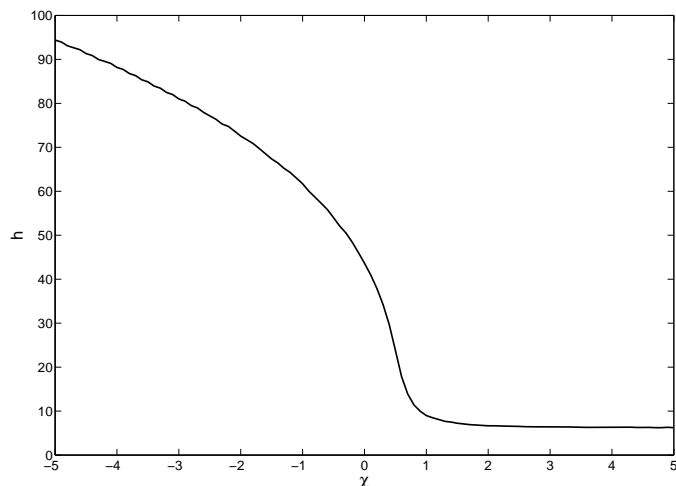
Figure 8: The relationship between the polymer brush height h and the Flory parameter representing the solvent quality χ for a polymer brush in a solvent as obtained from the MWC model. This plot uses grafting distance $a = 4$ and polymerization $N = 100$.

1.2.6 Polymers Interacting with Mixed Solvent

In addition to the cases considered so far, there are many generalizations and special cases which are possible to consider. One important case is a polymer or polymer brush in a mixture of two or more solvents [45, 49–57]. One could attempt to use either of the basic approaches considered here (that is, Alexander-de Gennes or Milner-Witten-Cates). In the AdG case, first term in Eq. (1.10), which takes into account the translational entropy of the solvent, must be replaced by one term for each type of solvent so that the translational entropy of each solvent is taken into account. The second term, which takes the polymer-solvent interaction into account, must be replaced by one term for every possible solvent-solvent and polymer-solvent interaction which may occur. In addition, in order to determine the concentrations of each solvent within the polymer brush, one must ensure that the chemical potential of each solvent is equal inside and outside the brush. One of the most transparent formulations of the Alexander-de Gennes version of this theory can be found in [58]. Within the realm of mixed solvent models, the choice of the various solvent parameters can give rise to a number of different types of polymer behavior. In one case

which bears the most on this work, Birshtein *et al.* note the existence of what they term a "compositional phase transition" in which the polymer brush collapses due to solvent composition changes in the brush. In the self-consistent field formulation of this theory, similar modifications are made to the free energy density f in Eq. (1.25) as were made to the AdG free energy. In this case, one finds for certain parameter values discontinuities in the density profiles that connect two regions of nonzero monomer density [59]. This is related to the phenomenon of "preferential solvation" in which the concentrations of the various solvents can be significantly different inside and outside of the polymer layer [60]. This phenomenon is analogous to the preferential infiltration of attractive nanoparticles into a polymer brush which I will discuss in later chapters.

1.2.7 Polymers Interacting with Nanoparticles

Of particular interest here are the interactions of polymers with various molecular or macromolecular level additives, which we will generically refer to as "nanoparticles." Nanoparticles are added to polymers in a wide variety of applications. For example, anti-plasticizers can be added to polymer melts to alter their physical properties [61, 62], quantum dots or metallic particles can be added to polymers to create solar cells or organic electronic devices [63–67], and of course protein "nanoparticles" and "polymers" are crucial to the functioning of the NPC, as discussed in section 1.1, and are also relevant in biomimetic NPC-like devices [68–70].

Nanoparticles and other types of inclusions have been treated in a variety of ways in the literature. For example, Currie and coworkers considered the case of a polymer brush with adsorbed surfactants in the Alexander-de Gennes approach by using a free energy similar to that of Eq. (1.1) but including additional terms for the energy associated with the binding of monomers to the nanoparticles, the free energy of mixing, and a repulsive interaction between surfactant micelles [71]. As in the case of mixed solvent, in this study it was found that the polymer layer height makes a discontinuous jump as the adsorption energy of the surfactants was varied. Physically, at a certain critical value of adsorption energy, it becomes energetically favorable to increase the layer height in order to adsorb as many surfactants as possible while still keeping them sufficiently separated. This work was followed by a self-consistent field (SCF) treatment similar to that discussed in subsections 1.2.4 and 1.2.5 which showed monomer density profiles develop a discontinuity not unlike that of Fig. 7 except that instead of the monomer density dropping to

zero, the discontinuity connects two regions of nonzero monomer density. This is shown in Fig. 9. This was accompanied by a discontinuous loading of the brush, in which the micelles preferentially occupied the upper region of the brush [72]. Indeed the case of nanoparticles inside a polymer brush is closely related to the problem of mixed solvents in some cases. If the nanoparticles are envisioned to be quite small, one can view them as the constituents of one of the solvents, and it should not be surprising that the two cases give similar results. Of course, when the nanoparticles become larger, attempting to view them as a continuum solvent will become problematic.
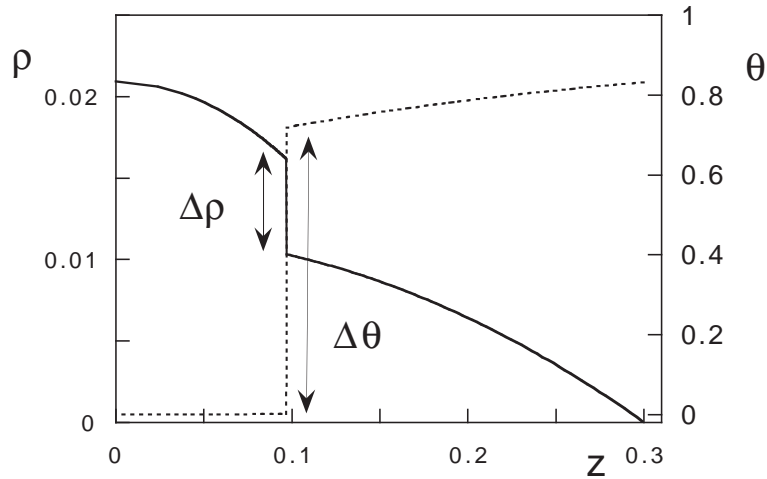
Figure 9: A figure from [72] showing a monomer density profile ρ (solid line) and the density profile of the surfactant micelles θ (dashed line). Under certain conditions, a discontinuity can develop in both profiles as surfactants preferentially occupy the high z region of the brush where repulsions between them are minimized.

In another important work by Kim and O'Shaughnessy an SCF theory for polymer brushes infiltrated by nanoinclusions of arbitrary size is presented [73]. In this theory, the free energy consists of terms accounting for polymer stretching and a requirement that space be filled with monomers and nanoparticles (in our language, $\psi + \phi = 1$). Notably absent in the theory is a direct interaction between nanoparticles and monomers, such as an adsorption energy or repulsion. It was found that nanoparticle penetration of the brush is sensitive to the nanoparticle size. For small nanoparticles, penetration into the brush is complete. As the nanoparticle size is increased, they are excluded first from the lower regions of the brush where the monomer density is higher, and finally are excluded from the brush entirely. The nanoparticle

size representing the crossover between the penetration and exclusion regimes is the blob size of the polymer brush (roughly the size of the fluctuations in polymer trajectories about the average path of the polymer). However, bear in mind that these results do not include direct nanoparticle-monomer interactions.

Other work has been performed for the case of large nanoparticles infiltrating a polymer brush, but typically the collapse of the brush is not considered. For instance, often the effect of only a single nanoparticle is considered (e.g. [74]), and it is sometimes assumed that the brush height remains unperturbed by the addition of nanoparticles (e.g. [75]).

1.3   LANGEVIN DYNAMICS SIMULATIONS

In addition to the analytical tools discussed in the previous section, this thesis will make extensive use of computational methods to explore the relevant systems to be studied. The use of computer simulations enable one to corroborate analytical findings and in some cases to probe parameters that are beyond the reach of analytical methods. Specifically, we will perform Langevin dynamic simulations, so we will begin with a discussion of the Langevin Equation. For additional details, the fortran code used to simulate the system may be found with this thesis as supplementary material.

1.3.1   The Langevin Equation

In Langevin dynamics, the motion of particles is governed by Newton's second law $\vec{F} = m d^2\vec{x}/dt^2$. In particular, we wish to consider Newton's second law for the case of a particle interacting not only with other particles, but also with a solvent or fluid. In principle, one could write down Newton's second law for all of the particles of interest as well as every particle of solvent. This is referred to as representing the solvent explicitly. On the other hand, one can avoid tracking the motion of solvent particles by representing them implicitly via their effect on the particle whose equation of motion we will consider. This is accomplished by regarding the net force on the particle of interest $\vec{F}$ to be composed of three contributions: (i) a deterministic force that results from the interaction of the particle of interest with other explicitly represented particles in the system, (ii) a random thermal noise due to the collision of the particle with small solvent molecules, and (iii) a frictional drag force due to the solvent.

When a particle is placed in a solvent, the random thermal motion of the solvent molecules gives rise to collisions between the particle and the solvent molecules. If the particle is significantly larger than the solvent molecules, these collisions will occur very frequently due to the large number of solvent molecules which are near the surface of the particle. These collisions result in a "jiggling" of the particle which is referred to as Brownian motion [40]. To avoid modeling the motion of the individual solvent molecules, one can model the combined effect of the collisions on the particle (excluding friction) via a random thermal force. This force $\vec{\eta}(t)$ is represented by a a stochastic function which has the properties that its time average is zero and its value at one time is not correlated to its value at earlier or later times [40, 76]. In other words,

$$\langle \vec{\eta}(t) \rangle = 0 \tag{1.31}$$

$$\langle \eta_i(t_1)\eta_j(t_2) \rangle = 2\gamma kT\delta(t_1 - t_2)\delta_{ij} \tag{1.32}$$

where γ is the friction coefficient of the particle and $i, j = x, y, z$. We will also assume the random noise function $\eta(t)$ is Gaussian, which means that the two moments Eqs. (1.31) and (1.32) are sufficient to define the properties of the distribution. In practice, we generate Gaussian random numbers $R(t)$ with unit variance using an algorithm based on Numerical Recipes [77], and multiply this by a prefactor which gives the proper standard deviation. Namely, the random forces can be obtained as [76]

$$\eta_i(t) = \sqrt{\frac{2\gamma kT}{\Delta t}}R(t). \tag{1.33}$$

Note that when time is discretized into steps of size Δt, the delta function in Eq. (1.32) should retain its integral of unity and so is replaced by $\delta_{t_1 t_2}/\Delta t$.

The second effect of the solvent is the frictional drag on the particle of interest. We assume that the friction is proportional to the particle's velocity and opposed to its motion, and therefore can be represented by a term $\vec{F}_f = -\gamma d\vec{x}/dt$. In practice, the value of the friction constant γ is important for the dynamics of the system but not for the equilibrium properties, achieved at long times under conditions of zero net particle flux. Since we will study the equilibrium properties only, for the present purposes the choice of γ is not important.

Including these two forces as well as a sum of the deterministic pairwise forces between the particle of interest, particle j, with other particles in the system, one obtains

$$\sum_{i\neq j} \vec{F}(\vec{r}_i, \vec{r}_j) - \gamma \frac{d\vec{x}_j}{dt} + \vec{\eta}(t) = m \frac{d^2 \vec{x}_j}{dt^2}. \tag{1.34}$$

This equation provides a second-order differential equation which can be solved numerically to obtain the trajectory of the particle $\vec{x}(t)$. Note that one could also include other forces here, such as an external force on particle j, but we will not consider that case here. We assume that the drag of the solvent is sufficiently strong that it removes the momentum of particles very rapidly (i.e., the overdamped limit). In this case, the inertial term $m\frac{d^2\vec{x}}{dt^2}$ can be neglected, and the equation obtained is

$$\sum_{i\neq j} \vec{F}(\vec{r}_i, \vec{r}_j) + \vec{\eta}(t) = \gamma \frac{d\vec{x}_j}{dt}. \tag{1.35}$$

This equation holds the advantage that it has been reduced to a first order differential equation. As such, one can calculate the sum of the deterministic forces on the particle at a time t, add to this the Gaussian random force generated according to Eq. (1.33), and use this force to update the components of the particle's position to their position at a time Δt later. Namely,

$$\left(\sum_{i\neq j} \vec{F}(\vec{r}_i, \vec{r}_j) + \vec{\eta}(t) \right) \frac{\Delta t}{\gamma} = \vec{x}_j(t + \Delta t) - \vec{x}_j(t). \tag{1.36}$$

This update procedure is performed on every particle in the system to update each particle's position from $\vec{x}(t)$ to $\vec{x}(t + \Delta t)$, then the entire process is repeated to increment time forward by another step Δt.

1.3.2 Simulations of Polymer Brushes

Before solving Eq. (1.35), one must decide upon the force fields that will be used to generate the deterministic pairwise forces between particles. One of the most ubiquitous and versatile of all molecular scale force laws is obtained from the Lennard-Jones (6-12) potential, which can be written as

$$U_{LJ} = 4\epsilon \left(\left(\frac{\sigma}{r} \right)^{12} - \left(\frac{\sigma}{r} \right)^{6} \right) \tag{1.37}$$

where r is the distance between particles, and σ and ϵ set the length and energy scales respectively. This potential provides a very strong repulsion at small r so that particles cannot overlap strongly, an attractive tail at large r which is suitable for modeling the van der Waals attraction between atoms (or qualitatively, other types of attractions), and a minimum point at $r_{min} = 2^{1/6}\sigma$ at which particles are bound with an energy ϵ. The LJ potential can be modified in order to remove the attractive tail if a purely repulsive force is desired. This modification and others can make the Lennard-Jones force suitable for modeling a wide range of physical phenomena.

Simulating polymer chains also requires the use of forces that will ensure the connectivity of the polymer chain. One of the most common choices is the finitely extensible nonlinear elastic (FENE) force which is given by

$$F_{FENE} = \frac{-kr}{1 - \left(\frac{r}{\ell_{max}} \right)^{2}}$$

where r is the distance between particles, ℓ_{max} is the maximum extension of the spring, and k is the spring constant [78]. The FENE force is approximately proportional to r at small r and thereby represents a spring-like potential. Unlike an ordinary Hooke's Law spring, the restoring force becomes super-linear in r if the spring is stretched too far. This is important because polymers cannot be stretched infinitely. They have some contour length beyond which stretching them becomes very difficult. In addition, one can use this maximum extension to ensure that adjacent monomers never become so spread apart that there is empty space along the polymer backbone, which would allow chains to cross and pass through each other.

In addition, our simulations require the polymer brush to be coupled to a solution of nanoparticles. We have accomplished this through two different methodologies which gave equivalent results in all instances in which they were compared. The first method, which we refer to as a grand canonical approach, involves making the "ceiling" of the simulation box an absorbing boundary for the nanoparticles, but introducing a

constant (modulo fluctuations) flux of nanoparticles into the box. Once equilibrium is reached, the flux of particles out of the box stabilizes at (on average) a level that is equal to the (fixed) flux into the box. This produces a constant concentration of nanoparticles in the polymer layer and above the polymer layer. This is equivalent to coupling the simulation box to a reservoir at fixed nanoparticle concentration (or chemical potential). Each flux of nanoparticles into the box corresponds to one value of the nanoparticle concentration in solution.

In certain cases, dramatically different morphologies of the polymers were observed for almost identical solution nanoparticle concentrations. (This will be discussed in chapter 2.) In this case, using the nanoparticle concentration as a control parameter produced some practical difficulties, so we sometimes use a canonical ensemble method. In this case, the ceiling of the simulation box is a reflecting boundary, and the number of nanoparticles in the simulation box is fixed. These nanoparticles will partition between the polymer layer and the region outside of the polymer layer according to the energetics of the system. After equilibrium is reached, the concentration of nanoparticles is measured. That is, the total number of nanoparticles, rather than their concentration, is the control parameter. This methodology is better suited to situations in which the system is very sensitive to the nanoparticle concentration. As expected, the two different ensembles produces the same results in those instances where a comparison was possible.

1.4 SUMMARY

In summary, much is known about polymer brushes. Brushes have been analyzed using simple Alexander-de Gennes type theories, which assume a homogeneous concentration of monomers throughout the brush, and using more sophisticated models from which density profiles of the monomers can be extracted. From both of these approaches, one can obtain the standard brush scaling relationship which states that the height of the brush above the grafting surface h is related to the number of monomers in the polymer chain N and the grafting density of the chains $\sigma = 1/a^2$ according to $h \sim N\sigma^{1/3}$. In addition to this, Milner-Witten-Cates theory shows that the density profile of the monomers is a downward-facing parabola with its maximum value at the grafting surface. More sophisticated generalizations of these theories also exist, such as Green's function based self-consistent field models [79–81], but the primary conclusions of the simpler models prove to be essentially correct.

The case of brushes in solvents has also been considered. In this case the monomer-solvent interaction must be included, but such models are fundamentally similar to their predecessors. In these models, one finds that the solvent may have the effect of swelling or compressing the polymer brush. For the case of good solvent, the swelling of the brush does not disrupt the scaling relationship $h \sim N\sigma^{1/3}$ and the brush is still parabolic. In poor solvent, the brush may collapse, in which case the volume of the brush scales with N. The collapsed brush may result in a discontinuous density profile in which the brush suddenly terminates at $z = h$.

A brush in mixed solvents may also compress and swell, but in this case more exotic effects are possible such as a preferential occupation of one solvent in the brush. This can also result in discontinuities in the density profiles, but much depends on the detailed parameter choices since each solvent can interact with the polymers and with each of the other solvents.

Brushes with "nanoparticles" (that is, some type of inclusions or foreign particles) have also been studied, but less extensively. When the nanoparticle size is on the order of the solvent molecule size, the nanoparticles behave in a way similar to a second solvent, causing, e.g., a preferential expulsion of the nanoparticles from the brush as in Fig. 9. Typically when their large size is taken into account, simplifying assumptions are made that preclude a collapse of the brush or other exotic morphology change.

In the following two chapters, I will consider the problem of a polymer brush infiltrated by nanoparticles which bind to the monomers. In chapter 2, which was published as [82], I consider the case where the nanoparticles are similar in size to a monomer and I use the simpler Alexander-de Gennes approach. In chapter 3, which was published as [83], I consider the case of larger nanoparticles and use an approach similar to Milner, Witten, and Cates [46]. In both cases, I find that a collapse of the brush is possible, as are discontinuities in the monomer and nanoparticle density profiles. In chapter 4, I apply these theoretical tools to examine the results on the system of the Nuclear Pore Complex, where a collapse-based mechanism is one possible candidate for nucleocytoplasmic transport.

2.0 THE MORPHOLOGIES OF POLYMER BRUSHES INFILTRATED BY SMALL NANOPARTICLES USING ALEXANDER-DE GENNES THEORY

2.1 INTRODUCTION

Alongside traditional bulk polymeric materials such as rubbers and plastics, thin surface films of polymers have become important in many technological applications, such as sensors, lubricant coatings, light-emitting devices, nonlinear optics and more. Thin polymer films decorated with nanoparticles form a novel class of "responsive" composite materials allowing one to design the function and to control the morphology of the films in nanotechnological applications such as solar cells and programmable memory devices. One major technological challenge is the precise control and engineering of the properties of such composites [63, 84–91].

In the biological context, polymer-like molecules (such as natively unfolded, disordered proteins) confined near or attached to surfaces interacting with nano-size particles (such as proteins) play important roles in many processes [92–97]. For instance, binding of certain transport proteins is thought to induce reversible morphological changes in the layer of natively unfolded proteins lining the channel of the nuclear pore complex in eukaryotic cells, and such morphological changes are at the core of the transport mechanism of this very important biological "device" [34, 93, 97, 98]. In another example, binding of proteins and proteoglycans to the layer of hyaluronic acid molecules that coat cartilage cells regulates the mechanical properties of the cartilage [99]. Some of the structural and functional aspects of such biological systems can be reconstituted *in vitro* with the purpose of studying the basic mechanisms of their function, as well as for developing bio-mimetic nanotechnological applications, such as nanofilters and biosensors [68–70, 84, 100].

Understanding various morphologies of polymer nanoparticle mixtures at surfaces is therefore important for the predictive design of novel materials and devices as well as for the mechanistic understanding

of important biological processes. These goals require predictive, quantitative theoretical understanding of the underlying physics of grafted polymers infiltrated by nanoparticles in order to bridge the gap between experimental results in controlled situations and predictions in realistic regimes, which might not be directly accessible experimentally. The behavior of single-component grafted polymer films, known as "brushes", has been extensively studied, and a comprehensive theoretical framework explaining the experimental phenomena has been developed (e.g.[37, 45, 46, 75, 101–104]), providing the foundation for the present work. Brush morphologies can be controlled, for instance, by changing the solvent quality or by manipulating the direct polymer-polymer interactions [45, 50, 75, 89, 102–104]. However, the effect of the addition of nanoparticles has been much less studied. In the case of only excluded volume interactions between the polymers and the nanoparticles, Kim and O'Shaughnessy [73, 105] studied theoretically the effect of particle size on their penetration and assembly into polymer brushes. Similar ideas were explored by Binder and coworkers [102] via Brownian dynamics simulations. More recently Halperin *et al.* [75] studied the additional effect of weak attractions between the nanoparticles and polymers on the brush structure, along with the variation of the solvent quality. In related systems, three dimensional structures of mixtures of block copolymers with nanoparticles have been studied in [106, 107].

In this chapter, motivated by several technologically and biologically important systems [33, 34, 63, 85, 86, 89, 93, 108], we study the effect of specific attractive interactions (binding) between grafted polymers and small particles that may infiltrate the polymer layer. In particular, we study the effect of these small nanoparticles on the film morphology, using mean field type analytical theory supported by Langevin dynamics simulations.

One particular motivation for our work is the controversy regarding possible morphological changes in the layers of natively unfolded constituents of the nuclear pore complex induced by the binding of other folded proteins [34, 35]. Our model, in its present form, is not directly applicable to this system due to the relatively large nanoparticles involved in the latter. Our primary goal here is to establish how the properties of a polymeric layer, such as its height and composition, depend on the concentration of nanoparticles present in it, the strength of their interaction with the polymers and the parameters of the layer such as the grafting density. We show that such attractive interaction can result in sharp large scale changes in the layer structure, allowing global control of the polymer layer morphology and geometry, as well as nano-particle positioning within the layer. This result is qualitatively consistent with observed

behavior for real nanoparticle systems such as that studied in Ref. [34] in which a substantial decrease in the height of grafted polymer was observed upon addition of the binding "nanoparticles." In addition, it provides a foundation on which to construct more elaborate models.

2.2 THE MODEL

We consider a layer of N_p flexible polymeric chains, each containing N monomers. Each chain is grafted at one end to a planar surface of area A at a distance a from its nearest neighbors. The polymer layer is in equilibrium with a solution of nanoparticles of concentration c that interact attractively with the monomers of the chains. The particles can penetrate the polymer layer, thereby changing its properties such as its density and the height above the grafting surface h - see Fig. 10 for illustration; we denote the number of nanoparticles in the layer as N_{np}. For simplicity, here we consider the nanoparticles to be of the same size as the chain monomers. With an appropriate choice of monomer size, these particles may be thought of as representing small nanoparticles (perhaps $\sim 1 - 3nm$ in diameter) interacting with polymer chains, as any other small additives which may penetrate a polymer layer, or as constituents of a mixed solvent. As discussed in Section 2.5, the conclusions of the mean field theory discussed below are also expected to hold for somewhat larger particles.

The layer height h is not dictated by the polymer length alone, but is established as a result of the minimization of the total free energy of the system that depends on several salient factors: entropic stretching of the polymers, steric repulsion between the monomers, and the interactions of the polymers with the nanoparticles.

A simple mean field free energy of such a layer, per unit area in units of $k_B T$ can be derived, for example, using a lattice construction [44, 46, 110], as explained in Appendix A. The result is

$$F(\psi, h)/A = \sigma h^2/(2N) + \tag{2.1}$$
$$+h \left(\phi \ln \phi + (1 - \phi - \psi) \ln(1 - \phi - \psi) + \chi \phi \psi\right)$$

where $\sigma = N_p/A = 1/a^2$ is the polymer grafting density, $\phi = N_{np}/(Ah)$ is the density of the nanoparticles and $\psi = N_p N/(Ah) = \sigma N/h$ is the monomer density; all lengths are measured in units of the
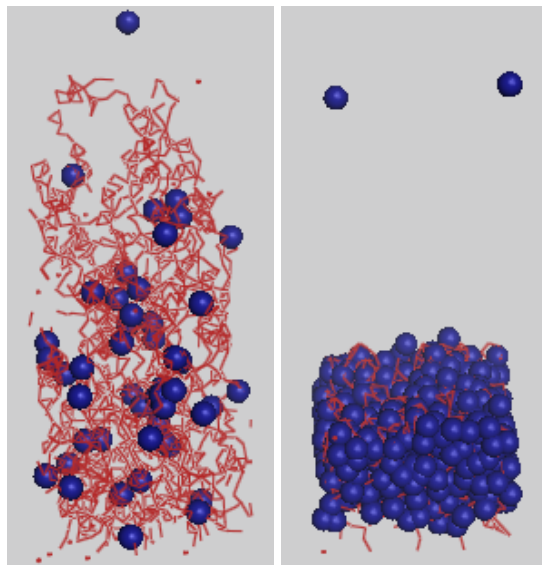
Figure 10: Snapshots of the Langevin simulations illustrating the first-order collapse of the polymer layer upon addition of the nanoparticles. The nanoparticles are shown as blue circles. Polymer chains, grafted from below onto a flat surface (not shown), are depicted in line format (i.e., their bead-spring structure is not resolved here). *Left panel:* The layer in the extended swollen state just below the transition; $c = 6.9 \times 10^{-5}$. *Right panel:* The collapsed layer packed with nanoparticles, just above the transition; $c = 2.4 \times 10^{-4}$. $\epsilon_b = 2$ and $a = 4$ for both panels. Snapshots were visualized using PyMOL [109].

monomer size b. The first term represents the entropic stretching of the polymers, under the assumption that the monomer density is a step function, as in the Alexander-deGennes model [37, 46]. The real monomer density distribution within the brush is closer to parabolic [46, 104, 111], but we will see that the predictions of this relatively simple model are in very good agreement with simulations for the quantities we are interested in. The second term represents the translational entropy of the nanoparticles within the layer, and the third term is the correction to the translational and configurational entropies due to excluded volume effects. Together, these three terms account for the entropy of all possible arrangements of the polymers, nanoparticles, and empty sites (which are implicitly assumed to be filled with athermal solvent) [110]. Other approximations for the free energy that express similar physics are possible [44, 110]; they result in qualitatively similar predictions. The last term in Eq. (2.1) describes the direct interaction between the nanoparticles and the polymers, where χ is proportional to the microscopic

energy of the particle-polymer interaction (see Section 2.4). We will focus on the case of $\chi < 0$, which corresponds to attractive interactions. The arguments so far are standard. In the absence of the interaction term, in the small density expansion, the free energy (2.1) reduces to the standard Alexander-deGennes polymer brush [46]. As we will be interested also in moderately high concentration regimes, we keep the full expression for the logarithmic term, which ensures incompressibility when $\psi + \phi \to 1$, i.e., when the polymers plus the nanoparticles occupy all the available volume.

The values of the variables h and ϕ are determined as sketched below. The chemical potential of the nanoparticles in the layer is, from Eq. (2.1):

$$\mu_{np} = \frac{\partial F/A}{h \partial \phi}\Big|_{h=\text{const}} = \chi\psi + \ln\left(\phi/(1 - \phi - \psi)\right). \tag{2.2}$$

The osmotic pressure of the layer is

$$\Pi = -\frac{dF/A}{dh}\Big|_{\phi h=\text{const}} = \chi\phi\psi - \frac{h\sigma}{N} - \psi - \ln(1 - \phi - \psi). \tag{2.3}$$

Because the nanoparticles are free to diffuse between the polymer layer and the bulk solution, in equilibrium their chemical potential in the layer, μ_{np} must be equal to the chemical potential μ_c of the nanoparticles in the solution above the layer. The osmotic pressure of the layer Π and of the solution Π_c must be equal as well. Assuming ideal solution, $\mu_c = \ln(c/(1-c)) \simeq \ln(c)$ and $\Pi_c = -\ln(1-c) \simeq c$. These two conditions determine the two unknowns: the layer height h and the concentration of the nanoparticles in the layer ϕ. These equilibrium conditions are equivalent to the minimization of the global thermodynamic potential $\Phi(c, h, N_{np}) = F(h, N_{np}) - \mu_c(c)N_{np} + \Pi_c(c)Ah$ over layer height h and the number of the nanoparticles in the layer, $N_{np} = \phi h$, when c is fixed ("grand canonical"), or the minimization of an appropriate "canonical" free energy when the total number of nanoparticles in the system is fixed instead. These two cases may correspond to different experimental situations.

2.3 SIMULATIONS

The mean field theory was augmented and verified via overdamped Langevin dynamics simulations [112–114]. In these simulations, the polymers are represented as chains of beads kept on the strand by finitely extensible, nonlinear, elastic (FENE) springs [112], which exert a force of the form

$$F_{FENE} = \frac{-kr}{1 - \left(\frac{r}{\ell_{max}}\right)^2}$$

on the nearest neighbor beads of the chain, where k is the spring constant, r is the distance between beads, and ℓ_{max} is the maximum separation of beads, at which the FENE restoring force becomes infinitely strong. The nanoparticles are modeled as freely diffusing beads. All beads, both the monomers of the polymers and nanoparticles, interact through a pairwise 6-12 Lennard-Jones type potential [113] of the form

$$U(r) = \begin{cases} \epsilon \left(\left(\frac{b}{r}\right)^{12} - 2 \left(\frac{b}{r}\right)^6 \right) + \epsilon - \epsilon_b & r < b \\ \epsilon_b \left(\left(\frac{b}{r}\right)^{12} - 2 \left(\frac{b}{r}\right)^6 \right) & r > b \end{cases} \tag{2.4}$$

which models short range molecular interactions. $\epsilon_b = 0$ for polymer-polymer interactions and nanoparticle-nanoparticle interactions, representing a short-range repulsion with the effective hard core diameter b and the excluded volume $\sim b^3$. For polymer-nanoparticle interactions, positive ϵ_b corresponds to attraction. Note that varying ϵ_b does not affect the excluded volume size b or the strength of the hard core repulsion interaction energy ϵ. Dynamically, in simulations each bead performs diffusion under the action of the deterministic forces from all other beads and the random thermal force [112, 113]. Each chain is grafted at one end to a wall at $z = 0$, z being the perpendicular distance from the wall. The wall itself is modeled by another purely repulsive potential of the shape of Eq. (2.4) with $\epsilon_b = 0$ and $r = z$, centered at $z = 0$. In all simulations chains of length $N = 100$ were grafted onto a square lattice at a distance $a = 4b$ or $a = 3b$ from each other, in a 4×4 or 6×6, array. Periodic boundary conditions were used in the in-plane directions. The simulations were performed with two types of boundary conditions on the top of the box: one corresponding to a reservoir of nanoparticles with fixed concentration (grand-canonical ensemble with respect to particle number), the other with a fixed number of particles in the simulation box (canonical ensemble). The two different boundary conditions were found to agree in regimes of parameter space where a comparison was possible. The brush height was measured by creating time-averaged histograms of the monomer density as a function of z, and marking

35
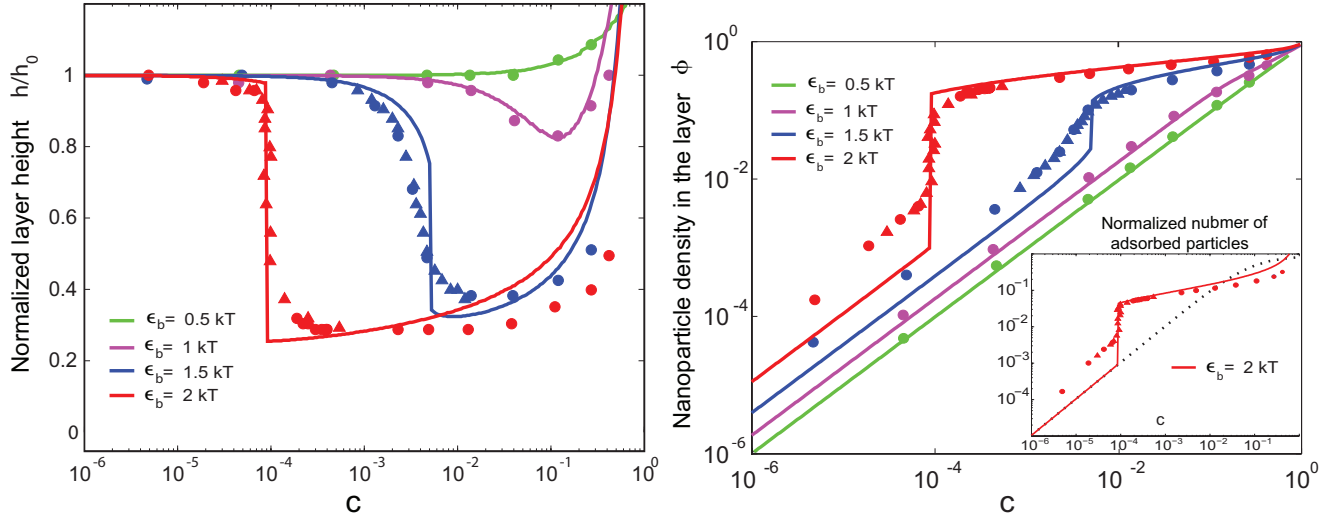
Figure 11: *Left panel:* Layer height, h, normalized by the height in the absence of nanoparticles, h_0, as a function of the concentration of the free nanoparticles in solution, c, for different interaction strengths. *Right panel:* Average nanoparticle density in the layer as a function of c for same interaction strengths as in the upper panel. The inset shows the number of adsorbed particles, per unit area, compared to a simple Langmuir adsorption isotherm (dotted line). In both panels the solid lines are the mean field theory, filled dots - corresponding grand-canonical simulations, filled triangles - canonical simulations. In both panels the grafting distance is $a = 4b$.

the top of the brush as the z value at which the monomer density became negligible. Once h was determined from the monomer density profile, all nanoparticles with $z < h$ were considered bound in the layer, and those with $z > h$ were considered to be in solution. The simulations were tested by comparing with known cases in the absence of nanoparticles [101].

2.4 RESULTS

The main result of the modeling is that the layer height, as well as its composition and morphology are very sensitive to the number of added nanoparticles and the strength of their interactions with the
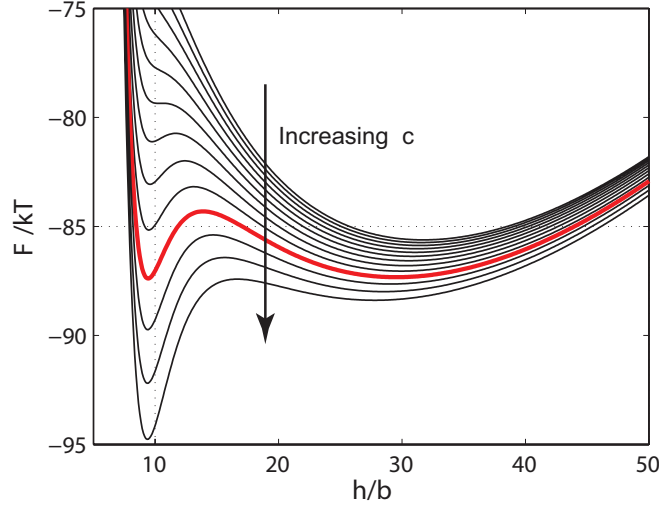
Figure 12: The total thermodynamic potential Φ vs. polymer layer height h for $a = 4$, $N = 100$, $\chi = -10$, and $10^{-4} < c < 10^{-2}$. The development of a minimum of the free energy (global thermodynamic potential) Φ at low values of h reflects the first order transition as the nanoparticle density is increased. At approximately $c = 1.2 \times 10^{-3}$ (shown via the bold red line), the two minima are equal in energy.

polymers. These results are summarized in Fig. 11 and illustrated in Fig. 10. For sufficiently strong interactions, increasing nano-particle concentration from zero causes the polymer layer to compress. At still higher concentrations, the trend is reversed and further addition of nanoparticles results in the swelling of the layer.

Notably, the nature of the compactification of the polymer layer is different at high and low interaction strengths $\chi(\epsilon_b)$. For weak attraction, above a critical value χ_c, and low to moderate c, the layer height h decreases continuously with the concentration of nanoparticles c, while for $\chi < \chi_c$ and an appropriately chosen range of c, the layer undergoes an abrupt, first order transition from an extended, low density state to a high density collapsed film packed with nanoparticles as shown in Fig. 11. This abrupt collapse is accompanied by a corresponding discontinuous increase in the number of nanoparticles adsorbed within the layer, as shown in Fig. 10 and the right panel in Fig. 11.

The results of the mean field theory are in very good agrement with simulations, as shown in Fig. 11. The interaction parameter χ is fitted as $\chi/(b^3 kT) = -8.45(\epsilon_b/kT) + 4$, consistent with the ef-
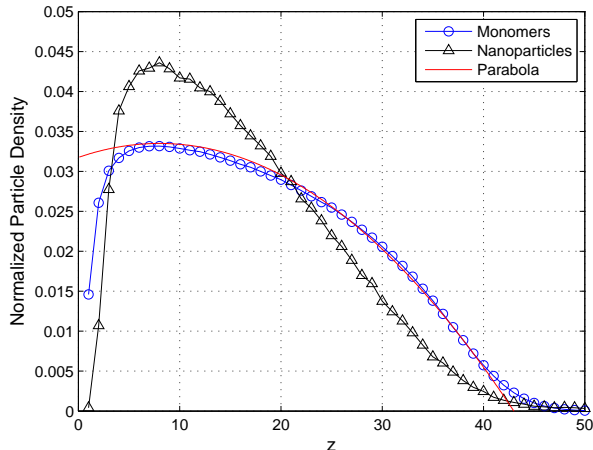
Figure 13: Time averaged histograms of the monomers' and nanoparticles' height above the grafting surface for parameter values for which few nanoparticles are bound to the brush. The monomer density profile is nearly parabolic as expected for a brush with no nanoparticles. The red line shows a parabola to guide the eye. Both profiles were generated for $a = 4$, $\epsilon_b = 2$, $c = 4.2 \times 10^{-5}$. The area under both data curves is normalized to unity.

fective interaction range of $2b$ [114]; it is also closely related to the second virial coefficient of the polymer-nanoparticle interaction potential (2.4) [40], $\chi \simeq \frac{1}{2} \int d^3 r (e^{-U(r)} - 1)$. Simulations also provide information about the internal structure of the layer.

The heuristic physics behind this behavior is simple: penetration of the nanoparticles increases the number of energetically favorable contacts between the polymer and the nanoparticles. This helps to overcome the entopic loss due to excluded volume interactions in the high density layer. At low particle concentrations, nanoparticles penetrate the porous, swollen texture of the unperturbed layer, causing the layer to condense around them, decreasing the volume of the layer. By contrast, at higher nanoparticle concentrations, the already dense, collapsed polymer layer has to increase its volume in order to accommodate as many nanoparticles as possible. The observed transition is expected to lie in the same universality class as an ordinary liquid-gas transition [115], which is apparent from the analysis of the thermodynamic potential Φ: as the nanoparticle concentration c increases, the global minimum of Φ discontinuously switches from a high value of the layer height h to a low one (see Fig. 12).
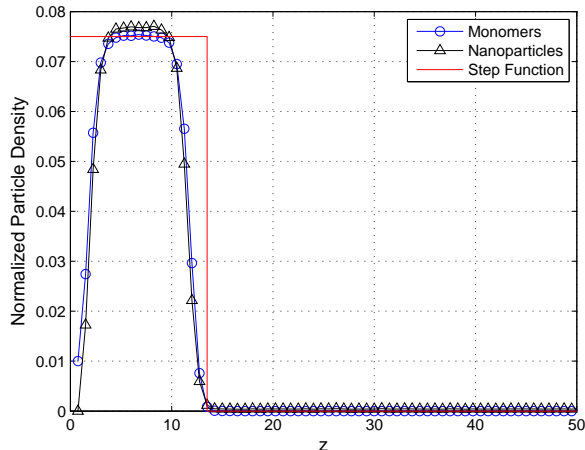
Figure 14: Time averaged histograms of the monomers' and nanoparticles' height above the grafting surface for parameter values for which many nanoparticles are bound to the brush. The red line shows a step function which drops to zero at the measured value of h. The density profiles are close to step functions because monomers and nanoparticles are tightly packed as in a solid. Both profiles were generated for $a = 4$, $\epsilon_b = 2$, $c = 2.3 \times 10^{-3}$. The area under both data curves is normalized to unity.

Besides confirming the general picture supplied by the mean field theory, simulations provide additional information about the particle distribution within the layer. When the nanoparticle concentration is small enough that they constitute only a small perturbation on the standard polymer brush, the monomer density profile is approximately parabolic as seen in Fig. 13. The height of the brush is approximately the intercept of the fit parabola as shown in Fig. 13. Although our MFT takes the monomer density to be constant throughout the polymer layer, the density profile obtained in simulations matches the expected behavior of a plane-grafted brush [41, 46], including the presence of a depletion region near the wall and a "foot" at high z in simulations [101, 116].

When the attraction between nanoparticles and polymers is sufficiently strong and the nanoparticle concentration is sufficiently high, the brush becomes highly compact, and space is almost completely filled with nanoparticles and monomers. That is, the monomer density profile becomes approximately a step function as seen in Fig. 14. Of course in simulations the step is not infinitely sharp, but instead includes a transition region of intermediate monomer concentration. We include this intermediate region

as part of the brush when calculating the height.

The corresponding nanoparticle density profiles can also be seen in Figs. 13 and 14. In both cases, the nanoparticle density profile for $z < h$ qualitatively tracks the monomer density profile because nanoparticles in the polymer layer are expected to be bound to one or more monomers.

2.5   DISCUSSION

To summarize, we have found that the morphology and composition of surface layers of polymers can be controlled by addition of attractive nanoparticles. In particular, we have uncovered the possibility of a novel first order transition between a low density swollen layer and a high density compact state, triggered by either the increase in the concentration of the nanoparticles or the increase in the interaction strength.

Although we present the case of monomer-size particles only, the results of this study are more broadly useful for several reasons. Firstly, this approach creates a useful foundation on which to analyze more complicated cases, and many of the same physical arguments made here hold for particles larger than the monomer units as well. The appropriate free energy analogous to Eq. (2.1) can be derived on the mean field (MF) level with minor modifications to the lattice gas argument (or other phenomenological arguments) used to derive Eq. (2.1), and a similar comparison to simulation may be carried out, as will be discussed in Chapter 3. For larger particles, especially when their size exceeds the "blob" size, a characteristic length scale of the brush which is roughly equal to the grafting distance [37], additional effects not included in a simple mean field theory, might become important. Such effects include corrections to the configurational entropy of the polymers, arising from either adsorption onto the surface of the larger particles or meandering around them, depletion interaction between large particles induced by the smaller monomers and crystallization of large particles [73, 105–107, 117, 118]. The exact shape of the density profile might be important for precise determination of the particle distribution within the brush and more sophisticated theories such as self-consistent field theory (SCFT) might be needed [46, 73, 111, 119]. However, preliminary simulations with larger nanoparticles show that the qualitative predictions of the simple MF theory hold even for larger nanoparticles. This is in accord with the general understanding that for particles of size smaller than the blob size, additional effects such as polymer stretching are sub-

dominant [73, 102, 105, 120]. A systematic discussion of the effects of the particle size and the above mentioned issues will be presented elsewhere. Secondly, consideration of monomer-sized nanoparticles may be directly applicable to realistic situations, particularly if one imagines a coarse-grained approach in which one monomer is a nano-scale moiety composed of several amino acids or other chemical units. In fact, the simulations carried out in Section 2.3 are, by nature, coarse-grained, and, provided the polymers under consideration are sufficiently flexible, the monomer size b need not be taken on the atomic scale.

Good agreement between the simple mean field theory and the simulations suggests that the theory does capture the essential complexity of the problem. Our results suggest strategies for the control of morphologies of composite materials for practical applications. The insights from the model also inform future analysis of biological systems such as interactions of unfolded polypeptides with nanoparticle-like objects such as proteins [34, 121]. Also, the described transition is mathematically similar to the "bistable switch", which is an important part of many biological control circuits [122]. Finally, the discontinuous dependence of the number of the nanoparticles in the layer on their concentration in the bulk has important implications for the estimation of the binding affinities between flexible objects such as unfolded proteins [92].

3.0 THE MORPHOLOGIES OF POLYMER BRUSHES INFILTRATED BY VARIOUS SIZES OF NANOPARTICLES BY MILNER-WITTEN-CATES THEORY

3.1 INTRODUCTION

Binding and intercalation of nanoparticles or other nano-sized objects to polymer layers grafted to surfaces is a common motif in nanotechnology and surface science and engineering [63, 64]. For instance, the collapse and extension of polymer layers grafted to the walls of nano-channels are used technologically for molecular valves and sieves [123, 124], drug delivery devices [125], and lubrication of surfaces [126]. Nano-inclusions and other additives can be used to control the specific morphologies crucial to the operation of devices such as solar cells and to create responsive materials through manipulation of the polymer-nanoparticle interactions [63–67]. Industrially, the physical properties of polymer materials can be manipulated by the binding of ungrafted polymers to small attractive additives, and this process can cause a reduction in the system volume [61, 62]. Polymer brushes are also used to prevent and manipulate protein binding to surfaces [127, 128].

Morphological transitions of flexible filaments induced by binding of nano-sized particles are also important in several biological processes. For example, hyaluronic acid, which is important to the functioning of cartiliage and skin, can undergo significant changes in volume when bound to proteoglycans [99]. In the Nuclear Pore Complex, binding of transport proteins may cause conformational changes in the unfolded proteins within the pore, facilitating nucleocytoplasmic transport of cargos [31, 34, 36, 121, 129]. Biomimetic devices based on the functional properties of such biological systems like have been created [68–70].

Grafted polymers in the absence of nanoparticles have been well-studied, both theoretically and experimentally, and the properties of such polymer "brushes" are well-established [37, 41, 46, 47, 81, 101, 116, 130–132]. Physically, the height of a brush is determined by the balance between the stretching

entropy of the polymers, which favors more compact conformations, and the excluded volume interaction between the polymers, which favors less compact conformations. The height and morphology of the brush can be modulated by changing the quality or the composition of the solvent or mixture of two or more solvents in contact with the brush or by the addition of small nanoparticles, whose size is of the order of the monomer size [45, 49–57, 71, 72, 82, 133].

However, the behavior changes for larger nanoparticles whose size exceeds the monomer size, and the morphological changes undergone by the polymers when they bind nano-sized objects are still not well-understood. Penetration of polymer brushes by large nanoparticles that do not bind or are repelled by the polymers has been studied by self-consistent field (SCF) calculations and computer simulations [73, 102, 105, 118, 127, 134]. It has been shown that weak attractive interactions between the nanoparticles and the polymers allow large nanoparticles to penetrate the brush [74, 75, 135]. However, the changes in the overall morphology and the height of the layer, and in particular collective and cooperative effects arising from binding multiple particles simultaneously, were not considered.

In this chapter, we investigate the morphological changes of plane-grafted polymer layers induced by binding of attractive nanoparticles of various sizes and interaction strengths. Using a self-consistent field theory approach augmented by Langevin Dynamics simulations, we find that the nanoparticles modulate the height and the morphology of the layers. Depending on the nanoparticle size, nanoparticle concentration, polymer grafting density, and polymer-nanoparticle interaction strength, a wide range of behaviors is observed, including nanoparticle-induced layer collapse and swelling. Nanoparticles can produce highly inhomogeneous stratified morphologies in which they form a band near the grafting surface, or they can fail to fully penetrate the layer and stay in the region of sparse polymer density far from the grafting surface. Features such as the sharpness and degree of the collapse in layer height depend on the nanoparticle size, interaction strength and the polymer grafting density.

3.2 THEORY

In this section, we develop a model of a layer of grafted polymers in equilibrium with a solution of large attractive nanoparticles using a variant of a self-consistent field theory (SCFT) [41, 46, 47, 81].

The state of the system is characterized by the collection of all polymer trajectories in space and by the

43

location of all nanoparticles. We denote the trajectory of a polymer chain α as $\vec{r}_\alpha(s)$, where $0 \le s \le N$ is the position of a monomer along the chain backbone, so that the local monomer volume fraction at a position $\vec{r}$ is $\psi(\vec{r}) = b^3 \sum_\alpha \int_0^N ds\, \delta(\vec{r} - \vec{r}_\alpha(s))$ where b is the monomer diameter. Similarly, we denote the local volume fraction of the nanoparticles at a position $\vec{r}$ within the brush $\phi(\vec{r}) = v \sum_i \delta(\vec{r} - \vec{r}_i)$ where v is the nanoparticle volume and the sum is over all nanoparticles [46, 73]; the volume fraction of the nanoparticles in the solution, c, is constant.

In units of kT, the grand canonical free energy (or, equivalently, generalized Edwards Hamiltonian [45]) of the brush for a given set of monomer and nanoparticle coordinates is given by a functional of the following form [41, 46, 47]:

$$
\begin{aligned}
F[\{\vec{r}_\alpha(s)\}] \;=\; & \sum_\alpha \frac{1}{2b^2} \int_0^N ds \left(\frac{\partial}{\partial s} \vec{r}_\alpha(s) \right)^2 \\
& + \frac{1}{b^3} \int d^3 r (f(\psi(\vec{r}), \phi(\vec{r})) - \frac{1}{\bar{v}} \mu_c \phi(\vec{r}))
\end{aligned}
\tag{3.1}
$$

The first term describes the stretching entropy of the polymers, $f(\psi, \phi)$ is the local free energy density due to all other effects, such as the excluded volume and other interactions between the polymers and nanoparticles, and the last term takes into account the fact that the layer is coupled to a (dilute) solution of nanoparticles with the chemical potential $\mu_c = \ln(c/(1-c))$. In this term $\bar{v}$ is the ratio of the nanoparticle volume to the monomer volume.

The non-elastic local free energy density $f(\psi(\vec{r}), \phi(\vec{r}))$ can be obtained from a lattice gas model [44]. Details of this derivation can be found in Appendix A. The result is

$$
\begin{aligned}
f(\psi, \phi) = (1/\bar{v})\{ & \phi \ln \phi + (1 - \bar{v})(1 - \phi) \ln[1 - \phi] \\
& + \bar{v}(1 - \psi - \phi) \ln[1 - \psi - \phi] + \chi \phi \psi \}
\end{aligned}
\tag{3.2}
$$

where χ characterizes the monomer-nanoparticle binding and depends on both the binding strength and the nanoparticle size. $\chi < 0$ corresponds to attractive monomer-nanoparticle interactions.

At equilibrium, the free energy functional (3.1) is minimized over the nanoparticle density $\phi(\vec{r})$ and the polymer trajectories $\{\vec{r}_\alpha\}$. Carrying out first the minimization over $\phi(\vec{r})$ yields a constraint that relates the local nanoparticle volume fraction at equilibrium $\phi_{eq}(\vec{r})$ to the monomer volume fraction $\psi(\vec{r})$. Namely,

$$
\mu_c = \chi \psi + \ln \left(\frac{\phi_{eq}(1 - \phi_{eq})^{\bar{v}-1}}{(1 - \psi - \phi_{eq})^{\bar{v}}} \right).
\tag{3.3}
$$

44

For arbitrary $\bar{v}$, Eq. (3.3) can be solved numerically, but at $\bar{v} = 1$, which corresponds to equal size monomers and nanoparticles, $\phi_{eq}(\psi)$ may be obtained analytically.

Further minimization of the free energy functional over the $\vec{r}_\alpha(s)$'s gives, for each polymer,

$$-\frac{1}{b^2}\frac{\partial^2}{\partial s^2}\vec{r}_\alpha(s) + \frac{\partial}{\partial\vec{r}_\alpha}\mu(\psi) = 0, \tag{3.4}$$

where

$$\begin{aligned}\mu(\psi) &= \frac{\partial}{\partial\psi}f(\psi, \phi_{\text{eq}}(\psi)) \\ &= -\ln(1 - \psi - \phi_{eq}(\psi)) + \frac{\chi}{\bar{v}}\phi_{eq}(\psi) - 1.\end{aligned} \tag{3.5}$$

A more detailed derivation of Eqs. (3.3) and (3.4) can be found in Appendix C. The equations (3.4) and (3.5) must be solved self-consistently (numerically) in order to determine the $\vec{r}_\alpha$'s and the $\psi(\vec{r}_\alpha)$'s. However, it has been noted [46] that when the density is uniform in the lateral direction, so that the densities are only dependent on the distance from the grafting surface z, Eq. (3.4) becomes mathematically identical to the Newtonian equations of motions of particles moving in the one-dimensional potential $-\mu(\psi(z_\alpha))$ over the time interval $[0, N]$. The untethered end of each grafted polymer chain starts from a different initial position $z_\alpha(0)$ with zero "velocity" $\partial z_\alpha(0)/\partial s = 0$ and reaches the final position $z_\alpha(N) = 0$ (the grafting surface) in the same "time" N. The only potential possessing such a property is the harmonic potential so that

$$\mu(\psi(z)) = A - Bz^2 \tag{3.6}$$

where $B = \pi^2/(8b^2N^2)$ [41, 46].

The monomer density profile $\psi(z)$ is determined by inverting Eq. (3.6) after making use of Eqs. (3.3) and (3.5), and the normalization condition

$$N\sigma = \int_0^h dz\psi(z) \tag{3.7}$$

where σ is the grafting density of the polymers and h is the height of the polymer layer above the grafting surface. The parameter A in Eq. (3.6) is adjusted so that Eq. (3.7) is satisfied, a procedure which could be phrased alternatively in the language of Lagrange multipliers [47, 135].

When the magnitude of the nanoparticle-monomer interaction parameter χ is sufficiently small, $\mu(\psi)$ is a monotonically increasing function of ψ over the entire range of solution nanoparticle volume fraction

$0 < c < 1$. In this regime, the spatial monomer density profile $\psi(z)$ is a continuous, monotonically decreasing, approximately parabolic function of z. For larger values of χ, $\mu(\psi)$ can become a non-monotonic function (i.e. more than one value of ψ can be associated with a given value of μ), which implies that the density $\psi(z)$ develops a discontinuity, resulting in a stratification of the layer into a band of high density near the grafting surface covered by a band of low density above it. The location of the density discontinuity is determined from the condition that the osmotic pressure $\Pi = -f(\psi, \phi) + \psi \partial_\psi f(\psi, \phi) + \phi \partial_\phi f(\psi, \phi)$ is continuous, which is required to maintain mechanical equilibrium throughout the layer. This condition is equivalent to using the Maxwell equal areas construction on $\mu(\psi)$ [48, 49, 55, 135]. Once the monomer density profile $\psi(z)$ is determined, the density profile of the nanoparticles $\phi(z)$ is calculated from $\psi(z)$ using Eq.(3.3). These results could also be obtained using an alternative (but equivalent) representation of the SCF method [47, 135].

3.3   SIMULATION METHODS

Simulations of the grafted polymer-nanoparticle system were performed using overdamped Langevin Dynamics simulations [136]. In this type of simulation, particles move under the influence of forces that result from the pairwise interactions between the particles and a random force that represents the thermal noise. Polymers were modeled using a bead-spring model, in which the bonds connecting nearest-neighbor monomers on the same polymer chain were represented using the finitely extensible nonlinear elastic (FENE) spring force [78]

$$F_{FENE} = \frac{-kr}{1 - \left(\frac{r}{\ell_{max}}\right)^2} \tag{3.8}$$

where k is the spring constant, r is the distance between adjacent monomers, and ℓ_{max} is the maximum possible distance between connected monomers.

The inter-particle interactions are modeled by a shifted potential of the Lennard-Jones form:

$$U(r) = \begin{cases} \epsilon \left(\left(\frac{d_{ave}}{r}\right)^{12} - 2 \left(\frac{d_{ave}}{r}\right)^6 \right) + \epsilon - \epsilon_b & r < d_{ave} \\ \epsilon_b \left(\left(\frac{b}{r-r_0}\right)^{12} - 2 \left(\frac{b}{r-r_0}\right)^6 \right) & r > d_{ave} \end{cases} \tag{3.9}$$

in which b is the monomer diameter, d_{ave} is the average diameter of the two interacting particles (or equivalently, the sum of their radii), ϵ is the strength of the repulsive interaction, ϵ_b is the binding strength
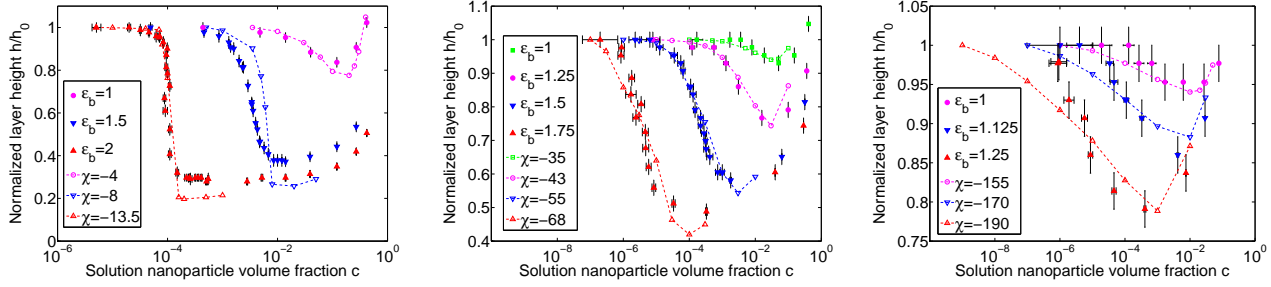
Figure 15: The height of the polymer layer above the grafting surface vs. the volume fraction of nanoparticles in solution for different binding strengths and nanoparticle volumes. Simulation data is shown in filled symbols. The SCFT results are shown as unfilled symbols connected with dashed lines. *Left panel:* nanoparticle volume $\bar{v} = 1$ and grafting distance $a = 4$, *Middle panel:* $\bar{v} = 19$ and $a = 4$, and *Right panel:* $\bar{v} = 96$ and $a = 4$.

between particles, r is the distance between particles, and $r_0 = (d - b)/2$ (where d is the nanoparticle diameter) is a shift in the potential to account for the difference between the radii of the two particles. The binding strength $\epsilon_b = 0$ for monomer-monomer and nanoparticle-nanoparticle interactions, while $\epsilon_b > 0$ for monomer-nanoparticle interactions. This form of the potential ensures that monomers are attracted to nanoparticles only when the distance between their surfaces is $(r - d_{ave}) \lesssim b$.

Sixteen polymer chains, each composed of $N = 100$ linked monomer beads, were grafted onto a flat surface (at $z = 0$) on a square lattice via fixed end beads with the distance between neighboring grafting sites being $a = \sigma^{-1/2}$. The grafting surface was modeled by a repulsive potential of the form of Eq. (3.9), but with $r = z$ and $\epsilon_b = 0$. The simulation box was bounded from above by a similar barrier. Laterally, periodic boundary conditions were enforced. Nanoparticles were allowed to diffuse throughout the simulation box, partitioning between the polymer layer and solution freely. Hence, the total number of nanoparticles in the simulation box was fixed, but their number in the polymer layer was not. For a few cases in which nanoparticles and monomers were the same size, the ceiling was made an absorbing boundary with a constant flux of nanoparticles into the box such that the solution nanoparticle concentration was fixed to within fluctuations. This procedure (corresponding to a grand canonical ensemble) was found to produce the same results as using a closed simulation box (canonical

ensemble) [82]. To test for potential finite size effects, such as a chain interacting with its own periodic image, we measured the lateral radii of gyration of the grafted chains, R_{gxy}:

$$R_{gxy}^2 = \frac{1}{N} \sum_{i=1}^{N} \left((x_i - x_{cm})^2 + (y_i - y_{cm})^2 \right) \tag{3.10}$$

where i indexes the monomer and x_{cm} and y_{cm} represent the x and y coordinates of the polymer chain's center of mass, respectively. R_{gxy}^2 was averaged over the chains and over time for two representative parameter sets: $a = 4$, $\epsilon_b = 1.25$, $\bar{v} = 96$, and $a = 2.2$, $\epsilon_b = 1$, $\bar{v} = 125$ at several nanoparticle concentrations. We found that on average $R_{gxy} = 4.8$ and 3.7, respectively, significantly smaller than the simulation box width in both cases (16 and 8.8 respectively), suggesting that finite size system artifacts are small.

The height of the layer h was determined as the distance from the grafting surface beyond which only a negligible fraction (1%) of the monomers were located after time averaging. Specifically, the distribution of monomers or nanoparticles along the z direction was calculated by creating histograms of the location of the monomer or nanoparticle centers and time averaging. For a time-averaged monomer distribution function $P(z)$ (whose integral was normalized to unity), h was defined as $\int_0^h P(z)\,dz = 0.99$. Once h was determined in this manner, nanoparticles whose centers were located at distance $z < h$ from the grafting surface were regarded as being in the polymer layer, while those with $z > h$ were regarded as being in the solution. Time averages and uncertainties in the solution phase volume fraction of nanoparticles c were obtained via the block averaging method [137]. To improve statistics, in some cases additional averaging over several independent runs was performed; each time series was block averaged separately, and the results were combined using standard uncertainty-weighting methods.

3.4   RESULTS AND DISCUSSION

The results of the theoretical model and of the simulations are summarized in Figs. 15-20. Fig. 15 shows the dependence of the equilibrium polymer layer height h on the volume fraction of nanoparticles in the solution c, as obtained from the theoretical model and the simulations for three different nanoparticle volumes: $\bar{v} = 1, 19, 96$. Note that $\bar{v}$ is a dimensionless ratio of the nanoparticle volume to the monomer volume $\bar{v} = v/v_0$ where v_0 is the volume of a single monomer. In simulations, $v_0 = \pi b^3/6$ with b

obtained from the minimum of the potential in Eq. (3.9), while in the SCFT v_0 was taken to be the volume of one lattice site. In all three cases, a range of monomer-nanoparticle binding strengths are considered: sufficiently strong attraction between monomers and nanoparticles causes a compression of the brush. That is, h decreases from its value in the absence of nanoparticles h_0. At high nanoparticle concentrations, the height recovers back to - and in some cases beyond - h_0. The compression of the brush occurs because the number of attractive contacts between monomers and nanoparticles is increased via an increase in monomer density (i.e. decrease in layer volume). The re-expansion occurs when the layer becomes saturated with nanoparticles, and more contacts can only be added by increasing the volume of the layer to accommodate additional nanoparticles. For $v = v_0$, the compression transition is very sharp and occurs over a narrow range of densities c. In fact, a simpler theory using an Alexander-de Gennes type free energy analogous to Eq. (3.2) with $\bar{v} = 1$ predicts a first order discontinuity in the h vs. c curves [82]. In contrast, the SCFT presented here predicts a rapid but continuous decrease. When the nanoparticle size v becomes significantly larger than the monomer volume v_0 ($\bar{v} \gg 1$), the transition region becomes broader.

The nature of the transition region can be further analyzed by the examination of the monomer and nanoparticle density profiles within the layer, shown in Fig. 16. Both the SCFT and the simulations show three distinct regimes as the nanoparticle concentration is increased. When the concentration of nanoparticles in the solution c is very low, the nanoparticles, although they do infiltrate the layer, cause only a small perturbation to the parabolic density profile that characterizes the free polymer brush. For very high c, in the compressed state, the density profiles of both monomers and the nanoparticles are close to a step function because monomers and nanoparticles are densely packed into a condensed layer. In the transition region between these two limiting cases, the layer develops an inhomogeneous morphology, stratifying into bands of high and low density. According to the SCFT, the formation of the dense state typically starts with a formation of a vanishingly thin band of high density near the grafting surface. Beyond this band is a lower density, parabolic region which extends to higher z. As the concentration of the nanoparticles increases, the width of this dense region grows until it contains all the material in the layer, and the parabolic region vanishes. The simulations qualitatively confirm this picture. They show the formation and eventual expansion of a high density region near the wall, although in comparison to SCFT, the simulations show a depletion region near the wall, a small "foot" in the density profile at high z, and the rounding of the boundaries between the dense and dilute regions. In addition, although
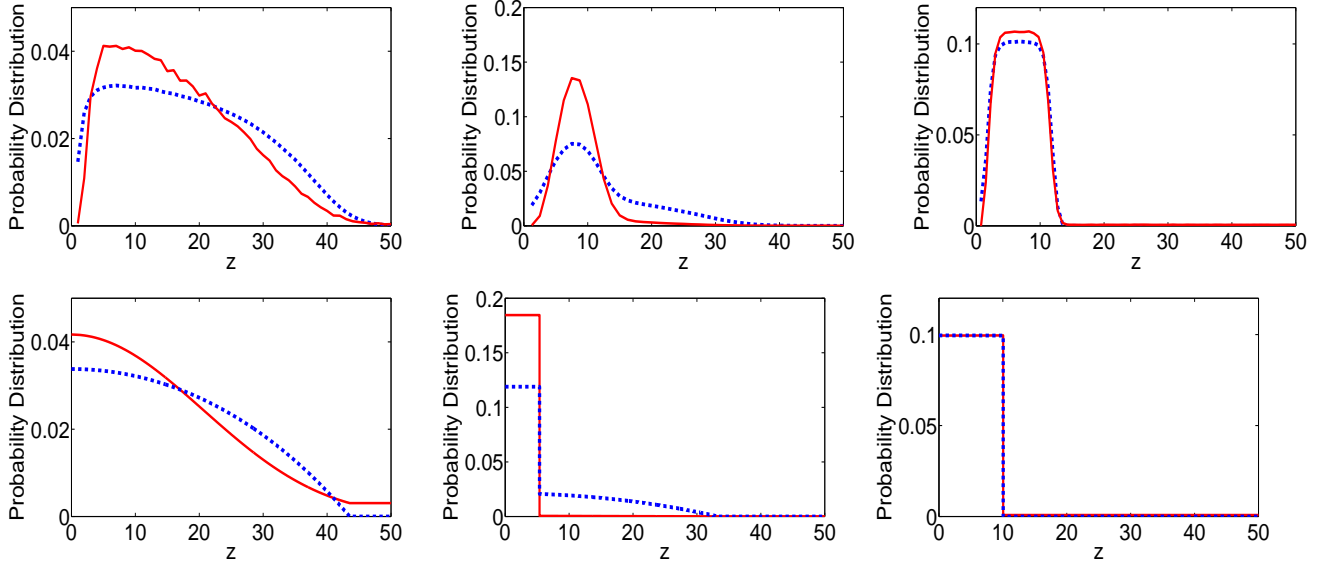
Figure 16: Monomer (dashed blue lines) and nanoparticle (solid red lines) probability distribution functions for grafting distance $a = 4$ and nanoaparticle volume $\bar{v} = 1$ at three different nanoparticle solution volume fractions c. Distributions are normalized such that the integral from zero to the layer height h is equal to one. Note that with this normalization the qualitative shape of the nanoparticle density profiles is accurately represented, but certain quantitative differences between SCFT and simulations, such as the total number of nanoparticles in the layer, are suppressed (see text). *Top row:* Simulations with binding strength $\epsilon_b = 2$. *Bottom row:* SCFT calculations with the corresponding interaction parameter $\chi = -13.5$. *Left Column:* $c = 2 \times 10^{-5}$, *Middle Column:* $c = 1 \times 10^{-4}$, *Right Column:* $c = 2.8 \times 10^{-3}$. See text for details.

the qualitative shapes of the nanoparticle distributions in SCFT vs. the Langevin simulations agree well in Fig. 16, certain quantitative features such as the absolute concentration of nanoparticles in the layer do not necessarily agree well at low c and high binding strength, where concentration fluctuations are too large and Eq. (3.2) is inadequate. These are well-known differences between Milner-Witten-Cates (Semenov-Zhulina) SCFT approximation and more realistic results, stemming from finite size effects, the discrete nature of the particles, fluctuations, and other factors not taken into account in the SCFT. [41, 101, 116, 132]
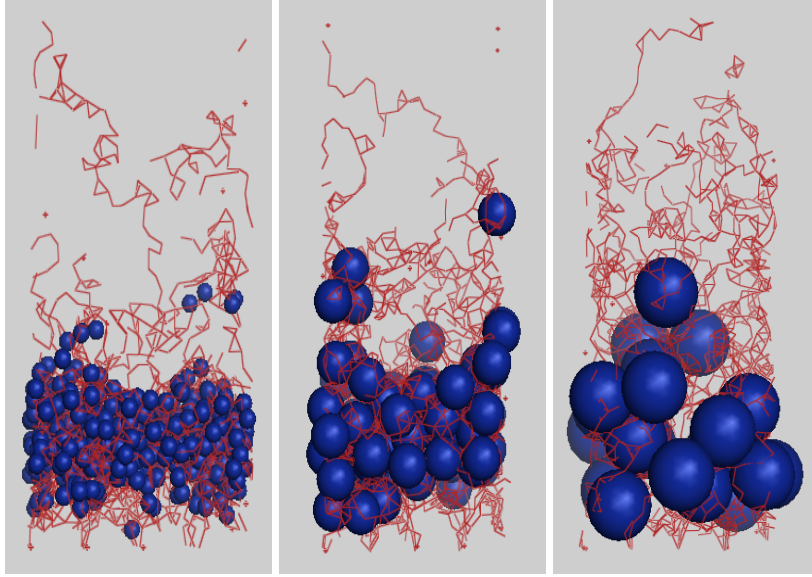
Figure 17: Snapshots from simulation data for $a = 4$ showing the tendency of nanoparticles to cluster near the grafting surface. Polymer chains are shown as red lines, and nanoparticles as blue spheres. *Left:* $\bar{v} = 1$, $\epsilon_b = 2$, $c = 8.1 \times 10^{-5}$, $h/h_0 = 0.76$, *Middle:* $\bar{v} = 19$, $\epsilon_b = 1.75$, $c = 1.3 \times 10^{-6}$, $h/h_0 = 0.83$, *Right:* $\bar{v} = 96$, $\epsilon_b = 1.25$, $c = 1.0 \times 10^{-6}$, $h/h_0 = 0.94$.

The features of the layer in the transition region are further illustrated by the representative simulation snapshots in Fig. 17. One can see that a dense region of monomers and nanoparticles forms near the grafting surface, corresponding to the peak in the density profile in the middle column of Fig. 16. Some of the polymer chains extend out of the dense region into the solution, forming a low density region above, corresponding to the tail region in the middle column of Fig. 16. It should be emphasized that, both in the SCFT and the Langevin simulation results, the layer is not merely adsorbing additional particles as the concentration in solution increases, but the observed layered structure inside the brush is induced by collective aggregation of the nanoparticles into the layer.

The SCFT predictions of the h vs. c behavior for grafting distance $a = 4$ are in good agreement with the simulations for both $\bar{v} = 1$ and $\bar{v} = 19$. For $\bar{v} = 96$, some features of the theoretical curves, such as the width of the transition region, begin to deviate from the simulated ones. Since volumes of $\bar{v} = 1, 19, 96$ correspond to nanoparticle diameters of $d = 1, 2.67, 4.57$ in units of monomer diameter
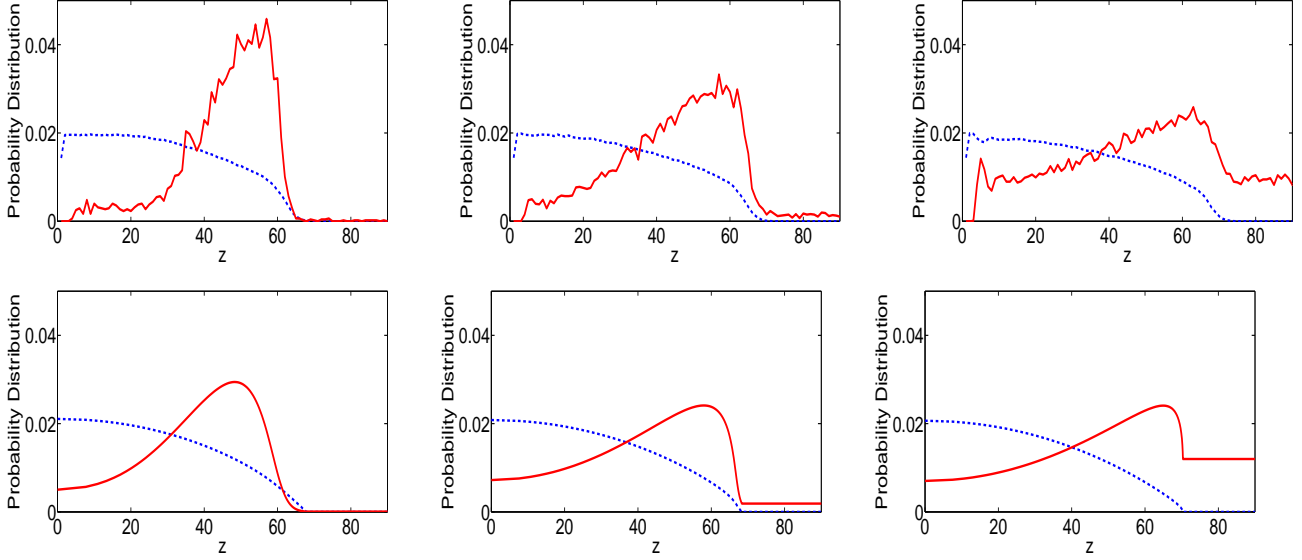
Figure 18: Monomer (dashed blue lines) and nanoparticle (solid red lines) probability distribution functions for $a = 2.2$ and $\bar{v} = 125$. Distributions are normalized such that the integral from zero to the layer height h is equal to one. *Top Row:* Simulations with binding strength $\epsilon_b = 1$ at three different numbers of nanoparticles in the simulation box (8, 16, 32; cf. Fig. 20). *Bottom Row:* SCFT calculations with interaction parameter $\chi = -175$ and three corresponding solution nanoparticle volume fractions ($c = 10^{-4}, 10^{-2}, 10^{-1}$). See text for details.

respectively, this is not unexpected. As previously mentioned, qualitative changes in the system behavior are expected to arise when the particle diameter d is on the order of the blob size size of the brush ξ [73, 102, 118]. For larger particles, additional perturbations of the polymer configurations that are not taken into account in the SCFT (such as the lateral stretching of the chains, or meandering of the chains around the particles) become important. In a brush, the blob size can be estimated to be on the order of the grafting distance ($\xi \sim a = 4$) [37], or alternatively $\xi \sim \psi^{-3/4} \sim (N/a^2 h_0)^{-3/4} \simeq 4.61$ [44, 131]. Thus, for $\bar{v} = 96$, the nanoparticle diameter $d \simeq \xi$ and one would expect the mean field approach used here to start to break down. Nevertheless, the SCFT appears to agree qualitatively with the simulation results even when $d > \xi$, as seen in Fig. 18 (discussed below), despite some deviation in the quantitative characteristics.
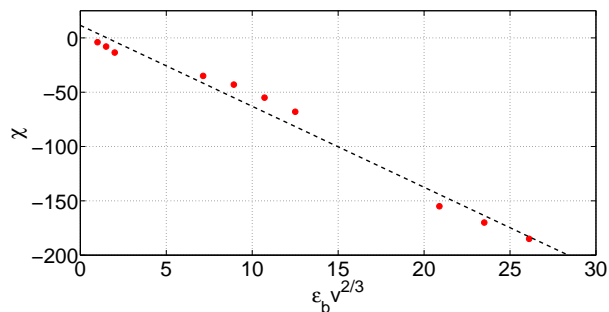
Figure 19: Correspondence of the mean field interaction parameter χ (defined in Eq. (3.2)) to the interaction energy used in simulations ϵ_b (Eq. (3.9)). *Dots:* values used in Fig. 15. *Dashed line:* Fit to a simple heuristic approximation $|\chi| \sim \bar{v}^{2/3}\epsilon_b$.

The only fitting parameter in the comparison of simulation results with SCFT is the relationship between the mean field interaction parameter χ and the interaction strength in the simulations ϵ_b. The fitted values agree rather well with a scaling relationship between the two that can be estimated *ab initio* on basic physical grounds. In mean field theory, the average total energy of attractive interactions experienced by a nanoparticle is $\chi\psi$. In simulations this energy is proportional to the average number of its surface contacts with the monomers, so that $|\chi| \sim v^{2/3}\epsilon_b$. One can see from Fig. 19 that this relationship is roughly obeyed. Some deviations from this simple argument are to be expected since, in principle, χ and ϵ_b should be related via the second virial coefficient of the system [138].

The behavior of the system changes entirely for very large particles or high grafting densities ($d \gg \xi \sim a$, where ξ is the "blob" size of the brush). In this regime, the free energy penalty associated with inserting a nanoparticle into the brush is larger and overcoming this penalty requires stronger binding energies [73, 75, 102, 105, 118]. If the binding energy is not sufficiently high to compensate, the behavior in this regime is illustrated in Figs. 18 and 20 for grafting distance $a = 2.2$ and particle size $\bar{v} = 125$ ($d = 5$). Nanoparticles still penetrate the topmost, dilute region of the brush, but the brush height does not change much as a result, and the polymer conformations and their density profiles are essentially unperturbed. As more nanoparticles are added to the system, they progressively infiltrate the layer. However, in this case the infiltration starts with the accumulation of the nanoparticles in the outer part of the polymer layer where the monomer density is lower, and not near the grafting surface. Interestingly, the agreement
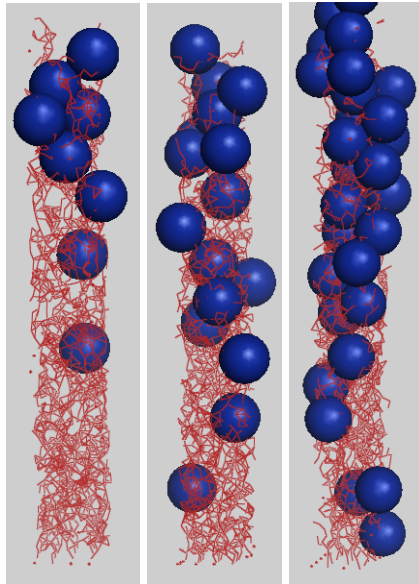
Figure 20: Snapshots from Langevin simulations with $\bar{v} = 125$, $a = 2.2$, and $\epsilon_b = 1$ corresponding to the profiles in Fig. 18. Polymer chains are shown as red lines, nanoparticles as blue spheres.

between the SCFT and the simulations is good even when the particle size is significantly larger than the grafting distance (Figs. 18 and 20) because the nanoparticles perturb the polymer conformations only slightly in this regime compared to a brush without the nanoparticles.

3.5 CONCLUSIONS

Using a theoretical SCFT model and Langevin dynamics simulations, we have shown that addition of nanoparticles to grafted polymer layers can result in a wide variety of qualitatively different behaviors that can be controlled by the polymer-nanoparticle binding strength, the nanoparticle volume, the nanoparticle concentration in the solution, and polymer grafting density. Sufficiently strong binding allows nanoparticles to penetrate the polymer brush. If the particle size is smaller than the "blob" size of the brush, both SCFT and Langevin simulations predict large-scale morphological changes in the layer, characterized by a decrease in the height of the layer (Fig. 15), and the formation of a dense region rich

in both monomers and nanoparticles that occurs near the grafting surface (Figs. 16 and 17). Remarkably, even when the grafting density was quite high (such that our polymer brush may be entering the over-stretched regime [119]) and the nanoparticles were quite large (such that the mean field approximations of the Theory section may be breaking down), both SCFT and Langevin simulations were in agreement in predicting a penetration of nanoparticles only into the sparse region near the top of the brush (Figs. 18 and 20), related to the "partial penetration" regime noted by Kim and O'Shaughnessy for the case of non-attractive nanoparticles [73].

The predicted behavior of polymer layers in the presence of nanoparticles has a clear physical explanation. It does not arise because the polymers are exposed to a bad solvent or due to an interaction between the solvent and the nanoparticles[49, 50, 52–55], but rather due to an attraction between the nanoparticles and polymers. Qualitatively speaking, it arises from the competition between the energy of attraction of the nanoparticles to the polymer, which favors compact conformation, and the confinement entropy of the polymers, which favors extended conformations. In fact, our previous work, based on a simpler Alexander-de Gennes-type (AdG) theory that assumes that the density of both monomers and the nanoparticles is uniform within the brush, takes into account only these two effects and also predicts a collapse of the polymer layer upon addition of small attractive nanoparticles [82]. However, the AdG type theory is unable to describe the non-uniform distribution of the particles in the brush and predicts a discontinuous collapse of the layer height, which, although approximately correct for small nanoparticles, starts to break down for larger particles. Remarkably, the SCFT treatment presented here, verified by the simulations, is applicable to a wide range of nanoparticle volumes and interaction strengths and also accurately describes the distribution of the particles within the layer and its internal morphology, thus greatly improving the applicability of the theory to a wide range of systems in both biological and technological contexts.

In particular, the results reported here may shed light on recent experimental results on the conformational changes induced in the unfolded polypeptides encountered in the Nuclear Pore Complex by binding of transport proteins, which may impact the transport of molecular cargo across the pore. Recent experiments with surface layers of such unfolded proteins observed regimes similar to those predicted here, such as the reversible collapse of the layers [31, 34, 121]. Detailed comparison as well as the examination of dynamic behavior will be reported elsewhere. Interactions of proteins and nanoparticles with surface polymer layers also arise in several technological applications, such as the fabrication of a

variety of non-fouling surfaces, responsive materials and nano-electronic devices, often involving large conformational changes in the polymers (reviewed in [64]). However, the predictive understanding of such systems is only starting to emerge.

Our model provides the basic physical framework for understanding and interpreting such experiments and designing or engineering devices. It can also be systematically developed by introducing more system-specific details into the model and presents specific, experimentally verifiable results on how the layer height and morphology depend on the densities and interaction strengths of the grafted polymers and nanoparticles involved.

4.0 APPLICATIONS TO THE NUCLEAR PORE COMPLEX

4.1 BACKGROUND AND INTRODUCTION.

The nuclear pore complex is responsible for conducting all molecular transport between the nucleus and the cytoplasm in eukaryotic cells. Transport through the NPC is fast, highly selective and robust with respect to molecular noise and structural perturbations. The transport of small cargo (such as ions) of sizes up to several nanometers [5] is not regulated by the NPC and occurs by pure diffusion, without direct interactions with the NPC. However, the passage of larger macromolecules, such as import of transcription factors and export of mRNA, is tightly regulated by the NPC. For efficient transport, macromolecules larger than several nanometers must bind a transport factor from a highly conserved family of proteins (known as Karyopherins or "kaps" in yeast or Importins/Transportins in vertebrates) that shuttle the bound cargo through the NPC [2].

The passageway for transport complexes is formed by a structural scaffold that consists of multiple proteins of a combined size of ∼125 MDaltons [139]. The central channel they form has a diameter of about ∼35-50 nm [4] and is filled by a set of 150 -250 (depending on the species) natively unfolded, unstructured polypeptide chains, collectively known as "FG nups" due to large numbers of phenylalanine-glycine (FG) repeats in their sequence [6, 7]. The FG nups appear to set up the permeability barrier that prevents the free passage of large macromolecules. They also serve as a template for the transient binding of the cargo-carrying transport factors. The attractive interaction and transient binding of the transport factors to the FG nups appears to be the key component of the transport mechanism, responsible for the selectivity and speed. For example, interfering with the binding of the transport factors decreases the transport efficiency, or abolishes the transport altogether [3, 22, 140, 141]. Conversely, functionalizing particles or molecules that normally cannot penetrate the NPC to bind transport factors or interact directly with the FG nups allows them to pass through the NPC [142].

Although the consensus on the overall role of the FG nups in transport through the NPC seems to have been reached, a mechanistic understanding is still lacking. It is clear that the binding of the transport factors helps to overcome the permeability barrier and enhances their transport compared to non-binders, and tuning the strength of this interaction enables control of the transport selectivity [11, 32, 143, 144], but this does not directly reveal the underlying mechanism of transport. Simple models that describe the transport as facilitated diffusion modulated by the interactions with the FG nups provide a good overall picture of the selectivity of the NPC and are able to semi-quantitatively describe the transport properties of systems that mimic the NPC function [143, 144]. However, it is not clear how the coarse grained parameters of such models arise from the molecular properties of the FG nups or how they are related to the permeability barrier.

Although structural data and measurements of the affinities are available, the results between different studies are conflicting in regard to identifying the major factors contributing to the binding of the transport factors to the FG nups. Generally, the strength of the interaction is reported according to the dissociation constant for the binding of the transport factors to the nups K_D. If one considers the process of binding as a simple bimolecular process in which transport factors at an equilibrium solution concentration $[Kap_s]$ and FG repeat domains at an equilibrium concentration $[FG]$ react to form bound complexes at an equilibrium concentration $[Kap_b]$, K_D may be thought of as the ratio $[Kap_s][FG]/[Kap_b]$ or equivalently as the equilibrium solution kap concentration at which half of the FG binding sites will be occupied [145]. In one experiment, the binding of the transport factor Kap95p to the nup Nsp1p was fit to a two-component Langmuir isotherm having a binding affinities of $0.32\mu M$ and $5.3\mu M$ [35]. In another experiment, a two-component fit was also used to obtain binding affinities between Kapβ1 and cNup62 of $0.35\mu M$ and $95.9\mu M$ [31]. Other studies have obtained values such as $8nM$ for free Kap95p and Nup62 [146], $1.7\mu M$ for Kap95p-Kap60p-cargo complexes with Nup42p, $90nM$ for the same complex with Nup100p, and $0.4nM$ for the complex with Nup1p [147]. In addition to the wide variation of these measurements, the average measured affinity of $\sim 0.3\mu M$ is substantially lower than physiological concentrations, and predictions based on transport times yield substantially weaker binding (e.g. $K_D \geq 4\mu M$ for transportin in permeabalized HeLa cells) [3, 148].

The actual conformations of the FG nups in the NPC and the mechanism by which the transport factors navigate the network created by the FG nups remain unclear. It is still under debate whether the FG nups essentially serve as a template for binding of the transport factors, or whether their dynamic con-

formational changes in response to transport factor binding are a crucial part of the transport mechanism. Various scenarios and models of the FG nup conformations have been proposed, with correspondingly different models of the dynamics of the translocation tied to the underlying conformation of the FG nups. Many of these ideas are supported or inspired by *in vitro* experiments in different regimes and with different FG nups. In one scenario, the FG nups form a physical gel due to their cross-linking at the hydrophobic FG locations, and the TFs disentangle this gel by exchanging their binding contacts with the FG nups. Conversely, macromolecules which do not have the requisite binding sites are unable to disentangle the gel and are blocked from entering the pore [27–29]. In another picture, the FG nups form a non-cross-linked "polymer brush" that constitutes the permeability barrier. In this case, it is the steric repulsion from the fluctuating chains which blocks passage through the pore. Transport would be achieved when the brush is collapsed by TFs, thereby removing the barrier [10, 30, 31]. More complicated models taking into account heterogeneity and molecular structure of the FG nups, have been proposed, such as the forest model in which nups are proposed to have collapsed globular domains near the channel walls and additional globular domains near the channel center, leaving two transport pathways in the remaining space [23, 24]. At present it is difficult to distinguish the mechanisms from one another in terms of experimental results, and some details remain obscure. For instance, it is not known with how many FG nups a transport factor interacts during the passage or for how long. In yet another model the transport factor is transported through the NPC by a single long-lived initial binding to an FG nup which carries it through the NPC [25]. Although the translocation of the TFs through the NPC can be tracked on single molecule level [149], the current experimental resolution (milliseconds and up to 10 nm) is not sufficient to resolve the detailed conformations of the FG nups and the coordinated dynamics of the transport factors and the FG nups during transport. Therefore, the support for different models comes from inferring the *in vivo* mechanisms from indirect or *in vitro* experimental efforts.

However, even the *in vitro* experiments appear to produce conflicting results. Specifically, several groups investigated assemblies of FG nups, grafted onto rigid surfaces [10, 30, 31, 35]. The height of the resulting layers has been investigated by atomic force microscopy (AFM), ellipsometry, surface plasmon resonance (SPR), and quartz crystal microbalance (QCMB) under different conditions. In particular, it was established through AFM measurement that the FG nups behave like conventional polymeric worm-like chains and that the elastic properties of such layers are close to what is expected for layers of flexible polymers [10]. However, the polymer height was dramatically reduced upon the addition of the transport

factor Kapβ1 [30]. This appears to support the idea that the nups are in a brush-like conformation which is collapsed by the transport factors. In a later experiment, the same group used SPR to again observe a collapse and subsequent recovery of the putative nup brush [31]. However, a similar experiment by another group used QCMB and concluded that their nup brush did not collapse in the presence of the TFs even though they penetrated the FG nup layer [35].

The FG nups are complex and their interactions are not fully understood. Therefore, in principle, many factors might need to be considered in order to explain the various observations, which can depend on all sorts of minute details of the FG nup sequence and local molecular interactions. However, despite wide variation of the FG nup sequences among different species, some major characteristics, such as FG mediated interaction with the transport factors, are strongly conserved. Similarly, artificial nanochannel mimics of the NPC that maintain only a gross level of similarity to real NPCs on the level of conceptual design recapitulate many important functional features of the NPC's under quite different conditions and with just a limited number of the FG nups [68–70]. Thus, it is not unreasonable to expect that the conformational dynamics of the FG nups and the transport factors can be understood from basic physical principles without consideration of the specific molecular details of individual cases.

Because the conformations of the FG nups and their dynamics are difficult to access experimentally, computational and theoretical approaches have become increasingly important (e.g. [129, 144, 150, 151]). Although these studies have provided insight into some of the factors that may be critical in determining the behavior of the NPC constituents, a unified theory which parameterizes the essential features of the system so as to explain the wide variety of observed behaviors has been elusive.

In this chapter, I address the conflicting experimental evidence by investigating the basic physical features and variables that control the kap-dependent conformations of the FG nups and their morphological changes. Using a coarse grained statistical mechanical theory [82, 83] that encompasses only the basic consensus physical features, i.e., the flexible nature of the FG nups and their attractive interactions with transport factors, we analyze the behavior of a nup brush grafted to a flat surface in a variety of parameter regimes. Based on this limited set of assumptions, the model resolves the apparent contradictions by obtaining qualitatively different behavior at different grafting densities and different kap-nup binding strengths. It provides experimentally testable predictions regarding what parameters control the transitions of the system from one regime to another and how apparently conflicting experimental results can be reconciled.

4.2 THE MODEL

The FG nups and their interactions with the transport factors can be modeled on many different levels of detail. However, not all of those details are known: even the number of binding sites on the transport factors and binding affinities are a matter of controversy. Therefore, the model used in this chapter aims as a first stage to capture only the essential physical properties of the FG nups and their interactions with the TFs. This basic model can then be further developed with additional molecular and structural details by adding additional terms to the free energies below or modifying the existing ones to account for effects such as the discrete binding sites on the transport factors, the specific amino acid sequence of the nups, or electrostatic effects. As a first attempt, the FG nups are modeled as flexible polymeric chains. Although natively unfolded proteins cannot always be described in this way (for instance due to residual secondary structure), the FG nups have been shown to be well described by the wormlike chain model, at least in *in vitro* AFM measurements [10]. The TFs are modeled as large solid spherical particles that interact *attractively* with the FG nup polymers.

We first examine the behavior of a flat layer of grafted chains in equilibrium with a solution of the particles - mimicking the experimental setup of Refs. [10, 30, 31, 35]. The main physical factors acting in such a situation are the entropy of chain packing and stretching and the energy of the attractive interaction. Roughly speaking, the attractive interaction between nups and transport factors favors more compact structures because it allows formation of more energetically favorable contacts, while the entropy of packing favors more diffuse and open conformations. The model is investigated using two different statistical mechanical models. For estimating crude properties of the layer, such as the maximum compression that can be achieved as the concentration of the transport factors is varied, a model of the Alexander-de Gennes form will be used. When details are needed, such as the layer morphology, a quasi-analytical self-consistent field theory (SCFT) is used. The details of the two approaches have been reported in [82] and [83] respectively and have been discussed in Chapters 2 and 3. The results of the models have previously been compared to the results of Langevin dynamics computer simulations in order to verify that they capture the essential physical features relevant to the behavior that they will be used to describe. In addition, the differences between the theory and simulations have already been examined, allowing us to understand qualitatively the corrections that are typically required to make the theoretical results more accurate.

In both models, the nup chains can be thought of as consisting of linked monomers, where each monomer can be roughly thought of as corresponding to a patch of several amino-acids−an appropriate mesoscopic size which is large enough that the specific atomic interactions can be coarse grained but small enough that the FG nups can still be regarded as long chains of monomers. The current modeling does not aim for a detailed representation of the specific chemical details of the FG nups, but rather elucidation of general patterns of behavior that are actually independent of various details (which can be added later).

We first obtain the non-elastic local free energy density $f(\psi, \phi)$ in units of kT from a lattice gas model, generalizing previous works (e.g. [37, 39, 44, 82]). The derivation of this expression is discussed in Appendix A. We obtain

$$f(\psi, \phi) = (1/\bar{v})\{\phi \ln \phi + (1 - \bar{v})(1 - \phi) \ln[1 - \phi]$$
$$+\bar{v}(1 - \psi - \phi) \ln[1 - \psi - \phi] + \chi \phi \psi\} \tag{4.1}$$

where ψ and ϕ represent the volume fractions of the monomers and transport factors respectively, the reduced volume $\bar{v}$ is the ratio of the nanoparticle volume to the monomer volume, and χ characterizes the binding between the FG repeats and transport factors and depends on both the binding strength of individual bonds and the maximum number of bonds which can be supported. We consider the case $\chi < 0$, which corresponds to attractive kap-nup interactions. In the Alexander-de Gennes model, one takes the volume fractions ψ and ϕ to be equal to their mean values in the polymer layer. As such, the non-elastic free energy of the polymer layer can be obtained by simply multiplying Eq. (4.1) by the layer volume. In the SCFT model, ψ and ϕ are local variables that represent the mean volume fraction of monomers or nanoparticles in the vicinity of a particular location in the layer, and a volume integral must be performed in order to account for contributions from the entire layer.

To the non-elastic free energy obtained from Eq. (4.1) we add a term for the free energy associated with stretching the polymer chains. In the Alexander-de Gennes model, we use $h^2/2N$ per chain, where h is the height of the polymer layer above the surface and N is the polymerization of the chain [37, 41]. In the SCFT model, one integrates the stretching energy of the polymer over the polymer backbone. This is achieved via an integral of the form $\int_0^N ds \left(\frac{\partial}{\partial s}\vec{r}(s)\right)^2$ where $0 \leq s \leq N$ represents the location as indexed along the polymer chain and $\vec{r}$ is the same point's spatial location.

Finally, we must couple the polymer layer to reservoir of transport factors at a fixed concentration c. The solution acts as a source of transport factors which may partition into the polymer layer. The partitioning of the particles is governed by their chemical potential μ_c. Using a lattice gas argument analogous to those outlined in Appendix A and taking the appropriate thermodynamic derivative, we obtain a solution chemical potential $\mu_c = \ln(c/(1-c))$. In the Alexander-de Gennes model, the solution is also treated as a reservoir of volume with osmotic pressure $\Pi = -\ln(1-c)/\bar{v}$. In the SCFT model, the height of the layer is free to vary via the spatially varying monomer volume fraction ψ, which is only nonzero up to the edge of the polymer layer, and the continuity of the osmotic pressure enters elsewhere, as discussed in Appendix B.

The resulting grand canonical thermodynamic potential in units of kT and per chain for the Alexander-de Gennes model is then

$$\Phi = \frac{h^2}{2N} + a^2 h \left(f(\psi, \phi) - \frac{\mu_c}{\bar{v}} \phi + \Pi \right) \tag{4.2}$$

where a is the grafting distance between the chains. We minimize this potential over the brush height h and the number of transport factors bound in the layer and obtain the equilibrium state of the system using a procedure very similar to the one described in Chapter 2 and in [82].

For the SCFT model, these physical considerations are encapsulated in the free energy functional

$$
\begin{aligned}
F[\{\vec{r}_\alpha(s)\}] &= \sum_\alpha \frac{1}{2b^2} \int_0^N ds \left(\frac{\partial}{\partial s} \vec{r}_\alpha(s) \right)^2 \\
&\quad + \frac{1}{b^3} \int d^3 r (f(\psi(\vec{r}), \phi(\vec{r})) - \frac{1}{\bar{v}} \mu_c \phi(\vec{r}))
\end{aligned}
\tag{4.3}
$$

where α indexes the polymer chain. Note that energies are expressed in units of kT, lengths are expressed in units of the monomer size in both models. b represents the diameter of one monomer and will set the scale of length when comparing this theory to experimental results. The functional can be minimized via a self-consistent approach within the framework of Milner-Witten-Cates theory [46] or the alternative approach of Zhulina et al. [47]. In particular, at equilibrium, the free energy Eq. (4.3) is minimized over all the polymer trajectories and the density distribution of the transport factors in the layer, as explained in previous work [83] and in Chapter 3 of this thesis.

Although our model does not attempt to capture molecular details about the nups or kaps, we need to understand the approximate parameter range that is relevant to the real systems. The masses of the

free transport factors Kapβ1 and Kap95p are both approximately 100kDa [141, 152]. Since our model does not represent the detailed shape of the kap, we will assume for simplicity that the kap is a spherical globular protein which has a typical density of $1.4 g/cm^3$ [153]. In this case its volume would be approximately $119 nm^3$ and its diameter $6.1 nm$. To give another example, the smaller transport factor NTF2 has a mass of approximately 29kDa [154], which would correspond to approximately a volume of $35 nm^3$ and a diameter of $4.1 nm$. In our model, the scale of length is set by the monomer diameter b. This distance corresponds to the cross-sectional size of the polymer chain in the direction perpendicular to the polymerization. Since the FG nup is a natively unfolded protein and lacks any significant secondary structure [6], we approximate its cross-sectional "width" as being on the order of one amino acid size, and we will set the diameter of the monomers of our polymer chain to be $b = 1 nm$. In our model, the volume of the kap should be expressed in units of the monomer volume. Monomers of diameter $b = 1 nm$ have volume $v_0 = (\pi/6) nm^3$. Therefore the volume of Kapβ1 and NTF2 would be roughly $\bar{v} = 227$ and $\bar{v} = 67$ respectively with all the assumptions above. It should be noted, however, that the model used is not very precise in its use of the kap volume. For instance, one might note that the lattice construction used to obtain the free energy density Eq. (4.1) specifies only the number of lattice sites occupied by the particles. It does not distinguish the shape of the particles, and the spatial arrangement and coordination of lattice sites are to some extent arbitrary. As a result, there is some degree of ambiguity in the correspondence between the actual kap volume and the parameter $\bar{v}$ in the model, and some fitting may be required.

4.3 RESULTS

Layer height has served as a useful and easily measured proxy for the layer conformation in experiment, and we will also use it theoretically. Overall, depending on the kap size, grafting density, and the interaction strength, there are several different regimes that result in different degrees of brush compression. A heuristic understanding of the effect of changing these parameters can be gained from Fig. 21 for the case of $\bar{v} = 227$, which is on the order of the transport factor size. In this plot we show the height of the layer when at maximum compression (for any solution kap concentration c), normalized by the height of the layer in the absence of kaps, for the given grafting distance a, and kap-nup interaction parameter

χ. In other words, each point on the plot shows layer height at the minimum of the h/h_0 vs. c curve (analogous to the ones shown in Figs. 11 and 15) for the given a and χ. For simplicity and since we only show the maximum compression rather than the detailed features of the morphology, we use the Alexander-de Gennes model in this figure. We will then supplement our understanding of the various qualitative regions of the diagram with more detailed results drawn from the Milner-Witten-Cates based model.

Qualitatively, we identify three basic regions of the diagram, which will be analyzed in detail below. At sufficiently weak binding (right side of Fig. 21), the compression is modest and the polymer brush is only slightly perturbed by the presence of the transport factors, regardless of their concentration. If the grafting density is too high (bottom of the diagram), the proximity of the polymers to each other creates a large energetic penalty for penetration of the transport factors into the polymer layer, and thus the compression of the brush is once again modest. If, on the other hand, the grafting density is low and the binding is strong (top left area of the diagram), a significant compression can occur. Strong compression is generally accompanied by layer collapse induced by penetration of the kaps to the region near the grafting surface.

4.3.1 Weak Binding Case: Continuous Penetration

At sufficiently weak binding strengths (compared to the strength of the repulsive interactions between monomers, which increases with the grafting density), the penetration of kaps into the nup brush is gradual and the effect on the layer height is modest. By this we mean that the kap density profile in the nup layer is continuous and is not characterized by strong inhomogeneities, a sudden collapse, or discontinuous loading of the brush. Rather, one can envisage the kaps as simply binding to the nups without significant changes in the nups' conformations as a result. The energetic benefit of a morphological reorganization of the nups to accommodate the kaps is not sufficient to overcome the energetic penalties associated with it. The monomer density profile, which characterizes the distribution of nups in the layer, is likewise continuous and is only slightly perturbed from its shape in the absence of kaps—the standard downward-facing parabola [41, 46, 47, 132]. The extent of the effects depend upon the concentration of kaps present, and there can be some compression of the brush due to a weak binding process of this sort, but typically the fractional reduction in brush height is on the order of 10% or less. This type of
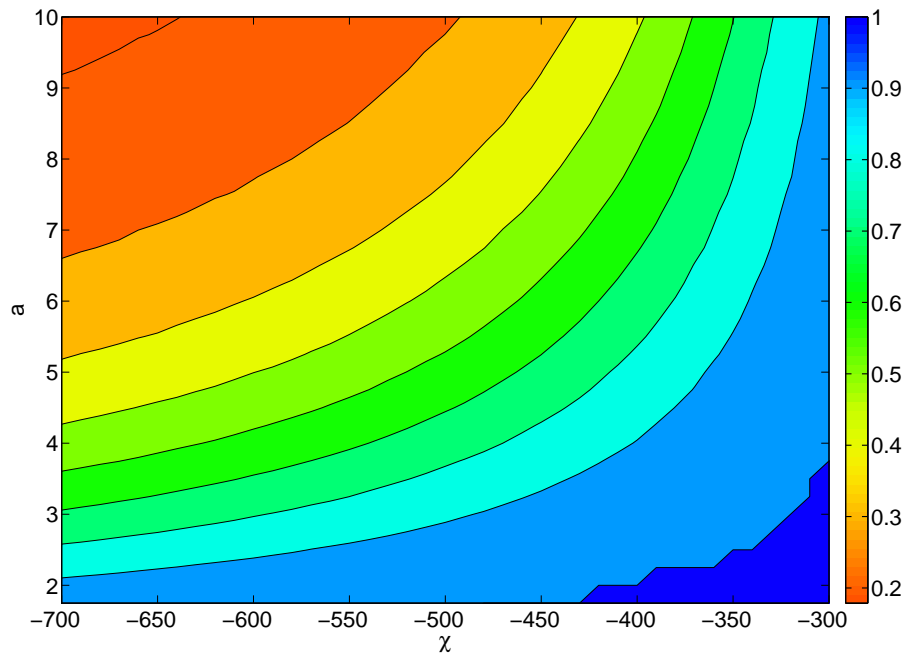
Figure 21: Contour plot which shows the maximum relative compression of the nup brush which can occur for the given kap-nup interaction parameter χ and grafting distance a for kap volume $\bar{v} = 227$. The color bar indicates the smallest value of the nup layer height h, normalized by the height in the absence of the transport factors h_0, which may be obtained for any solution concentration c of transport factors. This figure was obtained using the Alexander-de Gennes formulation of the theory.

compression can be seen on the right-hand side of Fig. 21.

An example of this type of density profile can be seen in Fig. 22. The monomer density profile is nearly parabolic (which is its shape in the absence of transport factors [46]), and the density profile for the transport factors qualitatively tracks the monomer density profile, though the concentration of the transport factors is much lower than the monomer concentration. In this case, one can regard the bound transport factors as being a small perturbation on the ordinary nup polymer brush, and the height of the polymers will not change much due to the binding of only a small concentration of transport factors.

66

Figure 22: Monomer (dashed blue) and Nanoparticle (solid red) density profiles for the case $\bar{v} = 227$, $\chi = -300$, $a = 9$, $N = 100$, and $c = 10^{-3}$. In this case, the monomer density profile is nearly parabolic and the density profile of the transport factors tracks the monomer density qualitatively. The transport factors are bound throughout the nup brush, but the effect of the transport factors on both the shape of the monomer density profile and its height above the grafting surface is limited. A compression of $\sim 10\%$ is possible with these parameters, but the qualitative shape of the monomer density profile is not strongly affected.

4.3.2 Low Grafting Density and High Binding Strength: Collapse and Recovery

For stronger binding and sparser grafting, the compression of the brush is much more dramatic. The strong energetic advantage of a qualitative morphological change in the nups which maximizes the number of contacts between the nups and kaps overwhelms the entropic and excluded volume penalty which ordinarily keep monomers separated. The collapse that results is characterized by the formation of a dense layer of kaps and monomers near the grafting surface (where the density of monomers is highest in the brush). In some cases, this dense layer may consume the entire polymer brush, while in other cases it may abut a sparser region above it where the monomer density is closer to that of the unperturbed brush.

The polymer height is reduced as kaps bind to the polymers and consume the sparse, brush-like region of the polymer layer, replacing it with a more compact, denser layer near the grafting surface.

When enough kaps have been loaded into the polymer layer, the sparse region disappears completely and the entire polymer layer is dense. This is the state of minimum layer height. Once this state has been realized, loading additional kaps into the brush results in a swelling of the brush. This swelling creates free volume in which the new kaps can be loaded. As a result, the brush height as a function of kap concentration is non-monotonic, and increasing the kap concentration will result in recovery of the brush back to, and ultimately beyond, its height in the absence of kaps at sufficiently high solution kap concentrations.

Both the collapse and recovery have been observed in Ref. [31], and the authors hypothesized the existence of a dense layer of kaps near the surface as an explanation of their experimental results. Although they did not observe these morphologies directly, they successfully fit their data with a two binding affinity model. As a way to explain the apparent presence of two different binding affinities, they suggested a strong binding in the dense part of the layer and weak binding in the sparse part of the layer. Our results in this regime appear to qualitatively corroborate the "cartoons" proposed in Ref. [31], in that we see the formation of a layer of kaps near the surface, followed by additional layers on top as more kaps are loaded into the brush.

Examples of this type of profile can be seen in Fig. 23. In such a case, the monomer density profile shows a discontinuity which connects a region of high density to a region of lower density. In the density profile for the transport factors, the effect is even more dramatic. The concentration of kaps in the dense region near the grafting surface is significantly higher than the concentration elsewhere. This corresponds to the formation of one or more layers of transport factors near the grafting surface. At higher solution concentrations (right panel of Fig. 23), the dense layer has grown to the point where the region of lower density has been completely consumed, and the entire nup layer has become dense. This corresponds to multiple layers of kaps piling up. As even more transport factors are added to the brush, it will swell because it is already stuffed with kaps and must grow in order to bind more.

4.3.3 High Grafting Density Case: Imperfect Penetration

If the size of the kaps is sufficiently large compared to the grafting distance of the polymer chains, they gradually become unable to penetrate the space between the polymers. At intermediate grafting densities, the kaps are preferentially located near the top of the brush, where there is a lower density of monomers
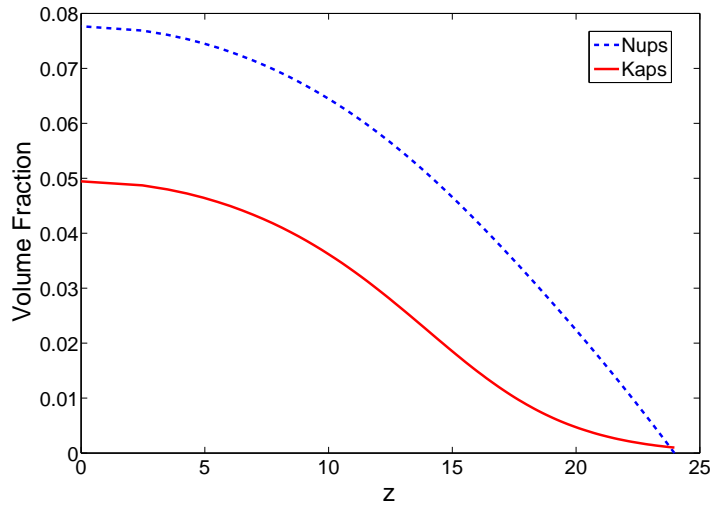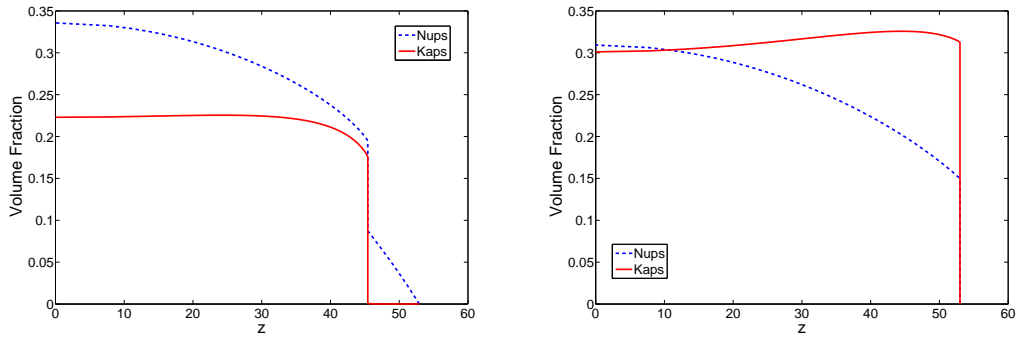
Figure 23: Monomer (dashed blue) and Nanoparticle (solid red) density profiles for the case $\bar{v} = 118$, $\chi = -250$, $a = 2.7$, and $N = 100$. *Left:* $c = 10^{-8}$. Note the discontinuity in the density profiles. This corresponds to the formation of a dense layer of nup monomers and transport factors near the grafting surface with a sparser region of nup monomers above it. *Right:* $c = 10^{-4}$. In this case, the entire layer has become dense, and the sparse region has disappeared.

and thus more free volume. At even higher grafting densities, they eventually are expelled from the brush altogether and must remain on the surface of the brush. These regimes of partial penetration and no penetration have been noted in theoretical studies of polymer brushes exposed to nanoinclusions which do not bind to the polymers [73]. In our case, the failure of kaps to penetrate to the bottom of the brush precludes a collapse of the brush. The collapse results from polymer strands being drawn toward the grafting surface via binding to the transport factors located there. It is possible that a dense region of kaps bound to monomers may form in the case of partial penetration, but if it does, it must be formed near the top of the brush, and this would not result in a reduction in the height of the brush.

An example of this type of effect can be seen in Fig. 24. In this case, the highest concentration of transport factors does not occur near the grafting surface, but rather near the outer edge of the nup brush. This corresponds to a situation in which few transport factors can fully penetrate to the bottom of the brush and instead most remain near the surface. Without the formation of a dense layer of transport factors near the grafting surface, there is no energetic motivation for the nup brush to collapse, and a significant reduction in height will not be observed here. Although much emphasis is placed on the collapse transition, it should be noted that a morphology which involves kaps remaining near the top of
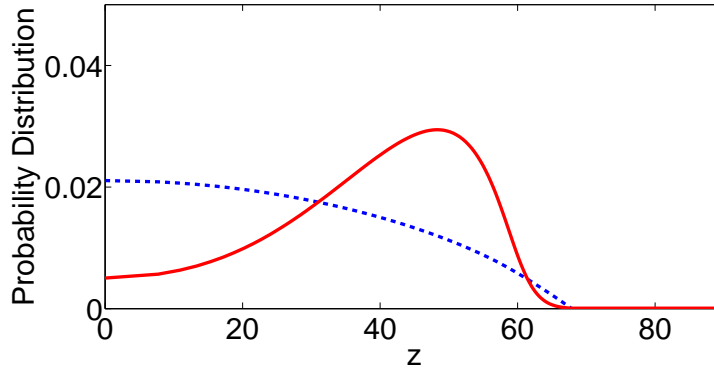
Figure 24: Monomer (dashed blue) and Nanoparticle (solid red) density profiles for the case $\bar{v} = 125$, $\chi = -175$, $a = 2.2$, $N = 100$, and $c = 10^{-4}$, as reproduced from Fig. 18. In this case, the concentration of the transport factors is highest in the edge of the nup brush, away from the grafting surface. This corresponds to an adsorption of the transport factors onto the top of the brush. Since the transport factors do not preferentially penetrate to the region near the grafting surface, this type of partial penetration will not cause a collapse of the layer.

the nup layer may be biologically relevant for the transport of larger cargoes. *In vivo* a failure of kaps to penetrate the brush could result in the formation of (or expansion of) a dense phase at the top of the brush near the channel center, potentially leaving a transport pathway in the sparser region near the grafting surface. This could be consistent with e.g. the forest model [23, 24] or simulations which have seen an analogous dense region in the channel center [151].

4.3.4 Analysis of Experimental results

Although the theoretical model used here is coarse-grained and considers only some of the essential features of the system, one can use it to better understand experimental results on nup-kap systems. In particular, we focus on three experiments which have similar setups, but have given seemingly contradictory results: Refs. [31, 34, 35]. In Ref. [34], Lim and coworkers consider the binding of the transport factor Kapβ1 to an *in vitro* system of surface grafted strands of the cNup153. In Ref. [31], Lim's group does a similar experiment, but with Kapβ1 and cNup62. Finally, in Ref. [35] Eisele, Görlich and cowork-
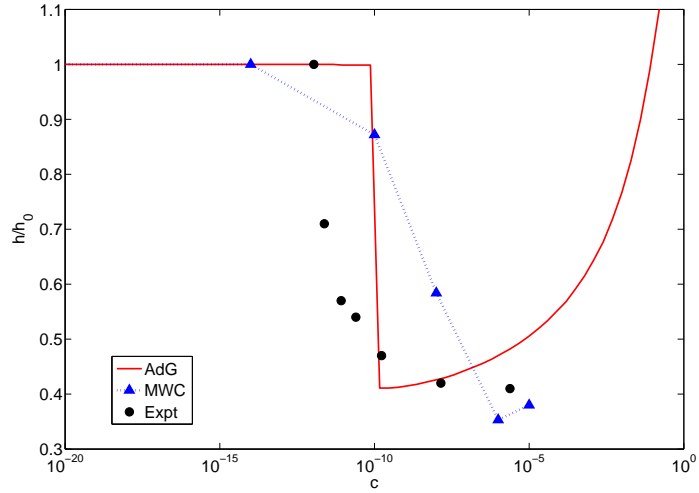
Figure 25: A comparison of the data from [34] with the results of our theory with the parameters $\bar{v} = 227$, $a = 9$, $\chi = -450$. Our theory predicts the substantial decrease in polymer height observed in the experiment with these parameters. While the Alexander-de Gennes model (AdG) predicts a discontinuous drop at a certain critical concentration, the Milner-Witten-Cates-based model (MWC) gives a more realistic gradual drop in the height.

ers perform a similar experiment, but using Kap95p and the nup Nsp1p. The aspects of these experiments relevant to our model are summarized in Table 1. The chemical details of the nups and kaps used in the three experiments are different, but we will subsume the differences into the parameter χ, which represents the net interaction between the nups and kaps. From this standpoint, two experimental parameters are relevant for our model: the ratio of the kap volume to the monomer volume $\bar{v}$ and the grafting distance a in units of the monomer diameter. a will be chosen based upon the reported grafting densities in the experiments, with adjustments allowed to account for aspects of the experiments not taken into account, as will be discussed below. In principle, the kap volume is fixed by the choice of b and a fitting such as that of section 4.2. However, it should be noted that the theory used is imprecise in modeling the detailed size and shape of the kap. As such, one can only expect this fitting to be a rough guide. We therefore allow ourselves some flexibility in choosing the kap volume, though we know it should be on the order of $\bar{v} \sim 227$ given our choice of $b = 1nm$. With a and $\bar{v}$ chosen in this way, the only fitting parameter

71

remaining to link our model to the three experiments is χ.

In Lim *et al.*'s 2007 experiment on grafted nups interacting with a solution of kaps [34], they found that at very low grafting densities (grafting distance $a \sim 24nm$) the nup brush strongly compressed in the presence of kaps, to about 40% of its height in the absence of kaps. We can approximate a similar situation by using a large value of a in our model along with our estimate of the kap volume, $\bar{v} = 227$. Although our choice of $b = 1nm$ would yield $a = 24$, we find that a better fit is obtained for $a = 9$. This may be due to a breakdown of the assumption of lateral inhomogeneity implicit in our model. Lim estimates the crossover to the mushroom regime (at which polymers cease to interpenetrate) at $a \sim 27nm$ [10]. Although his grafting distance is slightly less than this, it is likely that his system is beginning to lose its lateral inhomogeneity, particularly when the polymers contract in response to the transport factors. In addition, Lim *et al.* make a second measurement of the grafting distance using a different methodology and a flatter substrate but the same sample preparation method and obtain a value of $a = 10nm$ [10], which is much closer to our best-fit value. Varying χ to fit Lim's data, we obtain a best fit curve shown in Fig. 25. For these parameters, the Alexander-de Gennes model predicts a discontinuity in the brush height as a function of the solution kap concentration, while the MWC-type theory predicts a more realistic gradual decrease.

In Lim *et al.*'s 2012 experiment [31], they used a higher grafting density and a different combination of nups and kaps. In this study, they consider several grafting densities, but some of the results appear to be in the mushroom regime (where our theory does not apply), so we will focus on the case that is highlighted in their work. Here they observed a compression to about 90% of the height in the absence of kaps for a grafting distance of 2.4nm. We found that a good fit to the experimental data could be obtained by using the MWC-based theory with $a = 2.7$, which is approximately the same as the experimental value, $\bar{v} = 118$, about one half of the value we used in the previous case, and $\chi = -250$. The factor of two difference in kap volume used is not significant compared to the level of precision of the theory used. This choice of a and $\bar{v}$, along with the best-fit χ results in the fit of Fig. 26. As one can see in the figure, the Alexander-de Gennes model can also be fit to the experimental data, albeit with $a = 3.9$, $\bar{v} = 118$, and $\chi = -205$. The result of using the AdG model without refitting the parameters is also shown for comparison.

It should not be surprising that the MWC and AdG theories require somewhat different parameters in order to fit the data. Firstly, although the models are superficially similar and agree well in some
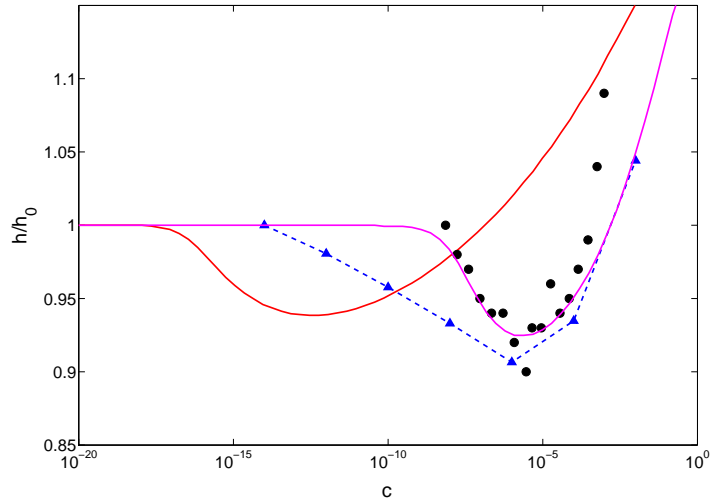
Figure 26: A comparison of the data from [31] (black dots) with the results of our theory. *Dashed Blue Line:* $\bar{v} = 118$, $a = 2.7$, $\chi = -250$ using MWC model. *Solid Red Line:* $\bar{v} = 118$, $a = 2.7$, $\chi = -250$ using AdG model. *Solid Pink Line:* $\bar{v} = 118$, $a = 3.9$, $\chi = -205$ using AdG model. Naturally, the fit is not exact, but our theory appears to give a qualitatively correct picture with a suitable parameter choice using either model. The red Alexander-de Gennes (AdG) curve is meant to show a comparison of the two models when the parameters are not re-fit. This produces a qualitatively similar curve in this case, but at a lower solution kap concentration.

cases, factors such as the spatial variation in the density and the stretching of the polymer chains are treated quite differently. There is no guarantee about whether these differences will noticeably manifest in particular cases. Furthermore, in some regions of parameter space, the theories can be fairly sensitive to parameter choices. Consulting Fig. 21, one can see for the analogous case of $\bar{v} = 227$ that for some parameter choices the system may be quite sensitive to changes in χ, while for other parameters it may be sensitive to a. Similarly, there may be regions where the system is more or less sensitive to the differences between the MWC and AdG theories, and smaller or larger parameter changes may be required to offset these. The difference in fitting parameters for the two theories suggests that our fitting of the theoretical parameters to the experimental ones will necessarily be inexact, though it can be guided by approximate fitting to the experiments.

The theoretical fit for the MWC-type model agrees well with experiment qualitatively, and the differences can be explained. Our model overestimates the compression of the brush at low kap concentrations, but this discrepancy is a known inaccuracy of the model used and is the same as the trend observed when comparing this theoretical model to Langevin dynamics simulations [83]. It is likely due to a breakdown of the mean field theory that underlies Eq. (4.1), which represents particles with their mean local density and ignores concentration fluctuations. The relative fluctuations will be more significant at low concentration. At high concentrations the discrepancies in the fit are due in part to the same geometrical imprecision which gives rise to the imprecision in the kap volume. Since the shape of the particles and the lattice they occupy when filling space is not precise, the density of the closely packed monomers and transport factors will be only approximately correct. The Alexander-de Gennes model's fit for the same parameters is also shown for comparison. In this case, the qualitative features of the curve are fairly accurate, but the compression occurs at a lower concentration.

After fitting the curve in this manner, we can examine the morphological details that the nups and kaps obtain. We find that for these parameters, the system is in the "collapse and recovery" regime described in section 4.3.2, in which a dense layer of kaps and nups forms near the grafting surface at intermediate kap concentrations (giving rise to the drop in the layer height). At higher concentrations a pileup of kaps results in a recovery and expansion of the layer. This appears to qualitatively corroborate the cartoon pictures hypothesized in Ref. [31] as well as their experimental results in terms of the change in layer height and the presence of two separate binding affinities (corresponding to the two separate densities of monomers and transport factors).

In a different experiment by Eisele *et al.* [35], a similar experimental setup was used, but in this case a compression of the polymer brush was not observed for a reported grafting distance of $4.4nm$. Although it is difficult to extract data of the type analyzed for the Lim experiments due to the experimental methods used, we can infer that the h vs. c curve for this experiment would be flat or nearly flat over the range of concentrations studied. In the context of our model, the grafting density used in this experiment must have been too high for collapse to be observed. Since the grafting density here was actually lower than that used in Ref. [31], this suggests that the strength of binding between Kap95p and Nsp1p is lower than the binding strength between Kapβ1 and cNup62. According to the data reported, the kaps did successfully penetrate the polymers, but the brush did not collapse as a result. This implies that the failure of the brush to collapse was due to the system being in the continuous penetration regime as described in section 4.3.1

or in the partial penetration as described in section 4.3.3. In both cases, the brush may be loaded with some kaps but fail to collapse. It is also possible that a small amount of compression did occur, but it was not observed to within the experimental precision. Since the maximum degree of compression might have only been a few percent in light of the modest compression in Ref. [31], it is possible that the compression was not significant enough to be detected. In fact, the supplementary information of Ref. [35] states that the error of the QCMB technique used is $\pm 4nm$, more than 10% of the unperturbed film thickness.

Although these three experiments seem contradictory in that three different compressions of the brush were obtained using similar experimental setups, the differences should not be surprising in light of Fig. 21, in which the effect of varying different parameters is represented. Since the experiments were performed using different combinations of nups and kaps and at different grafting densities, we can hypothesize that the experiments lie in qualitatively different regions of the plot. The brush of Ref. [34] underwent a dramatic collapse because of the low grafting density used. The brush of Ref. [31] underwent a smaller collapse because the experiment was performed at a higher grafting density. The lack of collapse in Ref. [35] might be due to a lower strength of the binding interaction between the nups and kaps used in this experiment, but it may be more likely that uncertainty in the measurements of the brush height masked a small amount of compression in Ref. [35].

Lastly, we consider the physical meaning of the interaction parameters obtained in the fits of Figs. 25 and 26. Our model includes many approximations, but we can use these best fit values of χ to provide an order of magnitude estimate of the real binding energy. Using the Alexander-de Gennes model for simplicity, the term in the final thermodynamic potential that represents the binding of the kaps and nups can be obtained by combining Eqs. (4.1) and (4.2) and is equal to $a^2 h \chi \phi \psi / \bar{v}$. Using $\phi = \bar{v} N_b / a^2 h$ where N_b is the numer of kaps in the nup layer, the free energy per kap can therefore be written as $\chi \psi$. Physically, χ represents both the binding strength of the interaction and the size and number of binding sites available on the kap, while the factor of ψ represents the concentration of FG repeats which will be nearby and therefore the fraction of the sites which will be occupied. The total binding energy that is possible if a kap is fully bound to the nups with every binding site occupied would be χ. Since we found that the experimental data can be fit by $\chi = -250$ or $\chi = -450$, we obtain a binding energy per kap of $\sim 250 kT$ or $\sim 450 kT$. Assuming that this energy is shared by $\sim 5 - 10$ binding sites [155], we estimate individual binding events to have binding energies on the order of $25 - 90 kT$. This suggests that fairly

strong binding between nups and kaps is necessary to offset the free energetic cost of layer collapse, but it should be emphasized that this estimate depends upon many approximations implicit in the model and fitting procedure used here.

4.4 CONCLUSIONS AND DISCUSSION

Although the available experimental data concerning the binding of nucleoporins to the transport factors in the nuclear pore complex appear at first glance to be inconsistent (insofar as both layer collapse and the absence of layer collapse have been reported), we present here a very simple theoretical model which can qualitatively explain the discrepancies among these experiments. Our model does not attempt to represent the nups and kaps with atomic or even amino-acid scale accuracy, but rather encapsulates the key physical features of the problem into results that can be clearly understood. Namely, if one varies the grafting density of the nups, binding affinity between the nups and kaps, and volume of the kaps, three distinct regimes can be observed. In one case, the layer does not collapse because the binding energy is insufficient to overcome the free energy cost associated with the reorganization of the nup chains. In a second regime, the kaps are unable to fully penetrate the nup brush and therefore cannot induce a collapse. In the third, collapse does occur because the grafting density is low enough and the binding energy is high enough that the nup chains can overcome the free energy penalty associated with the collapse by offsetting it with the energy associated with binding.

In addition to providing a qualitative explanation that can reconcile differences between the experimental results, our model can serve as a predictive guide for future experiments. For example, if one consults Fig. 21, one can predict that Görlich and coworkers could perform their experiment at a lower grafting density and see a similar collapse as that observed by Lim's group. The typical grafting distance in the NPC is on the order of that used in Görlich's experiment [35, 156], but one must remember that the actual geometry of the NPC is highly non-planar, and given the sensitivity of the system to parameters, it is difficult to predict from the aforementioned experiments or the work discussed here whether the nups in the pore would collapse, fail to collapse, or even obtain a morphology for which the non-planar geometry is crucial, such as that predicted by the forest model where there could be a dense region analogous to our collapsed layer in a location other than along the channel wall. However, before an attempt to

76

relate these experiments to the NPC *in vivo* can hope to succeed, we must gain a heuristic appreciation of the parameter space in which experiments are being performed and a recognition of when different experimental results are to be expected.

5.0   CONCLUSIONS

In this thesis I have examined the behavior of grafted polymers when interacting with additives that interact attractively with the polymers. I analyzed the system in Chapter 2 with a simpler Alexander-de Gennes theory, which assumes a uniform density of monomers and nanoparticles throughout the layer, and in Chapter 3 with a more complex Milner-Witten-Cates self-consistent field theory. These theoretical finding are corroborated by Langevin dynamics simulations. Finally, I applied this model to further the understanding of the grafted proteins found in the nuclear pore complex when they interact attractively with transport factors in Chapter 4.

Broadly speaking, we have found that the attractive nanoparticles are capable of inducing a collapse of the polymer layer. This collapse is often characterized by the formation of a dense layer of monomers and nanoparticles near the grafting surface. The Alexander-de Gennes theory predicts this collapse as a discontinuous drop in the height of the polymer layer at a certain critical solution concentration of nanoparticles, while the MWC theory predicts a continuous decrease, but one that is characterized by discontinuous monomer and nanoparticle density profiles.

This type of collapse does not occur for all possible system parameters. If the attractive interaction between the monomers and nanoparticles is not strong enough, the compression of the layer is not as significant and it is not characterized by a discontinuous density profile. Rather, the nanoparticles act as a small perturbation on the ordinary polymer brush. Another regime exists at large nanoparticle sizes compared to the grafting distance of the polymers. In this regime, nanoparticles cannot penetrate the small spaces between the polymers to reach the grafting surface. Instead, they remain near the top of the brush, where the density of monomers is lower.

The observation of different parameter regimes is significant when considering applications to the nuclear pore complex system. Experiments in this field have produced inconsistent results in that collapse has only been observed in certain cases. Our theory provides a qualitative explanation as to why

these results occur. The experiments were performed with different experimental parameters and probed different regimes. The recognition that simple models such as the ones we present here can explain the different results should help to resolve disagreements in the community and promote experiments and NPC models which take advantage of the understanding of different parameter regimes presented here.

APPENDIX A

COUNTING STATES IN THE LATTICE GAS MODEL

When calculating contributions to polymer free energies, we frequently invoke approximations via a lattice gas model. In this approach, one divides space into discrete lattice sites and counts states based on the assumption that the polymer is made of disconnected monomer beads in a random (gaseous) arrangement on a lattice. One can then approximately correct this starting point in order to take into account the polymer's connectivity. An alternate approach would be to avoid making the assumption that monomers are arranged randomly in a gas, and instead count states based on the assumption that each monomer must occupy an adjacent lattice site to the monomers connected to it in the polymer chain. However, in order for the problem to be tractable, self-avoidance is typically only considered at the mean field level [39]. Although it is not conceptually obvious that either approach should generate an accurate free energy since a number of assumptions and approximations underly both methods, it is encouraging that they give the same result (modulo a physically irrelevant additive constant). In addition, a van der Waals version of the derivation produces a free energy which is different in some details but produces a generally qualitatively similar result in terms of, for example, the scaling of the free energy with crucial parameters such as the nanoparticle volume. Thus, though the method used here is inexact, it appears to give qualitatively reasonable results and ultimately was found to agree well with the simulation results presented in chapters 2 and 3. However, it should be emphasized that the following derivation is approximate and does not explicitly count the possible physically correct conformations of the polymers in all circumstances.

A.1 POLYMER BRUSH WITHOUT NANOPARTICLES

Imagine that space is divided into a lattice with M sites. Onto this lattice, randomly place N monomers such that only one particle can occupy each lattice site. The number of possible configurations Ω will be

$$\Omega = \frac{M!}{N!(M-N)!} \tag{A.1}$$

Equating the entropy of this system to $\ln \Omega$, we can obtain (in units of kT)

$$F = M\left(\psi \ln \psi + (1-\psi)\ln(1-\psi)\right) \tag{A.2}$$

where $\psi = N/M$ is the fraction of lattice sites occupied by monomers. Note that Sterling's approximation has been used and the (ultimately physically irrelevant) terms linear in ψ have been discarded. The first term in Eq. (A.3) represents the translational entropy of the monomers, while the second term represents the translational entropy of the empty lattice sites.

In order to make this free energy suitable for a polymer chain, in which monomers do not have the translational entropy implied by Eq. (A.3), the term $\psi \ln \psi$ must be discarded and replaced by the elastic energy of stretching of a polymer chain. (Note that terms linear in ψ do not contribute to the relevant thermodynamic derivatives, and we will not include such terms when taking the translational entropy into account.) The appropriate stretching entropy for a polymer brush is $h^2/2N$ per chain. This procedure is followed e.g. by de Gennes [37]. The corrected free energy then becomes

$$F = \frac{h^2}{2N} + M(1-\psi)\ln(1-\psi). \tag{A.3}$$

This is equivalent to the free energy used in Eq. (1.1) when one notes that the system volume is $M = a^2 h$.

A.2 POLYMER BRUSH WITH SMALL NANOPARTICLES

If the polymer layer consists of polymer chains mixed with nanoparticles that are the same size as the monomers, then the lattice gas counting becomes

$$\Omega = \frac{M!}{N!N_B!(M-N-N_B)!} \tag{A.4}$$

where N_B is the number of nanoparticles in the polymer layer. Calculating $F = -\ln\Omega$, and again using Stirling's approximation,

$$F = M\left(\psi\ln\psi + \phi\ln\phi + (1-\psi-\phi)\ln(1-\psi-\phi)\right), \tag{A.5}$$

where ϕ is the fraction of sites in the layer occupied by nanoparticles. After correcting for the connectivity of the polymers in the same way,

$$F = \frac{h^2}{2N} + M\left(\phi\ln\phi + (1-\psi-\phi)\ln(1-\psi-\phi)\right). \tag{A.6}$$

This is equivalent to the free energy used in Eq. (2.1).

A.3 POLYMER BRUSH WITH LARGE NANOPARTICLES

Now we consider the case in which the nanoparticles and monomers do not have the same size. In particular, let the ratio of the nanoparticle volume to the monomer volume be v. That is, the nanoparticles occupy v lattice sites. In order to represent the fact that the large nanoparticles must occupy v adjacent sites, they are placed on a superlattice that has M/v sites. This gives a counting of states for the nanoparticles to be

$$\Omega_1 = \frac{(M/v)!}{N_B!(M/v-N_B)!}. \tag{A.7}$$

After the nanoparticles are placed, the monomers are placed in the remaining free volume. The counting of states for the monomers is then

$$\Omega_2 = \frac{(M-vN_B)!}{N!(M-vN_B-N)!}. \tag{A.8}$$

The uncorrected free energy can then be calculated as $F = -\ln \Omega_1 \Omega_2$, namely,

$$F = \frac{M}{v} \left(v\psi \ln \psi + \phi \ln \phi - (1-v)(1-\phi) \ln(1-\phi) + v(1-\psi-\phi) \ln(1-\psi-\phi) \right). \quad \text{(A.9)}$$

Note that in this case ϕ represents the fraction of the smaller lattice sites that are occupied by the nanoparticles: $\phi = vN_B/M$, while $\psi = N/M$ as before. Removing the translational entropy of the monomers and adding the stretching entropy as before,

$$F = \frac{h^2}{2N} + \frac{M}{v} \left(\phi \ln \phi - (1-v)(1-\phi) \ln(1-\phi) + v(1-\psi-\phi) \ln(1-\psi-\phi) \right). \quad \text{(A.10)}$$

This is essentially the Alexander-de Gennes form of the free energy used in Chapters 3 and 4.

APPENDIX B

THE MAXWELL EQUAL AREAS CONSTRUCTION AND THE OSMOTIC PRESSURE FOR A POLYMER BRUSH INFILTRATED BY NANOPARTICLES

Starting with the free energy density of Eq. (3.2), we can obtain the osmotic pressure Π and the chemical potential of the monomers (excluding the elastic term) and nanoparticles μ_m and μ_b through the thermodynamic derivatives

$$\Pi = -\frac{\partial}{\partial V}(V f_{int}(\psi, \phi)) = \frac{\chi}{\bar{v}}\phi\psi - \psi + \left(1 - \frac{1}{v}\right)\ln(1-\phi) - \ln(1-\psi-\phi), \qquad \text{(B.1)}$$

$$\mu_m = \frac{\partial f_{int}(\psi, \phi)}{\partial \psi} = -\ln(1-\psi-\phi) + \frac{\chi}{\bar{v}}\phi - 1, \qquad \text{(B.2)}$$

and

$$\mu_b = \frac{\partial f_{int}(\psi, \phi)}{\partial \phi} = \chi\psi + \ln\left(\frac{\phi(1-\phi)^{\bar{v}-1}}{(1-\psi-\phi)^{\bar{v}}}\right). \qquad \text{(B.3)}$$

Note that the partial derivative used to determine the osmotic pressure in Eq. (B.1) is to be carried out at constant particle number rather than constant density. $f_{int}(\psi, \phi)$ must first be changed into $f_{int}(V, N_b)$, where N_b is the number of nanoparticles bound in the polymer layer, using $\psi = N/V$ and $\phi = \bar{v}N_b/V$. It can be shown that Eqs. (3.2), (B.1), (B.2), and (B.3) are related by

$$f_{int} = -\Pi + \mu_m\psi + \frac{1}{\bar{v}}\phi\mu_b. \qquad \text{(B.4)}$$

Since nanoparticles are free to move within the layer and are exchanged between the polymer layer and the solution above, the chemical potential of the nanoparticles is constant throughout the layer and its value is fixed by the concentration of the solution above μ_c. This chemical potential can be obtained

by writing the free energy of the (one-component) solution above the layer and taking the appropriate thermodynamic derivative. Namely,

$$\mu_b = \mu_c = \ln\left(\frac{c}{1-c}\right), \tag{B.5}$$

which can be obtained via the same type of lattice gas counting arguments discussed in Appendix A.

For a specified value of ψ, Eqs. (B.3) and (B.5) can be solved to obtain a unique value of ϕ in the interval $0 < \phi < (1 - \psi)$. In general, only a numerical solution is available, but for the special case of $\bar{v} = 1$, which is the case considered in Chapter 2, an analytical solution is available. Namely,

$$\phi_{\bar{v}=1}(\psi) = \frac{1-\psi}{1 + \exp(\chi\psi - \mu_s)}. \tag{B.6}$$

After solving for $\phi(\psi)$ and substituting into Eqs. (B.1) and (B.2), $\Pi(\psi, \phi)$ and $\mu_m(\psi, \phi)$ become functions of one variable only: $P(\psi)$ and $\mu(\psi)$. In particular, since the total derivative of $f_{int}(\psi, \phi)$ can be written as

$$\frac{d}{d\psi} f_{int}(\psi, \phi) = \frac{\partial f_{int}}{\partial \psi} + \frac{\partial f_{int}}{\partial \phi}\frac{d\phi}{d\psi} \tag{B.7}$$

$$= \mu_m + \frac{1}{\bar{v}}\mu_b \frac{d\phi}{d\psi}, \tag{B.8}$$

the relationship between ϕ and ψ at equilibrium can be used to obtain

$$\left(\frac{d}{d\psi} f_{int}(\psi, \phi)\right)_{\phi=\phi(\psi)} = \mu(\psi) + \frac{1}{\bar{v}}\mu_b \left(\frac{d\phi}{d\psi}\right)_{\phi=\phi(\psi)}. \tag{B.9}$$

An unexpected feature of the function $\mu(\psi)$ is that in some cases it may be non-monotonic and possess a van der Waals loop. The presence of this loop ultimately corresponds to the highly inhomogeneous layer morphologies discussed in Chapters 3 and 4. In order to make $\mu(\psi)$ a monotonic function of ψ we must excise the loop. This corresponds to choosing an upper and lower value of ψ at which $\mu(\psi_u) = \mu(\psi_\ell)$ and replacing the function $\mu(\psi)$ between these two values of ψ with a horizontal tie line. In other words, in the range $\psi_\ell \leq \psi \leq \psi_u$, we make $\mu(\psi)$ a constant value μ_{tie}, which is equal to $\mu(\psi_\ell)$ and $\mu(\psi_u)$. Although, in principle, many values of ψ_ℓ and ψ_u have this property, they can be chosen uniquely by also requiring mechanical stability of the polymer layer. This will occur only if the loop is excised in

such a way that the osmotic pressure is continuous everywhere, corresponding to $P(\psi_u) = P(\psi_\ell)$. This condition is equivalent to using Maxwell's equal areas method, which can be stated as

$$\int_{\psi_\ell}^{\psi_u} \mu(\psi)d\psi = \mu_{tie}(\psi_u - \psi_\ell), \tag{B.10}$$

as will be proved below.

Starting from Eq. (B.10), we first explicitly take the anti-derivative $G(\psi)$ of the integrand $\mu(\psi)$. Eq. (B.10) then becomes

$$G(\psi_u) - G(\psi_\ell) = \mu_{tie}(\psi_u - \psi_\ell). \tag{B.11}$$

Since by definition $dG(\psi)/d\psi = \mu(\psi)$, we can write Eq. (B.9) as

$$\left(\frac{d}{d\psi} f_{int}(\psi, \phi)\right)_{\phi=\phi(\psi)} = \frac{dG}{d\psi} + \frac{1}{\bar{v}}\mu_b \left(\frac{d\phi}{d\psi}\right)_{\phi=\phi(\psi)}. \tag{B.12}$$

This equation implies

$$G(\psi) = f_{int}(\psi, \phi(\psi)) - \frac{1}{\bar{v}}\mu_b\phi(\psi), \tag{B.13}$$

perhaps with an additive constant which will be irrelevant here. Combining this with Eq. (B.4), we obtain

$$G(\psi) = -P(\psi) + \mu(\psi)\psi. \tag{B.14}$$

Finally, we combine Eqs. (B.11) and (B.14) to obtain

$$P(\psi_\ell) - P(\psi_u) = 0. \tag{B.15}$$

Therefore, the osmotic pressure is continuous in the layer even if the monomer concentration undergoes a discontinuity due to treatment of the the van der Waals loop. Furthermore, setting the osmotic pressure equal at the discontinuity is equivalent to performing the Maxwell equal areas construction on the van der Waals loop in the function $\mu(\psi)$. As a result, there are two equivalent methods to excise the loop in a physically correct manner. One can perform the Maxwell construction directly, or one can choose the discontinuity such that the osmotic pressure is continuous. In addition, the existence of two methods can provide a computational double-check on a numerical solution.

APPENDIX C

SOLVING THE MILNER-WITTEN-CATES MODEL WITH NANOPARTICLES

In this appendix I will sketch how the stationary point of the free energy function Eq. (3.1) is found in order to obtain the equilibrium conditions Eqs. (3.3) and (3.4). The first variation δF of the functional is obtained by varying the polymer trajectories $\{\vec{r}_\alpha\}$ and the nanoparticle volume fraction ϕ from their minimum energy state equilibrium state, and then the stationary point is found by setting $\delta F = 0$.

Let us first find the first variation of the stretching term in Eq. (3.1), which may be written as

$$\sum_\alpha \frac{1}{2b^2} \int_0^N ds \left(\frac{\partial}{\partial s} \vec{r}_\alpha(s) \right)^2 = \sum_\alpha \frac{1}{2b^2} \int_0^N ds \left(\dot{x}_\alpha^2(s) + \dot{y}_\alpha^2(s) + \dot{z}_\alpha^2(s) \right) \tag{C.1}$$

where the dot has been used to represent a derivative with respect to s. For simplicity, let us consider one term in this sum only: the z component term from a single chain. Adding a small variation δz to $z(s)$ yields

$$\frac{1}{2b^2} \int_0^N ds \left(\dot{z} + \delta \dot{z} \right)^2 = \frac{1}{2b^2} \int_0^N ds \dot{z}^2 + \frac{1}{2b^2} \int_0^N ds \left(2 \dot{z} \delta \dot{z} \right) \tag{C.2}$$

to first order in the variation. The last term on the right hand side can be integrated by parts to obtain

$$\int_0^N ds \dot{z} \delta \dot{z} = \dot{z} \delta z \big|_0^N - \int_0^N ds \ddot{z} \delta z. \tag{C.3}$$

The boundary term vanishes because at $s = 0$, $\delta z = 0$ since every chain is end-grafted, while at $s = N$, $\dot{z} = 0$ because at equilibrium the tension in the chain must be zero at the free end, and we assume that the dominant contributions will come from those close to the equilibrium state. By carrying out the same procedure on the x and y terms, one can see that the first variation of this term is

$$\delta \left(\sum_\alpha \frac{1}{2b^2} \int_0^N ds \left(\frac{\partial}{\partial s} \vec{r}_\alpha(s) \right)^2 \right) = \sum_\alpha \frac{1}{b^2} \int_0^N ds \left(\ddot{\vec{r}}_\alpha(s) \cdot \delta \vec{r}_\alpha \right). \tag{C.4}$$

To treat the other terms in Eq. (3.1), which depend on ψ and ϕ, we can write their variation as

$$\delta\left(\frac{1}{b^3}\int d^3r(f(\psi(\vec{r}),\phi(\vec{r})) - \frac{1}{\bar{v}}\mu_c\phi(\vec{r}))\right) = \frac{1}{b^3}\int d^3r\left(\frac{\partial f(\psi,\phi)}{\partial\psi}\delta\psi + \left(\frac{\partial f(\psi,\phi)}{\partial\phi} - \frac{\mu_c}{\bar{v}}\right)\delta\phi\right).$$
(C.5)

Note that the variation in the polymer trajectories $\{\vec{r}_\alpha\}$ corresponds directly to a variation in the monomer volume fraction ψ. ϕ, on the other hand, must be varied separately. As a result, $\delta F = 0$ requires two separate conditions. First the prefactor of $\delta\phi$ must be zero. This yields

$$\frac{\mu_c}{\bar{v}} = \frac{\partial f(\psi,\phi)}{\partial\phi}.$$
(C.6)

This provides Eq. (3.3) which relates ψ and ϕ at equilibrium.

After this condition has been taken into account, the remaining terms in δF from Eqs. (C.4) and (C.5) give

$$\sum_\alpha \frac{1}{b^2}\int_0^N ds\left(\ddot{\vec{r}}_\alpha(s)\cdot\delta\vec{r}_\alpha\right) + \frac{1}{b^3}\int d^3r\frac{\partial f(\psi,\phi)}{\partial\psi}\delta\psi = 0.$$
(C.7)

In order to reduce this expression, we must convert the integral over the spatial coordinates into an integral over s. This can be done by noting that

$$\psi(\vec{r}) = b^3\sum_\alpha\int ds\delta(\vec{r} - \vec{r}_\alpha(s))$$
(C.8)

so that

$$\delta\psi = b^3\sum_\alpha\int ds\delta(\vec{r} - \vec{r}'_\alpha(s)) - \sum_\alpha\int ds\delta(\vec{r} - \vec{r}_\alpha(s))$$
(C.9)

where $\{\vec{r}'_\alpha\}$ denotes the positions of the monomers after the variation has been applied. In addition, we note that since ψ and ϕ are functions of $\vec{r}$, $\partial f(\psi,\phi)/\partial\psi$ can be regarded as a function $\mu(\vec{r})$. Then

$$\begin{aligned}
\int d^3r\frac{\partial f(\psi,\phi)}{\partial\psi}\delta\psi &= \int d^3r\mu(\vec{r})\delta\psi\\
&= b^3\int d^3r\mu(\vec{r})\left(\sum_\alpha\int ds\delta(\vec{r} - \vec{r}'_\alpha(s)) - \sum_\alpha\int ds\delta(\vec{r} - \vec{r}_\alpha(s))\right)\\
&= b^3\sum_\alpha\int ds\left(\mu(\vec{r}'_\alpha(s)) - \mu(\vec{r}_\alpha(s))\right)\\
&= b^3\sum_\alpha\int ds\nabla_\alpha\mu\cdot\delta\vec{r}_\alpha.
\end{aligned}$$
(C.10)

Inserting Eq. (C.10) into Eq. (C.7), we obtain

$$\sum_\alpha \int ds \left(\nabla_\alpha \mu - \frac{1}{b^2} \ddot{\vec{r}}_\alpha \right) \cdot \delta\vec{r}_\alpha = 0. \tag{C.11}$$

Setting the expression in parentheses equal to zero yields an equation which can be mapped onto Newton's second law for a particle moving in the potential $-\mu(\vec{r})$, as in Eq. (3.4).

BIBLIOGRAPHY

[1] Q. Yang, M. P. Rout, and C. W. Akey. Three-dimensional architecture of the isolated yeast nuclear pore complex: functional and evolutionary implications. *Mol Cell*, 1:223–234, 1998.

[2] I. G. Macara. Transport into and out of the nucleus. *Microbiol. Mol. Biol. Rev.*, 65:570–594, 2001.

[3] K. Ribbeck and D. Görlich. Kinetic analysis of translocation through nuclear pore complexes. *EMBO J.*, 20:1320–1330, 2001.

[4] R. Y. H. Lim and B. Fahrenkrog. The nuclear pore complex up close. *Curr. Opin. Cell Biol.*, 18: 342–347, 2006.

[5] M. Suntharalingam and S. R. Wente. Peering through the pore: Nuclear pore complex structure, assembly, and function. *Dev. Cell*, 4:775–789, 2003.

[6] D. P. Denning, S. S. Patel, V. Uversky, A. L. Fink, and M. Rexach. Disorder in the nuclear pore complex: The fg repeat regions of nucleoporins are natively unfolded. *PNAS*, 100:2450–2455, 2003.

[7] V. V. Krishnan, E. Y. Lau, J. Yamada, D. P. Denning, S. S. Patel, M. E. Colvin, and M. F. Rexach. Intramolecular cohesion of coils mediated by phenylalanine-glycine motifs in the natively unfolded domain of a nucleoporin. *PLOS Computational Biology*, 4:e1000145, 2008.

[8] M. Rout and S. Wente. Pores for thought: nuclear pore complex proteins. *Trends Cell Biol.*, 4: 357–365, 1994.

[9] A. Hoelz, E. W. Debler, and G. Blobel. The structure of the nuclear pore complex. *Annu. Rev. Biochem.*, 80:613–643, 2011.

[10] R. Y. H. Lim, N.-P. Huang, J. Köser, J. Deng, K. H. A. Lau, K. Schwarz-Herion, B. Fahrenkrog, and U. Aebi. Flexible phenylalanine-glycine nucleoporins as entropic barriers to nucleocytoplasmic transport. *PNAS*, 103:9512–9517, 2006.

[11] M. Stewart, R. P. Baker, R. Bayliss, L. Clayton, R. P. Grant, T. Littlewood, and Y. Matsuura. Molecular mechanism of translocation through nuclear pore complexes during nuclear protein import. *FEBS Letters*, 498:145–149, 2001.

[12] B. Fahrenkrog and U. Aebi. The nuclear pore complex: nucleocytoplasmic transport and beyond. *Nat. Rev. Mol. Cell Biol.*, 4:757–766, 2003.

[13] J. M. Cronshaw and M. J. Matunis. The nuclear pore complex: disease associations and functional correlations. *Trends Endocrin. Met.*, 15:34–39, 2004.

[14] M. A. van der Aa, E. Mastrobattista, R. S. Oosting, W. E. Hennink, G. A. Koning, and D. J. Crommelin. The nuclear pore complex: The gateway to successful nonviral gene delivery. *Pharmaceutical Research*, 23:447–459, 2006.

[15] H. P. Erickson. Size and shape of protein molecules at the nanometer level determined by sedimentation, gel filtration, and electron microscopy. *Biol. Proced. Online*, 11:32–51, 2009.

[16] N. Panté and M. Kann. Nuclear pore complex is able to transport macromolecules with diameters of about 39 nm. *Mol. Biol. Cell*, 13:425–434, 2002.

[17] R. Peters. Translocation through the nuclear pore complex: Selectivity and speed by reduction-of-dimensionality. *Traffic*, 6:421–427, 2005.

[18] T. Imasaki, T. Shimizu, H. Hashimoto, Y. Hidaka, S. Kose, N. Imamoto, M. Yamada, and M. Sato. Structural basis for substrate recognition and dissociation by human transportin 1. *Mol. Cell*, 28: 57–67, 2007.

[19] M. Rexach and G. Blobel. Protein import into nuclei: Association and dissociation reactions involving transport substrate, transport factors, and nucleoporins. *Cell*, 83:683–692, 1995.

[20] Y. M. Chook and G. Blobel. Structure of the nuclear transport complex karyopherin-β2-rangppnhp. *Nature*, 399:230–237, 1999.

[21] R. B. Kopito and M. Elbaum. Reversibility in nucleocytoplasmic transport. *PNAS*, 104:12743–12748, 2007.

[22] R. Bayliss, S. W. Leung, R. P. Baker, B. B. Quimby, A. H. Corbett, and M. Stewart. Structural basis for the interaction between ntf2 and nucleoporin fxfg repeats. *EMBO J.*, 21:2843–2853, 2002.

[23] J. Yamada, J. L. Phillips, S. Patel, G. Goldfien, A. Calestagne-Morelli, H. Huang, R. Reza, J. Acheson, V. V. Krishnan, S. Newsam, A. Gopinathan, E. Y. Lau, M. E. Colvin, V. N. Uversky, and M. F. Rexach. A bimodal distribution of two distinct categories of instrinsically disordered structures with separate function in fg nucleoporins. *Molecular & Cellular Proteomics*, 9:2205–2224, 2010.

[24] J. Kim, A. Izadyar, N. Nioradze, and S. Amemiya. Nanoscale mechanism of molecular transport through the nuclear pore complex as studied by scanning electrochemical microscopy. *J. Am. Chem. Soc.*, 135:2321–2329, 2013.

[25] J. S. Mincer and S. M. Simon. Simulations of nuclear pore transport yield mechanistic insights and quantitative predictions. *PNAS*, 108:351–358, 2011.

[26] M. A. Powers and D. J. Forbes. Nuclear transport: Beginning to gel. *Curr. Biol.*, 22:1006–1009, 2012.

[27] S. Frey, R. P. Richter, and D. Görlich. Fg-rich repeats of nuclear pore proteins form a three-dimensional meshwork with hydrogel-like properties. *Science*, 314:815–817, 2006.

[28] B. B. Hülsmann, A. A. Labokha, and D. Görlich. The permeability of reconstituted nuclear pores provides direct evidence for the selective phase model. *Cell*, 150:738–751, 2012.

[29] A. A. Labokha, S. Gradmann, S. Frey, B. B. Hülsmann, H. Urlaub, M. Baldus, and D. Görlich. Systematic analysis of barrier-forming fg hydrogels from xenopus nuclear pore complexes. *EMBO J.*, 32:204–218, 2013.

[30] R. Y. H. Lim, B. Fahrenkrog, J. Köser, K. Schwarz-Herion, J. Deng, and U. Aebi. Nanomechanical basis of selective gating by the nuclear pore complex. *Science*, 318:640–643, 2007.

[31] R. L. Schoch, L. E. Kapinos, and R. Y. H. Lim. Nuclear transport receptor binding avidity triggers a self-healing collapse transition in fg-nucleoporin molecular brushes. *PNAS*, 109:16911–16916, 2012.

[32] M. P. Rout, J. D. Aitchison, A. Suprapto, K. Hjertaas, and Y. Zhao. The yeast nuclear pore complex: Composition, architecture, and transport mechanism. *J. Cell Biol.*, 148:635–651, 2000.

[33] S. S. Patel, B. J. Belmont, J. M. Sante, and M. F. Rexach. Natively unfolded nucleoporins gate protein diffusion across the nuclear pore complex. *Cell*, 129:83–96, 2007.

[34] R. Lim, B. Fahrenkrog, J. Köser, K. Schwarz-Herion, J. Deng, and U. Aebi. Nanomechanical basis of selective gating by the nuclear pore complex. *Science*, 318:640–643, 2007.

[35] N. B. Eisele, S. Frey, J. Piehler, D. Görlich, and R. P. Richter. Ultrathin nucleoporin phenylalanine-glycine repeat films and their interaction with nuclear transport receptors. *EMBO Rep.*, 11:366–372, 2010.

[36] R. Y. H. Lim, N. P. Huang, J. Kser, J. Deng, K. H. A. Lau, K. Schwarz-Herion, B. Fahrenkrog, and U. Aebi. Flexible phenylalanine-glycine nucleoporins as entropic barriers to nucleocytoplasmic transport. *Proceedings of the National Academy of Sciences*, 103(25):9512–9517, 2006.

[37] P. G. de Gennes. Conformations of polymers attached to an interface. *Macromolecules*, 13:1069–1075, 1980.

[38] S. Alexander. *J. Phys. (Paris)*, 38:983, 1977.

[39] P. J. Flory. Thermodynamics of high polymer solutions. *J. Chem. Phys.*, 10:51–61, 1942.

[40] M. Doi and S. F. Edwards. *The Theory of Polymer Dynamics*. Oxford University Press, 1988.

[41] S. T. Milner. Polymer brushes. *Science*, 251:905–914, 1991.

[42] C. Williams, F. Brochard, and H. L. Frisch. Polymer collapse. *Ann. Rev. Phys. Chem.*, 32:433–451, 1981.

[43] J. D. McCoy, Y. Ye, and J. G. Curro. Application of density functional theory to thethered polymer chains: Athermal systems. *J. Chem. Phys.*, 117:2975–2988, 2002.

[44] P. G. de Gennes. *Scaling Concepts in Polymer Physics*. Cornell University Press, 1979.

[45] C. Yeung, A. Balazs, and D. Jasnow. Lateral instabilities in a grafted layer in a poor solvent. *Macromolecules*, 26(8):1914–1921, 1993.

[46] S. T. Milner, T. A. Witten, and M. E. Cates. Theory of the grafted polymer brush. *Macromolecules*, 21:2610–2619, 1988.

[47] E. B. Zhulina, O. V. Borisov, and V. A. Priamitsyn. *J. Colloid Interface Sci.*, 137:495–511, 1990.

[48] M. Wagner, F. Brochard-Wyart, H. Hervet, and P.-G. de Gennes. Collapse of polymer brushes induced by n-clusters. *Colloid Polym. Sci.*, 271:621–628, 1993.

[49] P. Lai and A. Halperin. Polymer brushes in mixed solvents: chromatography and collapse. *Macromolecules*, 25(24):6693–6695, 1992.

[50] J. Marko. Polymer brush in contact with a mixture of solvents. *Macromolecules*, 26(2):313–319, 1993.

[51] P. Auroy and L. Auvray. Collapse-stretching transition for polymer brushes. preferential solvation. *Macromolecules*, 25:4134–4141, 1992.

[52] T. M. Birshtein and Y. V. Lyatskaya. Theory of the collapse-stretching transition of a polymer brush in a mixed solvent. *Macromolecules*, 27:1256–1266, 1994.

[53] Y. Lyatskaya and A. Balazs. Phase separation of mixed solvents within polymer brushes. *Macromolecules*, 30(24):7588–7595, 1997.

[54] T. Birshtein, A. Mercurieva, and E. Zhulina. Deformation of a polymer brush immersed in a binary solvent. *Macromolecular Theory and Simulations*, 10(7):719–728, 2001.

[55] V. Amoskov, T. Birshtein, and A. Mercurieva. Scf theory of a polymer brush immersed into a multi-component solvent. *Macromolecular theory and simulations*, 15(1):46–69, 2006.

[56] D. I. Dimitrov, A. Milchev, and K. Binder. Polymer brushes in solvents of variable quality: Molecular dynamics simulations using explicit solvent. *J. Chem. Phys.*, 127:084905, 2007.

[57] V. A. Baulin and A. Halperin. Signatures of a concentration-dependent flory χ parameter: Swelling and collapse of coils and brushes. *Macromol. Theory Simul.*, 12:549–559, 2003.

[58] T. M. Birshtein, A. A. Mercurieva, and E. B. Zhulina. Deformation of a polymer brush immersed in a binary solvent. *Macromol. Theory Simul.*, 10:719–728, 2001.

[59] V. M. Amoskov, T. M. Birshtein, and A. A. Mercurieva. Scf theory of a polymer brush immersed into a multi-component solvent. *Macrmol. Theory Simul.*, 15:46–69, 2006.

[60] P. Auroy, L. Auvray, and L. Leger. Structures of end-grafted polymer layers: a small-angle neutron scattering study. *Macromolecules*, 24(9):2523–2528, 1991.

[61] T.-M. Don, J. P. Bell, and M. Narkis. Antiplasticization behavior of polycaprolactone/polycarbonate-modified epoxies. *Polym. Eng. Sci.*, 36:2601, 1996.

[62] A. K. Dasmahapatra, H. Nanavati, and G. Kumaraswamy. Polymer srystallization in the presence of "sticky" additives. *J. Chem. Phys.*, 131:074905, 2009.

[63] I. Luzinov, S. Minko, and V. Tsukruk. Responsive brush layers: from tailored gradients to reversibly assembled nanoparticles. *Soft Matter*, 4(4):714–725, 2008.

[64] M. A. C. Stuart, W. T. Huck, J. Genzer, M. Müller, C. Ober, M. Stamm, G. B. Sukhorukov, I. Szleifer, V. V. Tsukruk, M. Urban, F. Winnik, S. Zauscher, I. Luzinov, and S. Minko. Emerging applications of stimuli-responsive polymer materials. *Nature materials*, 9(2):101–113, 2010.

[65] N. Camaioni, M. Catellani, S. Luzzati, and A. Migliori. Morphological characterization of poly(3-octylthiophene):plasticizer:c_{60} blends. *Thin Solid Films*, 403–404:489–494, 2002.

[66] H. Hoppe and N. S. Sariciftci. Organic solar cells: An overview. *J. Mater. Res.*, 19:1924–1945, 2004.

[67] I. Tokareva, S. Minko, J. Fendler, and E. Hutter. Nanosensors based on responsive polymer brushes and gold nanoparticle enhanced transmission surface plasmon resonance spectroscopy. *Journal of the American Chemical Society*, 126(49):15950–15951, 2004.

[68] Y. Caspi, D. Zbaida, H. Cohen, and M. Elbaum. Synthetic mimic of selective transport through the nuclear pore complex. *Nano Lett.*, 8:3728–3734, 2008.

[69] T. Jovanovic-Talisman, J. Tetenbaum-Novatt, A. S. McKenney, A. Zilman, R. Peters, M. P. Rout, and C. B. T. Artificial nanpores that mimic the selecticity of the nuclear pore complex. *Nature*, 457:1023–1027, 2009.

[70] S. Kowalczyk, L. Kapinos, T. Blosser, T. Magalhães, P. van Nies, R. Lim, and C. Dekker. Single-molecule transport across an individual biomimetic nuclear pore complex. *Nature Nanotechnology*, 6(7):433–438, 2011.

[71] E. P. K. Currie, O. V. van der Gucht, J. Borisov, and M. A. Cohen Stuart. End-grafted polymers with surfactants: A theoretical model. *Langmuir*, 14:5740–5750, 1998.

[72] E. P. K. Currie, G. J. Fleer, M. A. Cohen Stuart, and O. V. Borisov. Grafted polymers with annealed excluded volume: A model for surfactant association in brushes. *Eur. Phys. J. E*, 1:27–40, 2000.

[73] J. U. Kim and B. O'Shaughnessy. Nanoinclusions in dry polymer brushes. *Macromolecules*, 39:413–425, 2006.

[74] Y. Chen and J. Z. Y. Chen. Absorption and engulfing transitions in nanoparticle infiltration into a polymer brush: A monte carlo simulation. *Journal of Polymer Science Part B: Polymer Physics*, 50(1):21–26, 2011.

[75] A. Halperin, M. Kröger, and E. Zhulina. Colloid-brush interactions: The effect of solvent quality. *Macromolecules*, 44:3622, 2011.

[76] Y. Y. Goldschmidt. Molecular dynamics of pancake vortices with realistic interactions: Observing the vortex lattice melting transition. *Phys. Rev. B*, 72:064518, 2005.

[77] W. H. Press, S. A. Teukolsky, W. T. Vetterling, and B. P. Flannery. *Numerical Recipes in Fortran 77: The Art of Scientific Computing, Second Edition*. Cambridge University Press, 2001.

[78] H. R. Warner, Jr. Kinetic theory and rheology of dilute suspensions of finitely extendible dumbbells. *Ind. Eng. Chem. Fundam.*, 11:379–387, 1972.

[79] A. K. Dolan and S. F. Edwards. The effect of excluded volume on polymer dispersant action. *Proc. Roy. Soc. London A, Math & Phys. Sci.*, 343:427–442, 1975.

[80] C. M. Wijmans, J. Scheutens, and E. B. Zhulina. Self-consistent field theories for polymer brushes. *Macromol.*, 25:2657–2665, 1992.

[81] R. R. Netz and M. Schick. Polymer brushes: From self-consistent field theory to classical theory. *Macromolecules*, 31:5105–5122, 1998.

[82] M. Opferman, R. Coalson, D. Jasnow, and A. Zilman. *Phys. Rev. E*, 86:031806, 2012.

[83] M. G. Opferman, R. D. Coalson, D. Jasnow, and A. Zilman. Morphology of polymer brushes infiltrated by attractive nanoinclusions of various sizes. *Langmuir*, 29:8584–8591, 2013.

[84] W. Senaratne, L. Andruzzi, and C. K. Ober. Self-assembled monolayers and polymer brushes in biotechnology: Current applications and future perspectives. *Biomacromolecules*, 6:2427–2448, 2005.

[85] E. P. K. Currie, W. Norde, and M. A. C. Stuart. Tethered polymer chains: surface chemistry and their impact on colloidal and surface properties. *Adv. Colloid Interface Sci.*, 100-102:205–265, 2003.

[86] A. C. Balazs, T. Emrick, and T. P. Russell. Nanoparticle polymer composites: Where two small worlds meet. *Science*, 17:1107–1110, 2006.

[87] R. J. Tseng, J. Huang, J. Ouyang, R. B. Kaner, and Y. Yang. Polyaniline nanofiber/gold nanoparticle nonvolatile memory. *Nano. Lett.*, 5:1077–1080, 2005.

[88] S. J. Green, J. J. Stokes, M. J. Hostetler, J. Pietron, and R. W. Murray. Three-dimensional monolayers: Nanometer-sized electrodes of alkanethiolate-stabilized gold cluster molecules. *J. Phys. Chem. B*, 101:2663–2668, 1997.

[89] L.-M. Chen, Z. Hong, G. Li, and Y. Yang. Recent progress in polymer solar cells: Manipulation of polymer: Fullerene morphology and the formation of efficient inverted polymer solar cells. *Adv. Mater.*, 21:1434–1449, 2009.

[90] J. Ouyang, C.-W. Chu, C. R. Szmanda, L. Ma, and Y. Yang. Programmable polymer thin film and non-volatile memory device. *Nature Materials*, 3:918–922, 2004.

[91] A. Boker, J. He, T. Emrick, and T. Russell. Self-assembly of nanoparticles at interfaces. *Soft Matter*, 3(10):1231–1248, 2007.

[92] S. S. Patel, B. J. Belmont, J. M. Sante, and M. F. Rexach. Natively unfolded nucleoporins gate protein diffusion across the nuclear pore complex. *Cell*, 129:83–96, 2007.

[93] M. Stewart. Molecular mechanism of the nuclear protein import cycle. *Nature Reviews Molecular Cell Biology*, 8(3):195–208, 2007.

[94] S. M. Liu and M. Stewart. Structural basis for the high-affinity binding of nucleoporin nup1p to the saccharomyces cerevisiae importin-β homologue, kap95p. *J. Mol. Biol.*, 349:515–525, 2005.

[95] V. N. Uversky. Natively unfolded proteins: A point where biology waits for physics. *Protein Science*, 11:739–756, 2002.

[96] D. Ron and P. Walter. Signal integration in the endoplasmic reticulum unfolded protein response. *Nat. Rev. Mol. Cell Biol.*, 8:519–529, 2007.

[97] S. Wente and M. Rout. The nuclear pore complex and nuclear transport. *Cold Spring Harbor Perspectives in Biology*, 2(10):a000562, 2010.

[98] S. Frey and D. Gorlich. A saturated fg-repeat hydrogel can reproduce the permeability properties of nuclear pore complexes. *Cell*, 130(3):512–523, 2007.

[99] T. Hardingham and H. Muir. The specific interaction of hyaluronic acid with cartilage proteoglycans. *Biochimica et Biophysica Acta - General Subjects*, 279:401, 1972.

[100] P. Kohli, C. Harrell, Z. Cao, R. Gasparac, W. Tan, and C. R. Martin. Dna-functionalized nanotube membranes with single-base mismatch selectivity. *Science*, 305:984–986, 2004.

[101] M. Murat and G. S. Grest. Structure of a grafted polymer brush: A molecular dynamics simulation. *Macromolecules*, 22:4054–4059, 1989.

[102] J. Yaneva, D. Dimitrov, A. Milchev, and K. Binder. Nanoinclusions in polymer brushes with explicit solvent - a molecular dynamics investigation. *J. Colloid. Interface Sci.*, 336:51–58, 2009.

[103] E. Zhulina, O. Borisov, V. Pryamitsyn, and T. Birshtein. Coil-globule type transitions in polymers. 1. collapse of layers of grafted polymer chains. *Macromolecules*, 24(1):140–149, 1991.

[104] J. Field, C. Toprakcioglu, R. Ball, H. Stanley, L. Dai, W. Barford, J. Penfold, G. Smith, and W. Hamilton. Determination of end-adsorbed polymer density profiles by neutron reflectometry. *Macromolecules*, 25(1):434–439, 1992.

[105] J. Kim and B. O'Shaughnessy. Morphology selection of nanoparticle dispersions by polymer media. *Physical Review Letters*, 89(23):238301, 2002.

[106] J. Huh, V. Valeriy, and A. Balazs. Thermodynamic behavior of particle/diblock copolymer mixtures: Simulation and theory. *Macromolecules*, 33(21):8085–8096, 2000.

[107] V. Pryamitsyn and V. Ganesan. Strong segregation theory of block copolymer-nanoparticle composites. *Macromolecules*, 39(24):8499–8510, 2006.

[108] R. Lim, U. Aebi, and B. Fahrenkrog. Towards reconciling structure and function in the nuclear pore complex. *Histochem. Cell Biol.*, 129:105–116, 2008.

[109] The PyMOL Molecular Graphics System, Version 1.3, Schrödinger, LLC. The PyMOL molecular graphics system, version 1.3r1. August 2010.

[110] P. J. Flory. *Principles of Polymer Chemistry*. Cornell University Press, 1953.

[111] C. Wijmans, J. Scheutjens, and E. Zhulina. Self-consistent field theories for polymer brushes: lattice calculations and an asymptotic analytical description. *Macromolecules*, 25(10):2657–2665, 1992.

[112] K. Binder. *Monte Carlo and Molecular Dynamics Simulations Polymer*. Oxford University Press., 1995.

[113] A. R. Leach. *Molecular Modelling: Principles and Applications, 2nd Edition*. Pearson Education Limited, 2001.

[114] M. Opferman, R. Coalson, D. Jasnow, and A. Zilman. *http://arxiv.org/abs/1110.6419*, 2011.

[115] R. Pathria. *Statistical Mechanics, 2nd Edition*. Elsevier, 1996.

[116] S. T. Milner. Strong-stretching and scheutjens-fleer descriptions of grafted polymer brushes. *J. Chem. Soc. Faraday Trans.*, 86:1349–1353, 1990.

[117] T. Biben and J. Hansen. Phase separation of asymmetric binary hard-sphere fluids. *Physical Review Letters*, 66(17):2215–2218, 1991.

[118] F. Solis and H. Tang. A bulk perturbation in a grafted brush. *Macromolecules*, 29(24):7953–7959, 1996.

[119] I. Coluzza and J. Hansen. Transition from highly to fully stretched polymer brushes in good solvent. *Physical Review Letters*, 100(1):16104, 2008.

[120] O. Guskova, S. Pal, and C. Seidel. Organization of nanoparticles at the polymer brush-solvent interface. *Europhys. Lett.*, 88:38006, 2009.

[121] N. Eisele, S. Frey, J. Piehler, D. Görlich, and R. Richter. Ultrathin nucleoporin phenylalanine–glycine repeat films and their interaction with nuclear transport receptors. *EMBO reports*, 11(5): 366–372, 2010.

[122] D. Angeli, J. E. Ferrell, and E. D. Sontag. Detection of multistability, bifurcations, and hysteresis in a large class of biological positive-feedback systems. *Proceedings of the National Academy of Sciences USA*, 101(7):1822, 2004.

[123] H. Iwata, I. Hirata, and Y. Ikada. Atomic force microscopic analysis of a porous membrane with ph-sensitive molecular valves. *Macromolecules*, 31:3671–3678, 1998.

[124] B. Yameen, A. Mubarak, R. Neumann, W. Ensinger, W. Knoll, and O. Azzaroni. Ionic transport through single solid-state nanopores controlled with thermally nanoactuated macromolecular gates. *Small*, 5:1287–1291, 2009.

[125] Y. Imanishi and Y. Ito. Glucose-sensitive insulin-releasing molecular systems. *Pure & Appl. Chem.*, 67:2015–2021, 1995.

[126] M. T. Müller, X. Yan, S. Lee, S. S. Perry, and N. D. Spencer. Lubrication properties of a brushlike copolymer as a function of the amount of solvent absorbed within the brush. *Macromolecules*, 38: 5706–5713, 2005.

[127] T. McPherson, A. Kidane, I. Szleifer, and K. Park. Prevention of protein adsorption by tethered poly (ethylene oxide) layers: experiments and single-chain mean-field analysis. *Langmuir*, 14(1): 176–186, 1998.

[128] S. Gon, M. Bendersky, J. L. Ross, and M. M. Santore. Manipulating protein adsorption using a patchy protein-resistant brush. *Langmuir*, 26(14):12147–12154, 2010.

[129] M. Tagliazucchi, O. Peleg, M. Kröger, Y. Rabin, and I. Szleifer. Effect of charge, hydrophobicity, and sequence of nucleoporins on the translocation of model particles through the nuclear pore complex. *Proceedings of the National Academy of Sciences*, 110(9):3363–3368, 2013.

[130] K. Binder and A. Milchev. Polymer brushes on flat and curved surfaces: How computer simulations can help to test theories and to interpret experiments. *J. Polym. Sci. Pol. Phys.*, 50:1515–1555, 2012.

[131] Y. Rabin and S. Alexander. Stretching of grafted polymer layers. *Europhys. Lett.*, 13:49, 1990.

[132] A. Chakrabarti and R. Toral. Density profile of terminally anchored polymer chains: A monte carlo study. *Macromolecules*, 23:2016–2021, 1990.

[133] R. M. Espinosa-Marzal, P. C. Nalam, S. Bolisetty, and N. D. Spencer. Impact of solvation on equilibrium conformation of polymer brushes in solvent mixtures. *Soft Matter*, Advance Article: doi:10.1039/c3sm27726g, 2013.

[134] S. Egorov. Insertion of nanoparticles into polymer brush under variable solvent conditions. *J. Chem. Phys.*, 137:134905, 2012.

[135] A. Halperin and M. Kroger. Collapse of thermoresponsive brushes and the tuning of protein adsorption. *Macromolecules*, 2011.

[136] D. L. Ermak and J. A. McCammon. Brownian dynamics with hydrodynamic interactions. *J. Chem. Phys.*, 69:1352–1360, 1978.

[137] H. Flyvbjerg and H. G. Petersen. Error estimates on averages of correlated data. *J. Chem. Phys.*, 91:461–466, 1989.

[138] J. O. Hirschfelder, C. F. Curtiss, and B. R. Byron. *Molecular Theory of Gases and Liquids*. John Wiley & Sons, 1965.

[139] M. Rout and G. Blobel. Isolation of the yeast nuclear pore complex. *J. Cell Biol.*, 123:771–783, 1993.

[140] R. Bayliss, K. Ribbeck, D. Akin, H. M. Kent, C. Feldherr, D. Görlich, and M. Stewart. Interaction between ntf2 and xfxfg-containing nucleoporins is required to mediate nuclear import of rangdp. *J. Mol. Biol.*, 293:579–593, 1999.

[141] R. Bayliss, T. Littlewood, and M. Stewart. Structural basis for the interaction between fxfg nucleoporin repeats and importin-β in nuclear trafficking. *Cell*, 102:99–108, 2000.

[142] B. Naim, D. Zbaida, S. Dagan, R. Kapon, and Z. Reich. Cargo surface hydrophobicity is sufficient to overcome the nuclear pore complex selectivity barrier. *EMBO J.*, 28:2697–2705, 2009.

[143] A. Becskei and I. W. Mattaj. Quantitative models of nuclear transport. *Curr. Opin. Cell Biol.*, 17: 27–34, 2005.

[144] A. Zilman, S. Di Talia, B. T. Chait, M. P. Rout, and M. O. Magnasco. Efficiency, selectivity, and robustness of nucleocytoplasmic transport. *PLOS Comput. Biol.*, 3:e125, 2007.

[145] J. A. Goodrich and J. F. Kugel. *Binding and Kinetics for Molecular Biologists*. Cold Spring Harbor Laboratory Press, 2007.

[146] K. Lott, A. Bhardwaj, G. Mitrousis, N. Pante, and G. Cingolani. The importin β binding domain modulates the avidity of importin β for the nuclear pore complex. *J. Biol. Chem.*, 285:13769–13780, 2010.

[147] B. Pyhtila and M. Rexach. A gradient of affinity for the karyopherin kap95p along the yeast nuclear pore complex. *J. Biol. Chem.*, 278:42699–42709, 2003.

[148] J. Tetenbaum-Novatt, L. E. Hough, R. Mironska, A. S. McKenney, and M. P. Rout. Nucleocytoplasmic transport: A role for nonspecific competition in karyopherin-nucleoporin interactions. *Mol. Cell. Proteomics*, 11:31–46, 2012.

[149] W. Yang, J. Gelles, and S. M. Musser. Imaging of single-molecule translocation through nuclear pore complexes. *PNAS*, 101:12887–12892, 2004.

[150] R. Moussavi-Baygi, Y. Jamali, R. Karimi, and M. R. K. Mofrad. Brownian dynamics simulation of nucleocytoplasmic transport: a coarse-grained model for the functional state of the nuclear pore complex. *PLOS Comput. Biol.*, 7:e1002049, 2011.

[151] D. Osmanovic, J. Bailey, A. H. Harker, A. Fassati, B. W. Hoogenboom, and I. J. Ford. Bistable collective behavior of polymers tethered in a nanopore. *Phys. Rev. E*, 85:061917, 2012.

[152] J. K. Forwood, A. Lange, U. Zachariae, M. Mafori, C. Preast, H. Grubmuller, M. Stewart, A. H. Corbett, and B. Kobe. Quantitative structural analysis of importin-β flexibility: paradigm for solenoid protein structures. *Structure*, 18:1171–1183, 2010.

[153] W. J. Kauzmann, K. Moore, and D. Schultz. Protein densities from x-ray crystallographic coordinates. *Nature*, 248:447–449, 1974.

[154] M. Vedadi, J. Lew, J. Artz, M. Amani, Y. Zhao, A. Dong, G. A. Wasney, M. Gao, T. Hills, S. Brokx, W. Qiu, S. Sharma, A. Diassiti, Z. Alam, M. Melone, A. Mulichak, A. Wernimont, J. Bray, P. Loppnau, O. Plotnikova, K. Newberry, E. Sundararajan, S. Houston, J. Walker, W. Tempel, A. Bochkarev, I. Kozieradzki, A. Edwards, C. Arrowsmith, D. Roos, K. Kain, and R. Hui. Structure of nuclear transport factor 2 (ntf2) from cryptosporidium parvum. *Mol. Biochem. Parasitol.*, 151:100–110, 2007.

[155] T. A. Isgro and K. Schulten. Binding dynamics of isolated nucleoporin repeat regions to importin-β. *Structure*, 13:1869–1879, 2005.

[156] F. Alber, S. Dokudovskaya, L. M. Veenhoff, W. Zhang, J. Kipper, D. Devos, A. Suprapto, O. Karni-Schmidt, R. Williams, B. Chait, A. Sali, and M. P. Rout. The molecular architecture of the nuclear pore complex. *Nature*, 450:695–701, 2007.